

Lifetime measurements in the lead region and the emergence of collectivity in ^{98}Zr

Inaugural-Dissertation
zur
Erlangung des Doktorgrades
der Mathematisch-Naturwissenschaftlichen Fakultät
der Universität zu Köln

vorgelegt von
Vasil Vasilev Karayonchev
aus Sofia

Köln 2020

Berichterstatter: Prof. Dr. Jan Jolie
Prof. Dr. Alfred Dewald

Tag der mündlichen Prüfung: 25.02.2021

Accepted for publication by the Faculty of Mathematics and Natural Sciences of the University of Cologne.

Abstract

The evolution from the single-particle, seniority-like structure to the emergence of collectivity has been investigated in the lead region through lifetime measurements. The fast-timing, the recoil-distance Doppler shift (RDDS), and the Doppler-shift attenuation (DSA) methods have been employed in the scope of this thesis.

Lifetimes of low-lying states in ^{211}At were measured in the $^{208}\text{Pb}(^6\text{Li},3\text{n})$ fusion-evaporation reaction via the fast-timing method and in the $^{209}\text{Bi}(^{16}\text{O},^{14}\text{C})$ two-proton transfer reaction via the RDDS and DSA methods. The deduced transition probabilities have been interpreted by two shell-model calculations. One was a multi-j shell-model calculation done using the Kuo-Herling residual interaction. The other one was done using a semi-empirical interaction for protons confined to the single-j $0h_{9/2}$ orbital. The Kuo-Herling calculations overestimate some of the ground-state transitions, which has been interpreted as a presence of particle-hole excitation in the ground-state wave function. However, the discrepancy between the calculated values and the measured ones is smaller than in the case of ^{210}Po . This shows that the effects of the particle-hole excitations are reduced when moving away from the ^{208}Pb core. The results from the single-j calculations describe the reduced transition probabilities well, which shows that seniority could be regarded as a good quantum number. The ^{209}Po nucleus was studied in the electron-capture decay of ^{209}At via the fast-timing technique. The deduced transition probabilities were compared to shell-model calculations done using the V_{low-k} approach based on the Bonn nucleon-nucleon potential. The results show that some of the states in ^{209}Po could be interpreted as single-particle neutron-hole states coupled to a ^{210}Po core. However, some additional contributions in the wave functions are needed to describe the experimental data better.

The onset of collectivity in the region was studied via fast-timing measurements of the lifetimes of the 4_1^+ states in ^{204}Po and ^{206}Po . The nuclei were studied via the $^{197}\text{Au}(^{11}\text{B},3\text{n})$ and the $^{198}\text{Pt}(^{12}\text{C},4\text{n})$ reactions, respectively. The results indicate that the transition to a collective behavior of the 4_1^+ states happens below $N=122$.

Additionally, the rapid onset of collectivity in the $A \approx 100$ region was investigated in the scope of this thesis. The low-spin structure of the ^{98}Zr nucleus was studied in the $^{96}\text{Zr}(^{18}\text{O},^{16}\text{O})$ two-neutron transfer reaction. Lifetimes were deduced using the RDDS and DSA techniques. The results were interpreted by a Monte Carlo shell-model and an interacting boson model with configuration mixing calculations. Both calculations reproduce most of the data but there are still some open questions regarding the low-spin structure of ^{98}Zr .

Contents

1	Introduction	7
1.1	Lifetime measurements	7
1.1.1	The fast-timing method	7
1.1.2	Doppler-shift methods	10
1.2	The nuclear shell-model	18
2	Lifetimes in ^{211}At and their implications on the nuclear structure above ^{208}Pb	23
3	Particle-hole excitations above ^{208}Pb	35
4	Lifetimes and structures of low-lying negative-parity states of ^{209}Po	45
5	Lifetimes of the 4_1^+ states of ^{206}Po and ^{204}Po: A study of the transition from noncollective seniority-like mode to collectivity	69
6	Tests of collectivity in ^{98}Zr by absolute transition rates	81
7	Conclusion and outlook	95
	Appendix: Test of the APCAD procedure for a DSA analysis: The lifetime of the 3_1^- state in ^{88}Sr	97
	Bibliography	103
	List of publications and conference proceedings	107
	Contribution to the publications in this thesis	109
	Acknowledgments	111
	Erklärung zur Dissertation	113

1 Introduction

1.1 Lifetime measurements

The lifetime of an excited nuclear state is an important observable. With the knowledge of the lifetime, electromagnetic transition matrix elements between different nuclear states can be calculated. Together with the excitation energies, these matrix elements are one of the most important observables in the nuclear structure. They are used to benchmark the wave function predicted by nuclear models. The transition matrix elements are often sensitive to small contributions in the wave functions which could not be distinguished when looking only at the excitation energies. An example of such contributions are the particle-hole excitations, which have been studied in the scope of this thesis.

Nuclear lifetimes cover a wide range of values - from nuclear resonances, which have lifetimes in the order of 10^{-22} s to isomeric states which have lifetimes longer than minutes. Different techniques are used to measure nuclear lifetimes depending on their magnitude. A review of the techniques can be found in Refs. [1, 2]. In this doctoral thesis, three methods are employed to extract lifetimes of excited nuclear states. The fast-timing method was used to extract lifetimes of excited states in ^{204}Po , ^{206}Po , ^{209}Po and ^{211}At . The Doppler-shift techniques, namely the recoil-distance Doppler shift method and the Doppler-shift attenuation method were employed to measure lifetimes in ^{211}At and ^{98}Zr . These methods are briefly described in the following subsections.

1.1.1 The fast-timing method

The fast-timing method is a direct method for measuring nuclear lifetimes in the range from few μs down to few ps. The technique relies on the measurement of the time difference between two events feeding and decaying from a nuclear state of interest. In principle, any event that provides a time reference related to the population or the decay of an excited state can be used. Such events are the detection of heavy ions, γ rays, conversion electrons, β particles, etc. A pulsed beam can also be used as a time reference. Depending on the particular case a suitable combination of these events can be employed to determine the lifetime of the nuclear state. In the scope of this doctoral thesis, the γ - γ fast-timing method

in combination with ultra-fast $\text{LaBr}_3(\text{Ce})$ scintillator detectors was used to measure lifetime of excited nuclear state in ^{204}Po , ^{206}Po , ^{209}Po and ^{211}At . The recent development of ultra-fast $\text{LaBr}_3(\text{Ce})$ scintillators [4] has given a new life to the γ fast-timing measurements. The unique combination of a good energy resolution and a fast response has made the $\text{LaBr}_3(\text{Ce})$ detectors the prime detector to use in fast-timing measurements. The superb resolution of the $\text{LaBr}_3(\text{Ce})$ detectors has allowed conducting reliable fast-timing measurements after neutron-induced fission [5] in which a large number of nuclei are populated resulting in an extremely complex γ -ray spectrum. In recent years, there has been also a development of the methodology of the fast-timing technique. The Generalized Centroid Difference (GCD) [6] method has been developed making the analysis of the experimental data easy and straightforward, especially for setups consisting of a large number of detectors. Furthermore, the time-walk associated with the electronics used in the fast-timing experiments has been optimized [7, 8] down to the x-ray region [9]. During his Ph.D. the author has also contributed to the development fast-timing technique [7, 9, 10].

A principal scheme of a γ - γ fast-timing setup employing analog timing is displayed in Fig. 1. A detector pair can detect γ rays coming from a source. One of the output signals of the detector, usually the anode output of the photomultiplier tube of the $\text{LaBr}_3(\text{Ce})$ detector, is fed to the input of a Constant Fraction Discriminator (CFD). The CFD is a time derivation device that triggers at a constant fraction of the maximum value of the signal. This minimizes the time walk of the signal, which is the dependence of the time-reference signal from the amplitude of the input signal pulse. The output of the CFD, which is a logical signal is then fed to the "start" or "stop" inputs of an analog time to amplitude converter (TAC). The TAC produces a logical signal with an amplitude that is proportional to the time difference between the two input signals. This signal is recorded by the Data Acquisition System (DAQ). The recorded TAC spectrum is known as the time-difference spectrum or time-difference distribution. The other output of the detectors (the dynode signals), usually preamplified, are fed directly to the DAQ and are used to record the energy of the detected γ rays.

In the scope of this thesis the time-difference spectra are analyzed according to the mirror-symmetric centroid difference method [11] which is an extension of the centroid difference method [3]. Two γ rays feeding (γ_1) or decaying from (γ_2) a certain nuclear level can be detected by the detector system. If the feeding γ ray is detected by the start detector (Det. 1) and the decaying γ ray by the stop detector (Det. 2) the time-difference spectrum recorded by the DAQ is called the *delayed* spectrum. If the feeding γ ray is detected by

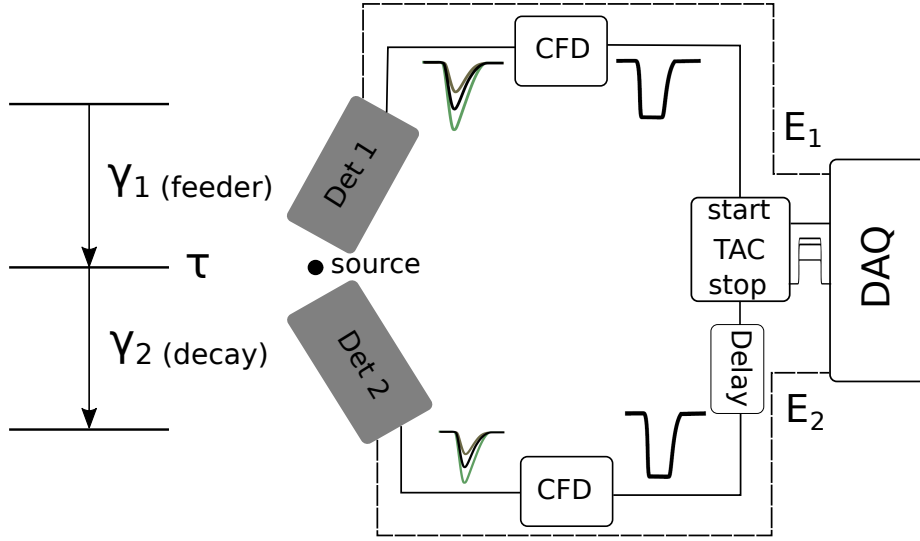


Figure 1: Principal scheme of a fast-timing setup.

the stop detector and the decaying γ ray by the start detector, the *anti-delayed* spectrum is recorded. The lifetime τ of the state of interest is then given by [11]:

$$\Delta C = C_d - C_a = 2\tau + PRD, \quad (1.1)$$

where ΔC is the difference of the centroid of the two time-distributions. C_d is the centroid of the delayed distribution and C_a of the anti-delayed. The Prompt Response Difference (PRD) is the centroid difference obtained when a prompt event is measured. The PRD depends on both the energy of the feeding and decaying γ rays.

The energy dependence of the PRD, known as the PRD curve, is measured by standard calibration sources, e.g. ^{152}Eu , ^{133}Ba , ^{226}Ra , etc. By selecting a feeder-decay combination of a level with known lifetime, the centroid difference ΔC is measured and the PRD could be determined directly from Eq. (1.1). An example of a PRD curve calibrated with an ^{152}Eu source is shown in Fig. 2.

The fast-timing procedure described here could be generalized for a detector system consisting of more than two detectors by superimposing the time-difference spectra of all the unique detector combination [6]. The method is known as the Generalized Centroid Shift (GCD) method and is used in the scope of this thesis.

To reduce the influence of time-correlated background and transitions with energies similar to those of the feeder or the decay, an external to the fast-timing system trigger can be used. Such a trigger can be provided by an ionization chamber, a high purity

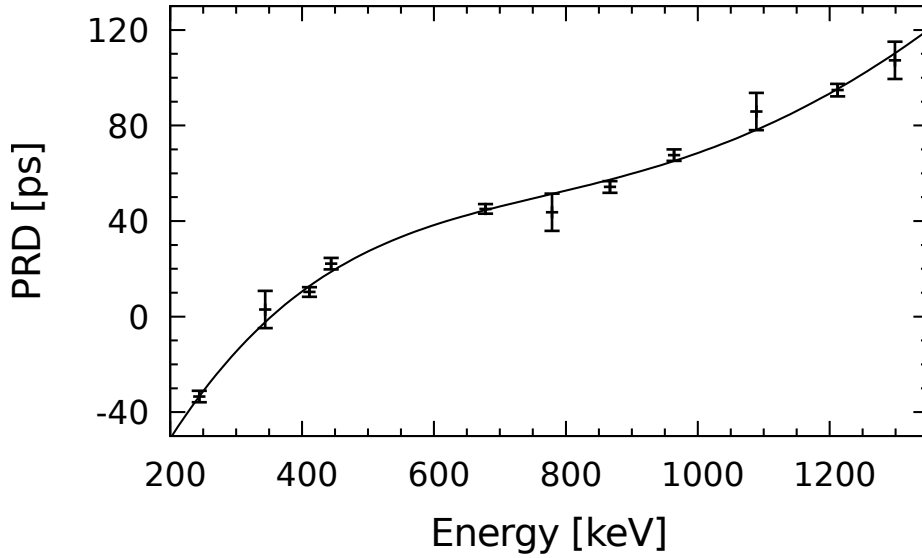


Figure 2: The prompt response difference (PRD) curve obtained with an ^{152}Eu source. The figure is taken from Ref. [12]

germanium (HPGe) detector, a β detector, etc. In this work, the fast-timing measurements were performed by utilizing an additional trigger provided by a HPGe gate.

1.1.2 Doppler-shift methods

The RDDS and DSA methods are two essentially different techniques for measuring lifetimes of excited nuclear states. However, both Doppler shift techniques rely on registering the Doppler shift of γ rays emitted by a nucleus in flight. The Doppler shift of a moving source is given by:

$$E = E_0 \frac{\sqrt{1 - \beta^2}}{1 - \beta \cos \theta}, \quad (1.2)$$

where E_0 is the energy of the γ ray depopulating a nuclear state and $\beta = v/c$ is the ratio of the speed of the excited nucleus v and the speed of light c . θ is the angle between the velocity of the moving source and the detector. The difference between the two methods is how the time scale is established. In the RDDS technique, the time scale is established by the time of flight of the excited nucleus between a target and a stopper foil. In the DSA technique, the time scale is established by the slowing-down time of the excited nucleus inside the stopper material. The experiments employing the Doppler shift techniques presented in this work were performed at the Plunger setup of the University of Cologne [13]. The setup consists of twelve HPGe detectors. Eleven detectors are positioned in two rings

around the target chamber at a distance of about 11 cm from the reaction target center. Six HPGe detectors are positioned at 45° and five at 142° relative to the beam axis. Additionally, there is one detector positioned at 0° . The detectors have efficiencies between 60 % and 100 % relative to $\varnothing 3" \times 3"$ cylindrical NaI detectors. The total absolute efficiency of the setup is ≈ 2 % at 1.3 MeV. The Plunger setup can be equipped with an array of six 1×1 cm photovoltaic PIN diodes positioned at backward angles. The photovoltaic cells¹ are a cheap alternative to the more expensive dedicated semi-conductor particle detectors. These particle detectors allow different reaction channels to be selected by applying gates in the energy spectrum of the detected particles. If the masses of the target and the stopper are largely different (e.g. bismuth and magnesium), a distinction between the two can be made in the particle spectrum. Additionally, the reaction kinematics is also restricted. By detecting beam-like recoils from a transfer or Coulomb-excitation reactions at backward angles the possible angles of the target-like products flying out of the target is restricted. This leads to smaller Doppler broadening due to reaction kinematics which allows for more precise measurements to be made.

The recoil distance Doppler shift method

The RDDS method is an experimental technique for measuring lifetimes of excited nuclear states in the range of 1 ps to 1 ns [14]. The lifetimes can be determined from experimental quantities measured directly from the γ -ray spectrum. The method is described in detail in the review article [13] and the references within. Here only the essential ideas needed for the analysis are presented.

A principle scheme of a RDDS setup is shown in Fig. 3. An excited state i of a nucleus populated in the target can decay in flight or after stopping in the stopper. The γ rays emitted during the flight appear Doppler shifted in the γ -ray spectrum. The corresponding peak is known as a shifted peak and its intensity is $I_i^s(t)$. The γ rays emitted after the excited nucleus has stopped in the stopper are not Doppler shifted and result in an unshifted peak with an intensity $I_i^u(t)$. Both intensities are a function of the time of flight of the excited nucleus between the target and the stopper t . The decay curve for the state i is defined as:

$$R_i(t) = \frac{I_i^u(t)}{I_i^u(t) + I_i^s(t)}.$$

In the simple case where the excited state has no feeding transitions the decay curve is

¹PDB-C613-2 by Advanced Photonix

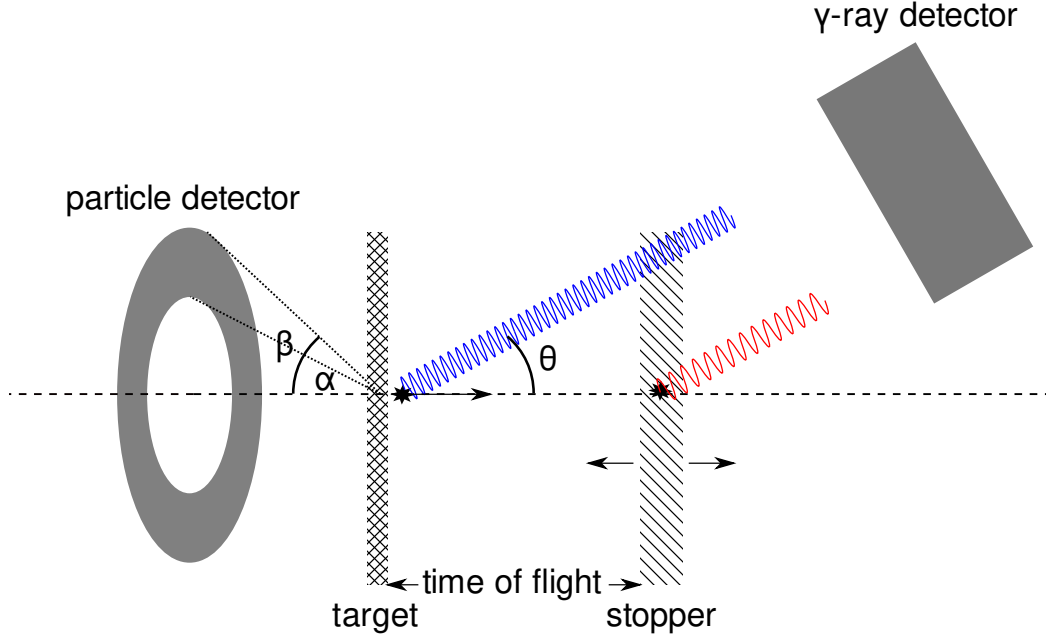


Figure 3: Principal scheme of a RDDS setup. Only beam-like particle scattered between angles α and β can be detected by the particle detector.

simply:

$$R_i(t) = e^{-t\lambda_i}, \quad (1.3)$$

where λ_i is the decay constant of the excited state i . In a realistic case, the state has a feeding pattern which needs to be taken into account to extract the lifetime of the state correctly. A system of differential equations, known as the Bateman equations needs to be solved. The equations relate the number of the nuclei in the state i $n_i(t)$ as a function of the time t , depending on the decay constant λ_i . The Bateman equations are:

$$\frac{d}{dt}n_i(t) = -\lambda_i n_i(t) + \sum_{k=i+1}^N \lambda_k n_k(t) b_{ki}.$$

Here k denotes the excited states feeding the state i , b_{ki} are the branching ratios between states k and the state i and N is the total number of states. The solutions of these equations with respect to the decay curve $R_i(t)$ is given by:

$$R_i(t) = P_i e^{-t\lambda_i} + \sum_{k=i+1}^N M_{ki} \left[(\lambda_i/\lambda_k) e^{-t\lambda_k} - e^{-t\lambda_i} \right]. \quad (1.4)$$

M_{ki} is defined recursively as:

$$M_{ki}(\lambda_i/\lambda_k - 1) = b_{ki}P_k - b_{ki} \sum_{m=k+1}^N M_{mk} + \sum_{m=i+1}^{k-1} M_{km}b_{mi}(\lambda_m/\lambda_k),$$

where P_i is the population of the state i . In the case where the feeding pattern is simple like in the transfer experiments employed in this work, the direct application of the Eq. (1.4) to the experimental data is straightforward.

Target-to-stopper distances are chosen depending on the lifetime to be measured so data points could be obtained evenly throughout the decay curve. The shifted and the unshifted components used to determine the ratios $R(t)$ are obtained by fitting or integrating the spectrum. Integration is only possible when the two components are well separated. It is always preferred since there are no systematic errors associated with the choice of many fit parameters. However, often the energy separation of the two components is not sufficient and the two components are not completely separated. The two components are then usually fitted using two Gaussian functions. Care should be taken when determining the width of the fits. When the statistics is not sufficient for a coincidence analysis, the width of the unshifted component can be obtained from a calibration source or by looking at the spectrum obtained at the shortest target-to-stopper distance if the unshifted component is dominant. The width of the shifted component can be obtained by looking at the spectrum obtained at the longest distance where the shifted component is dominant. Once the widths are obtained they are fixed and used in the fits for all the distances. Alternatively, a DSA simulation can be performed to simulate the spectrum and obtain the lifetime. This is especially useful when the lifetimes becomes comparable to the stopping time of the ion inside the stopper. Such an approach is presented below .

The RDDS experiments presented in this work are performed using the Cologne Plunger device which is described in detail in the review article [13].

The Doppler shift attenuation method

The DSA method is widely used for measuring nuclear lifetimes from the few ps region down to the fs region. A description of the method can be found in the review articles [1, 2].

A schematic of a DSA experiment is given in Fig. 4. Excited nuclei produced in the target layer are allowed to recoil in a stopping material. While the nuclei are slowing down they emit γ rays which will appear Doppler shifted in the γ -ray spectrum. Since the stopping

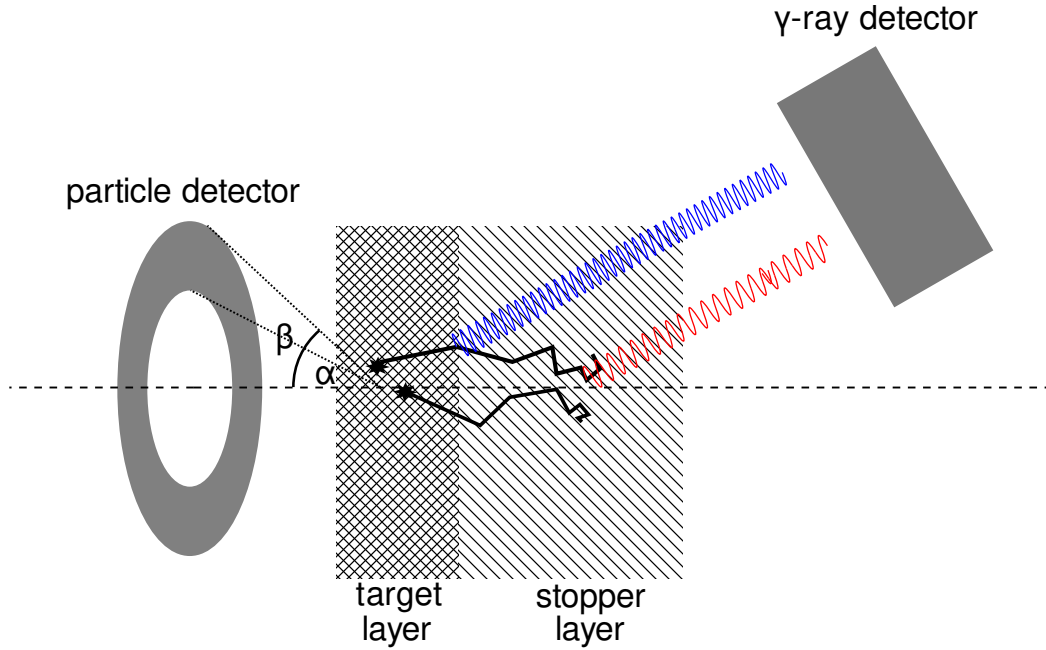


Figure 4: Principal scheme of a DSA experiment. Only beam-like particle scattered between angles α and β can be detected by the particle detector.

is a continuous process the detected γ rays will also have a continuous energy distribution. The shape of the peak inside the energy spectrum of the γ detector will be broadened and is known as a *Doppler broadened lineshape*. If the stopping process is known, the lifetime τ of the excited state can be obtained by fitting the Doppler-broadened lineshape. In this work, the DSA analysis was performed using the computer program APCAD which is described in detail in Ref. [15].

In APCAD the stopping process of the ions is modeled using a Monte-Carlo simulation in the framework of Geant4 [16]. The electronic and nuclear stopping powers used in the simulation are provided by an external table. In this work, the stopping powers are taken from the software package SRIM [17]. The nuclear stopping powers are usually reduced by 30 % to account for microchanneling effects [18] due to the microcrystalline structure of the target. APCAD simulates the kinematics of an arbitrary two-body reaction of the type A(B,C)D, such as the transfer reactions used in the scope of this doctoral thesis. The doubly-differential cross-section of the reaction is provided externally by the user. The ideal case would be if the cross-section is already experimentally available. Unfortunately, this experimental data is very seldom available and is mainly limited to light fragments reactions, e.g. (t,p), (d,p), etc. reactions. Alternatively, the reaction cross-sections can be taken from, e.g., the GRAZING code [19, 20]. The influence of the choice of cross-

section on the simulation results has been investigated in this work and it was found that it does not play a significant role. Experimentally, this can be attributed to the fact that the reaction kinematics is to some extent fixed by the particle detectors at backward angles. Additionally, the beam does not lose a significant amount of energy in the target layers. The result of the stopping simulations is a file containing the time evolution of the velocity vectors of the simulated ions. Based on this file APCAD calculates the Doppler shift observed by each angular bin of the γ detector system. In this calculation, APCAD takes into account the detector geometry and the kinematic restrictions imposed by the particle detectors. The result of this calculation is the so-called *stopping matrix*. The stopping matrix gives the probability to observe a γ ray with a given Doppler shift as a function of the time after the excitation of the ion. This distribution can be folded with the decay function of the excited state and the detector repose and fitted to the experimental Doppler-broadened lineshape of the peak of interest to obtain the lifetime of the state τ . In this procedure, the feeding coming from higher-lying states is taken into account according to the Bateman equation (1.4). As an example, the stopping matrix of the $^{209}\text{Bi}(^{16}\text{O},^{14}\text{C})^{211}\text{At}$ experiment presented in Chapter 3 is shown in Fig. 5.

The procedure of APCAD for obtaining lifetimes has been tested for the first excited 3^- state in ^{88}Sr . The obtained result of 0.97(7) ps is in perfect agreement with the literature value of 1.0(7) ps [52]. The procedure is described in the Appendix.

DSA simulation of a RDDS experiment

When measuring short lifetimes in a RDDS experiment, the stopping of the ions inside the stopper starts to play a significant role on the obtained lifetimes. This is especially important for lower energy transitions that do not have well-separated shifted and unshifted components. To account for this effect, a DSA simulation can be performed and the experimental spectrum can be fitted to obtain the lifetime. This can be done by the procedure described before. To reproduce the RDDS setup, a triple target is defined in the simulation: a target, a stopper, and a vacuum layer between them. This approach is used in this work to obtain the lifetime of the 2_3^+ in ^{98}Zr (see Chapter 6). The stopping matrices for two target-to-stopper distances are displayed in Fig. 6.

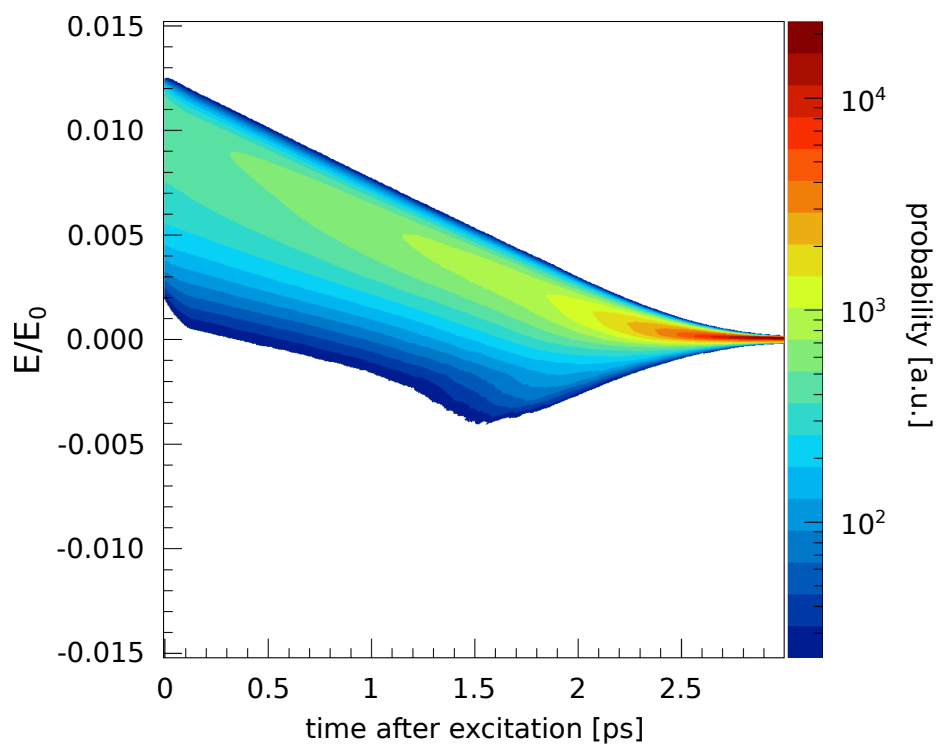


Figure 5: Stopping matrix for ^{211}At ions populated in the $^{209}\text{Bi}(^{16}\text{O}, ^{14}\text{C})^{211}\text{At}$ reaction stopping in a two-layer target. The target is 0.5 mg/cm^2 ^{209}Bi evaporated on a 1.5 mg/cm^2 Mg stopper. The beam energy is 84 MeV.

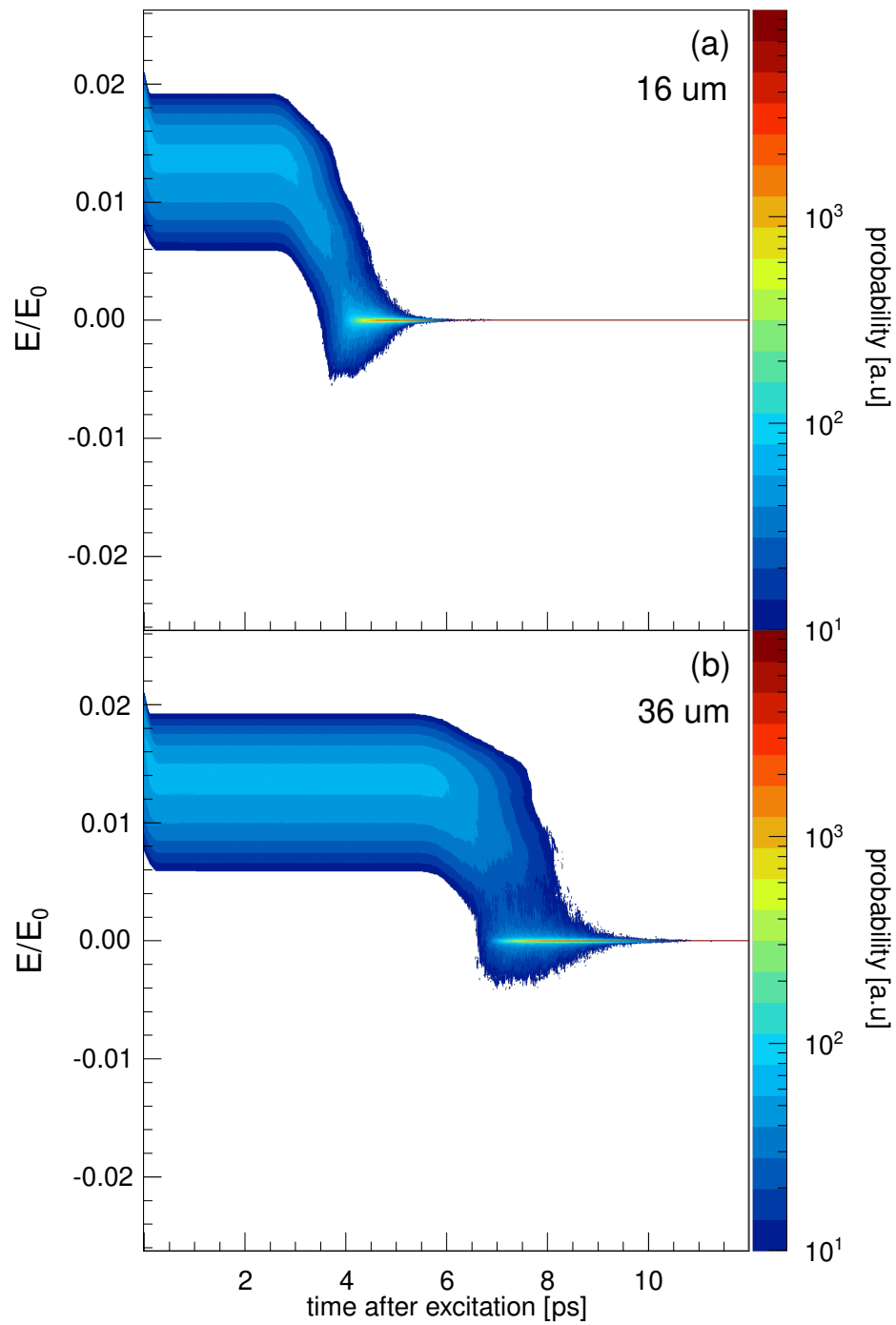


Figure 6: Stopping matrix of the $^{96}\text{Zr}(^{18}\text{O}, ^{16}\text{O})^{98}\text{Zr}$ reaction for two target-to-stopper distances.

1.2 The nuclear shell-model

The atomic nucleus is a quantum many-body system consisting of strongly interacting protons and neutrons. The interaction between them can be considered as an effective residue of the strong interaction between the quarks, the constituents of the nucleons, which is described by quantum chromodynamics (QCD) [21]. At the low-energy regime, where quarks are bound to nucleons, the strong coupling constant $\alpha_s \approx 1$ and perturbation theory can not be used. The mathematical problem of obtaining the nucleon-nucleon interaction, considering the many degrees of freedom of the involved particles, is very complex. Alternative approaches which simplify this problem are the model-based approaches which aim to describe the nucleon-nucleon interaction. Such approaches are the Hamada and Johnson potential [22] and the Bonn-potential [23]. In the last years, significant progress in deriving the nucleon-nucleon interaction from QCD has been made in terms of the model-independent chiral field effective theory [24, 25]. Once the nucleon-nucleon forces are available, the nuclear many-body problem can be tackled directly by solving the Schrödinger equation. This approach is known as the *ab initio* method. The complexity of the problem grows drastically with the number of nucleons involved. Consequently, the problem can be solved exactly only for very light nuclei.

A successful framework for microscopic nuclear structure calculations that simplifies massively this problem is the nuclear shell model [26]. It is based on the assumption that nucleons move independently in a central potential, a mean-field. The central potential is usually modeled by a Woods–Saxon potential or a harmonic oscillator potential. This gives rise to the experimentally observed shell structure. With the addition of a strong spin-orbital term, the shell model reproduces the magic numbers [27, 26] which corresponds to closed major shells. Within this model, the valence nucleons, external to the filled shells, interact through the two-body residual interaction (the part of the interaction that is not absorbed into the central potential), which induces mixing of different nuclear configurations. The residual nuclear interaction is usually derived from realistic nucleon-nucleon potentials. Such are the approach of Kuo and Herling [28] based on the Hamada-Johnson potential [22] and the V_{low-k} approach [29] based on the Bonn potential [23]. However, these approaches still require experimental input to fix the parameters involved when constructing the matrix elements of the two-body residual interaction. Here the study of nuclei with only a few valence nucleons plays a pivoting role. The limited valence space allows for the shell-model calculations to be performed in full-basis, without the need for truncations. The result of the calculation can be then compared to physical observables to test and fine

tune the used residual interaction.

The ^{208}Pb region

The ^{208}Pb nucleus is the heaviest known doubly-magic nucleus. The region around it has attracted significant interest during the years. Experimentally, the presence of stable isotopes gives access to many nuclei and there is a large amount of spectroscopic data already available. Theoretically, the fact that ^{208}Pb can be regarded as a good doubly-magic nucleus has motivated many successful shell model calculations [30, 31, 32, 33, 34]. These calculations have been mainly concentrated on describing the energy spectrum of the nuclei around ^{208}Pb .

Recent measurement of lifetimes in ^{210}Po [35] and ^{212}Po [36], have shown that the low-lying structure of these nuclei cannot be understood completely in the framework of the shell model. Calculations carried out using the Kuo-Herrling residual interaction [32] overestimate up to two times the transition probabilities of the $2_1^+ \rightarrow 0_1^+$ transition. This could be interpreted as an admixture of particle-hole excitations across the $Z=82$ shell closure. To investigate further the particle-hole excitations above ^{208}Pb , the ^{211}At nucleus was studied via the $^{208}\text{Pb}(^6\text{Li},3n)$ fusion-evaporation reaction and via the $^{209}\text{Bi}(^{16}\text{O},^{14}\text{C})$ two-proton transfer reaction. The fast-timing, RDDS, and DSA methods were used to determine the lifetimes of low-lying states.

The structure of odd-even nuclei is governed by the coupling of the odd particle to the closest even-even nucleus. With very few exceptions of isomeric states and states in the stable ^{207}Pb and ^{209}Bi nuclei, the information on the lifetimes of the odd-even nuclei in the region above ^{208}Pb is very limited. Experimental and theoretical studies of these nuclei are of great importance for understanding the evolution of the single-particle orbitals and the interaction between the nucleons. To study how the odd neutron holes couple to the ^{210}Po core, the odd-even nucleus ^{209}Po was studied in the electron capture decay of ^{209}At via the fast-timing technique.

The onset of collectivity in the ^{208}Pb region

It is well known that the proton-neutron correlations tend to drive collective nuclear behavior [37]. When the number of both valence proton and neutron grows, the quadrupole part of the residual interaction acting between the protons and neutrons starts to increase and proton-neutron correlations start to develop. At some point, this leads to the breakdown of the neutron-neutron and proton-proton pairing correlations and the development of spatial proton-neutron correlations [38]. Due to the long-range proton-neutron correla-

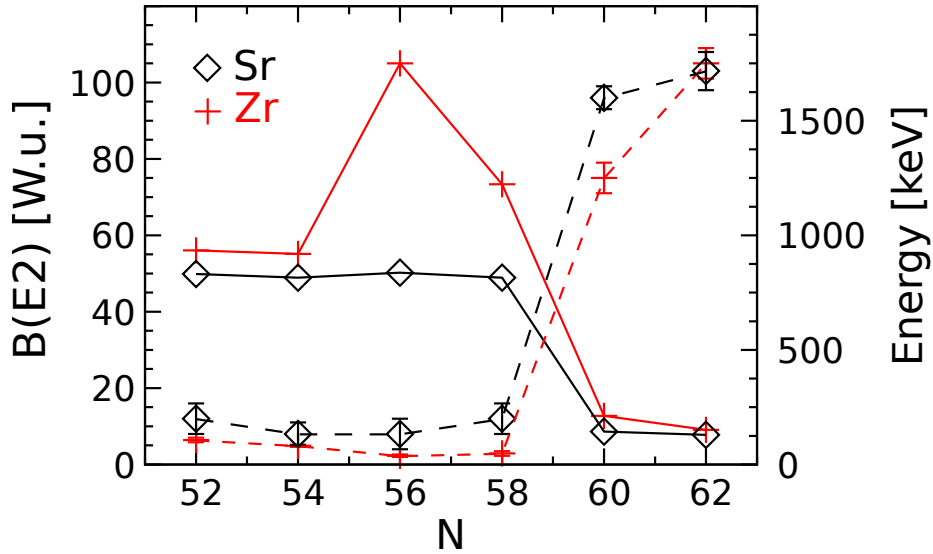


Figure 7: The energies of the first excited 2^+ states for Zr and Sr isotopes with $N = 52-62$ (symbols connected by a solid line), together with the $(BE2; 2_1^+ \rightarrow 0_1^+)$ (symbols connected by a dashed line). Data are taken from the nuclear data sheets [42, 43, 44, 40, 41, 45]. The $B(E2; 2_1^+ \rightarrow 0_1^+)$ value for ^{98}Zr is taken from Ref. [46]. This figure and caption are taken from Ref. [12].

tions many nucleons are involved in the nuclear excitation, leading to a collective behavior. A key experimental indicator for the presence of collective behavior is high $E2$ transition rates between the low-lying nuclear states. It was recently shown, via Coulomb-excitation measurements [39], that there is an increased collectivity of the $2_1^+ \rightarrow 0_1^+$ transition in $^{208,210}\text{Rn}$ and ^{206}Po . However, the experimental information on the lifetimes in even-even nuclei in the region remains very limited up to date, which hinders the understanding of the onset of quadrupole collectivity in the region above ^{208}Pb . To improve the understanding of the development of collectivity in the region, ^{204}Po and ^{206}Po were studied in the scope of this doctoral thesis. The nuclei of interest were populated in the $^{197}\text{Au}(^{11}\text{B},3n)$ and the $^{198}\text{Pt}(^{12}\text{C},4n)$ fusion-evaporation reactions, respectively, and were studied via the fast-timing technique.

The rapid onset of collectivity in Sr and Zr isotopes

While the onset of collectivity is usually a gradual process, the Sr and Zr isotopes are unique on the nuclear chart. When crossing $N=60$ their structural behavior changes rapidly from a single-particle one to a collective one. This is very well seen through the rapid drop in the excitation energies of the first excited 2^+ states and the drastic rise in the transition probabilities of the $2_1^+ \rightarrow 0_1^+$ transition when crossing $N=60$ [40, 41] (see Fig. 7).

The rapid onset of collectivity in the Sr and Zr isotopes has been attributed to the specific ordering of the orbitals in the region and specifically to the strong isoscalar attractive proton-neutron interaction between the spin-orbital partner orbitals, the $\pi(1g_{9/2})$ and the $\nu(1g_{7/2})$ [38, 47, 48].

^{98}Zr is a key nucleus as it lies on the interface of the onset of collectivity. Recent lifetime measurements in ^{98}Zr have revealed that the 2_1^+ and 0_2^+ could be considered as members of a collective structure [46]. However, this measurement was a singles RDDS measurement where the ^{98}Zr was produced after fission of a ^{238}U beam on a ^9Be target. The feeding pattern in such experiments is extremely complicated. To corroborate the lifetime measurements and further study the ^{98}Zr nucleus an experiment was performed in the scope of this thesis. The ^{98}Zr nucleus was populated in the $^{96}\text{Zr}(^{18}\text{O}, ^{16}\text{O})$ two-neutron transfer reaction at energies below the Coulomb barrier, which simplifies the feeding massively. The study is presented in Chapter 6.

Publication I:

2 Lifetimes in ^{211}At and their implications on the nuclear structure above ^{208}Pb

Lifetimes in ^{211}At and their implications for the nuclear structure above ^{208}Pb

V. Karayonchev,^{*} A. Blazhev, A. Esmaylzadeh, J. Jolie, M. Dannhoff, F. Diel, F. Dunkel, C. Fransen, L. M. Gerhard, R.-B. Gerst, L. Knafla, L. Kornweibel, C. Müller-Gatermann, J.-M. Régis, N. Warr, and K. O. Zell
Institut für Kernphysik, Universität zu Köln, D-50937 Köln, Germany

M. Stoyanova

Faculty of Physics, St. Kliment Ohridski University of Sofia, 1164 Sofia, Bulgaria

P. Van Isacker

Grand Accélérateur National d'Ions Lourds, CEA/DRF–CNRS/IN2P3, Bvd Henri Becquerel, F-14076 Caen, France



(Received 9 October 2018; published 28 February 2019)

Lifetimes of excited states in ^{211}At were measured using the electronic γ - γ fast timing technique. The nucleus of interest was populated in a $^{208}\text{Pb}(^6\text{Li}, 3n)^{211}\text{At}$ fusion-evaporation reaction at the FN Tandem accelerator of the Institute for Nuclear Physics, University of Cologne. The lifetimes of the $17/2^-$ and $23/2^-$ states were determined, together with an upper limit for the $13/2^-$ state. The experimental results are compared to two shell-model calculations, one using a semiempirical interaction for three particles in a single $j = 9/2$ shell and the other using the modified Kuo-Herling interaction in a multi- j model space.

DOI: [10.1103/PhysRevC.99.024326](https://doi.org/10.1103/PhysRevC.99.024326)

I. INTRODUCTION

The semimagic nucleus ^{211}At is located three protons above the doubly magic nucleus ^{208}Pb . Having only three valence particles makes ^{211}At a very good candidate to test the nuclear shell model (SM) as the calculations can be made in a large basis without any truncations. Moreover, it is also possible that the low-spin structure can be described in a single- j approximation, limiting the model space to only three protons in the $0h_{9/2}$ orbital. One of the advantages of a SM description confined to a single- j orbital is that simple, analytic predictions can be made, which can then be compared with observed nuclear properties. This approach is beautifully illustrated by the relations that can be established between the energy spectrum of two nucleons in a j orbital, j^2 , and that of three nucleons j^3 (see chap. 21 of Ref. [1]). These relations are satisfied if the nuclear interaction conserves seniority, which is the case if $j \leq 7/2$ and if the interaction is of two-body character. Even if $j \geq 7/2$, seniority is usually fairly well conserved among identical nucleons and a lowest-seniority approximation should suffice at low energy. Deviations from the predicted energy relations therefore probe the existence of seniority-breaking and/or three- and higher-body interactions in a single- j model space. Similar relations exist between electromagnetic properties of neighboring nuclei, in particular between electric quadrupole ($E2$) matrix elements. If the $E2$ operator is of one-body character, then a single matrix element is needed (e.g., the quadrupole moment in the one-nucleon configuration or the $2^+ \rightarrow 0^+$ matrix element in the j^2 configuration) to predict all $E2$ transitions

between j^n states. Just as deviations from the predicted energy relations indicate the presence of higher-body interactions, departures from the predicted decay rates may be attributed to higher-order terms in the $E2$ operator. Such terms are to be expected since, as repeatedly emphasized [2,3], a consistent theory requires not only an effective Hamiltonian but equally well-effective transition operators, tailored to the model space under consideration.

A one-plus-two-body electric quadrupole operator can be fixed from $E2$ matrix elements in the j and j^2 configurations. In its full generality, this requires the knowledge not only of all $E2$ transitions but also of all electric quadrupole moments—an experimental luxury that is seldom (or never) available. Therefore, in the Appendix, a method is developed that eliminates the need for the knowledge of quadrupole moments. Once this simplification is accepted, one can compare the predictions of the one-body $E2$ operator with those of one with one-plus-two-body character to examine whether the latter yields superior results. For comparison, also the results of a full SM calculation are shown, in a nontruncated basis, taking into account the full $82 \leq Z \leq 126$ proton major shell above ^{208}Pb .

Experimentally, the presence of the $29/2^+$, 50-ns isomer in ^{211}At makes the determination of lifetimes of lower-lying states employing Doppler-shift based methods very hard. For this reason we have employed the fast-timing technique.

Section II describes the performed experiment and its analysis. Section III compares the results with a single- j prediction and with a large-basis SM calculation, showing good agreement, except in a few cases where an explanation for the disagreement has been provided. The large-basis SM calculations show intriguing discrepancies for the $M1$ transitions in the $N = 126$ isotones above ^{208}Pb , which demands

^{*}Corresponding author: karayon@ikp.uni-koeln.de

further theoretical work. The derivation of the formulas in the single- j approximation is presented in the Appendix.

II. EXPERIMENT AND ANALYSIS

The nucleus of interest was populated in the $^{208}\text{Pb}(^6\text{Li}, 3n)^{211}\text{At}$ fusion-evaporation reaction. An average beam current of 5 pA with an energy of 34 MeV was provided by the Cologne 10 MV FN-Tandem accelerator. The target used was a 54-mg/cm² ^{208}Pb foil enriched to 99.14%. The thick target stopped all produced nuclei and the beam particles, thus preventing background γ rays produced in reactions of the primary beam with the beam line, downstream of the target, or the beam dump. The detector array consisted of eight HPGe detectors and nine LaBr₃(Ce) scintillators (called hereafter LaBr), each with dimensions $\varnothing 1.5 \times 1.5$ in. Six of the LaBr detectors were placed inside bismuth germanate (BGO) anti-Compton shields in order to suppress the Compton background. The other three LaBr detectors had lead shields suppressing background events associated with scattered γ rays. The time difference spectra of every unique combination of LaBr detectors were recorded using time to amplitude converters (TAC) applying the multiplexed-start and multiplexed-stop electronics circuitry [4]. The detector energy signals and the TAC amplitudes were recorded using 80-MHz synchronized digitizers, without any triggers in a “listmode” data format.

The time difference spectra were analyzed according to the GCD method [5]. Here we present only the aspects of the method needed for the analysis of the data. Please refer to Ref. [5], where the method is discussed in detail. The GCD method takes into account the asymmetric timing of a real γ - γ set-up. Therefore, for a selected feeder-decay combination of a given state, two independent time spectra are produced: the delayed and the antidelayed. The delayed spectrum C_d is produced when the feeder provides the start signal and the decay provides the stop signal. And vice versa, the antidelayed C_a spectrum is produced when the decay provides the start signal and the feeder provides the stop signal. In the simple case where no background is present, the centroids of the two time distributions are displaced by two times the mean lifetime τ of the given state plus an energy dependent time-walk correction, known as the prompt response difference (PRD):

$$C_d - C_a = \Delta C = 2\tau + \text{PRD}. \quad (1)$$

The PRD describes the mean time walk characteristics of the set-up and its energy dependence is determined experimentally by a standard calibration procedure using a ^{152}Eu source [4]. By selecting a feeder-decay combination for a state of known lifetime the delayed and the antidelayed time spectra are produced. Measuring the difference of their centroids ΔC and using Eq. (1), the PRD is obtained. The data points are fitted with the function:

$$\frac{a}{\sqrt{eE_\gamma^2 + b}} + cE_\gamma + d. \quad (2)$$

The resulting curve is presented in Fig. 1. The systematic uncertainty associated with the PRD curve is defined as the

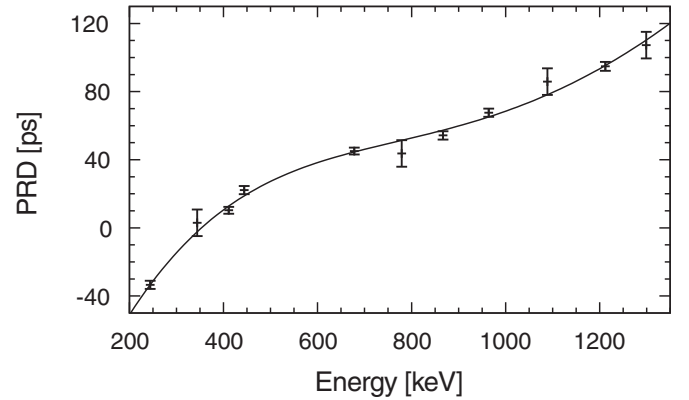


FIG. 1. The PRD curve of the set-up measured with a ^{152}Eu source.

statistical 2σ deviation of the data points from the fitted curve corresponding to 7 ps.

The lifetimes were extracted analyzing triple- γ coincidences. This allows one to set an additional gate on a γ -ray transition observed in a HPGe detector, which reduces the influence of possible contaminant transitions with an energy similar to that of the feeder and/or decay transitions. The peak-to-background ratio in the LaBr detectors, which is inherently low, is also improved, reducing the influence of the time-correlated background. The full projections of the triple coincidences together with a level scheme relevant for the analysis are shown in Fig. 2. The level scheme is adopted from Ref. [6], where the nucleus of interest was populated in the similar $^{208}\text{Pb}(^7\text{Li}, 4n)^{211}\text{At}$ reaction and was confirmed by a γ - γ coincidence analysis using the HPGe detectors.

The doubly gated LaBr and HPGe spectra, relevant for the analysis of the $13/2^-$ state, are shown in Fig. 3(a). The doubly gated HPGe spectrum is generated from HPGe-HPGe-LaBr triple coincidences using the same gates in both cases. Due to the superior resolution of the HPGe detector one can cross-check for undesired transitions with an energy similar to that of the $13/2^- \rightarrow 9/2^-$ transition. By placing a second LaBr gate on the full-energy peak (FEP) of the 1067-keV transition, the delayed and the antidelayed time distributions are obtained and are shown in Fig. 3(b). Measuring the centroid difference and using Eq. (1), one can easily determine the lifetime.

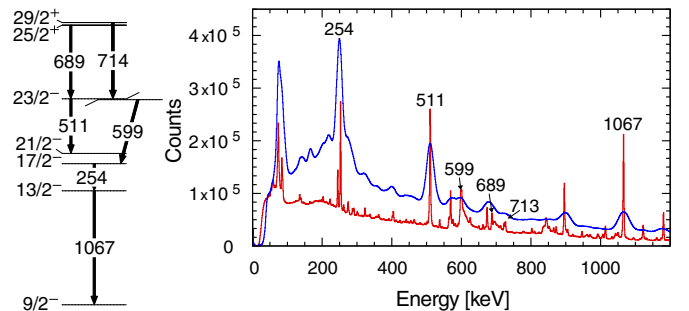


FIG. 2. Right: Partial level scheme of ^{211}At relevant for the analysis adopted from Ref. [6]. Left: Full projections of HPGe-LaBr (blue) and HPGe-HPGe-LaBr (red) coincidence spectra.

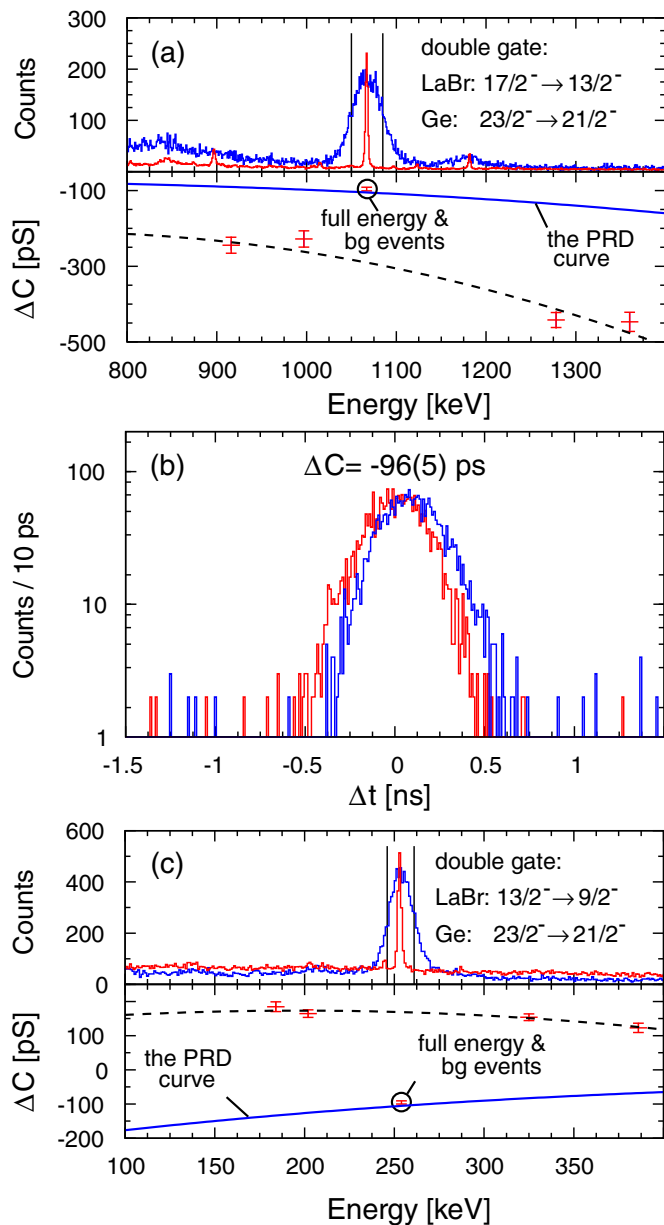


FIG. 3. The figure indicates the basic steps for extracting the lifetime of the $13/2^-$ state. (a) Top: LaBr (blue) and HPGe (red) detector projection in HPGe-LaBr gates, where the gate in the LaBr spectrum is set on the feeder. The vertical lines indicate the gate used to produce the time difference spectra. The corresponding peak-to-background ratio is 11.5. (a) Bottom: The fitted time response of the background (dashed line), together with the PRD curve and the obtained centroid difference from (b). (b) Time-difference spectra for the 254- and 1067-keV feeder-decay combination. (c) Same as (a) but the gate in the LaBr spectrum is set on the decay transition and the analysis of the background is done around the feeder. The corresponding peak-to-background ratio is 10.3.

However, the time distributions contain time-correlated background events, which also contribute when determining the centroid difference ΔC_{exp} . To have a precise lifetime measurement, this contribution has to be deduced and a correction needs to be applied. This is done by placing gates on the

background region on the either side of the FEP of the decay transition to obtain the time response (centroid difference) of the background. The data points obtained are fitted with a quadratic function and the time response of the background at position of the FEP of the decay ΔC_d^{bg} is obtained by interpolation. The fitted time response of the background together with the data points used in the fit, the PRD curve and measured centroid difference ΔC_{exp} are presented in the lower panel of Fig. 3(a). An analogous procedure is performed to obtain the time response of the background ΔC_f^{bg} at the position of the FEP of the feeder. The measured centroid difference ΔC_{exp} is corrected in the following way [7]:

$$\Delta C_{\text{FEP}} = \Delta C_{\text{exp}} + \frac{1}{2} \left[\frac{\Delta C_{\text{exp}} - \Delta C_f^{\text{bg}}}{(p/b)_f} + \frac{\Delta C_{\text{exp}} - \Delta C_d^{\text{bg}}}{(p/b)_d} \right], \quad (3)$$

where $(p/b)_{f,d}$ are the peak-to-background ratios observed in the gates indicated in Fig. 3. After this correction we were able to determine an upper limit of 7 ps for the lifetime of the $13/2^-$ excited state. This limit is considerably lower than the previously known upper limit of 200 ps, which was determined in a fast-timing measurement using HPGe detectors [8].

The lifetime of the $23/2^-$ excited state was determined using the same analysis procedure. The corresponding figures are given in Fig. 4. In order to maximize the statistics in the time spectra an OR gate on the HPGe detectors has been set, using the $13/2^- \rightarrow 9/2^-$ or the $17/2^- \rightarrow 13/2^-$ transition. The resulting lifetime is 56(5) ps. Previously, only an upper limit of 300 ps was known [8].

The lifetime of the $17/2^-$ excited state is long, compared to the time resolution of the set-up, which is ~ 400 ps at this energy. In such a case the time spectrum becomes asymmetric and a slope appears on one side of the prompt peak. The $17/2^-$ state is fed mainly by a 96-keV $E2$ transition from the $21/2^-$ state, which is highly converted, with a conversion coefficient of 9.1, and could not be used in the gamma analysis. Alternatively, we have used a 599-keV transition, which feeds the $17/2^-$ state from a state of unknown spin and parity. This transition has also been observed in Ref. [6]. The doubly gated LaBr and HPGe spectra are shown in Fig. 5(a), where the gate on LaBr detector spectrum has been set on the $17/2^- \rightarrow 13/2^-$ transition. By setting a third gate in the LaBr spectrum, as indicated in the figure, the delayed and the antidelated spectra are obtained. The antidelated time spectrum is inverted and translated on top of the delayed spectrum and the sum of these spectra is shown in Fig. 5(b). An exponential fit to the data points yields a lifetime of 2.14(14) ns. The error indicated includes the systematic error which arises when choosing the fit region and the value of the constant background, and the statistical error obtained when performing the fit, treating these errors as independent variables. Note that this value is very different from the value of $\tau \leq 0.1$ ns [8], adopted in Ref. [9], that would lead to an extremely high value of $B(E2; 17/2^- \rightarrow 13/2^-) \geq 84$ W.u.

The results obtained are summarized in Table I together with the adopted literature values. Reduced transition

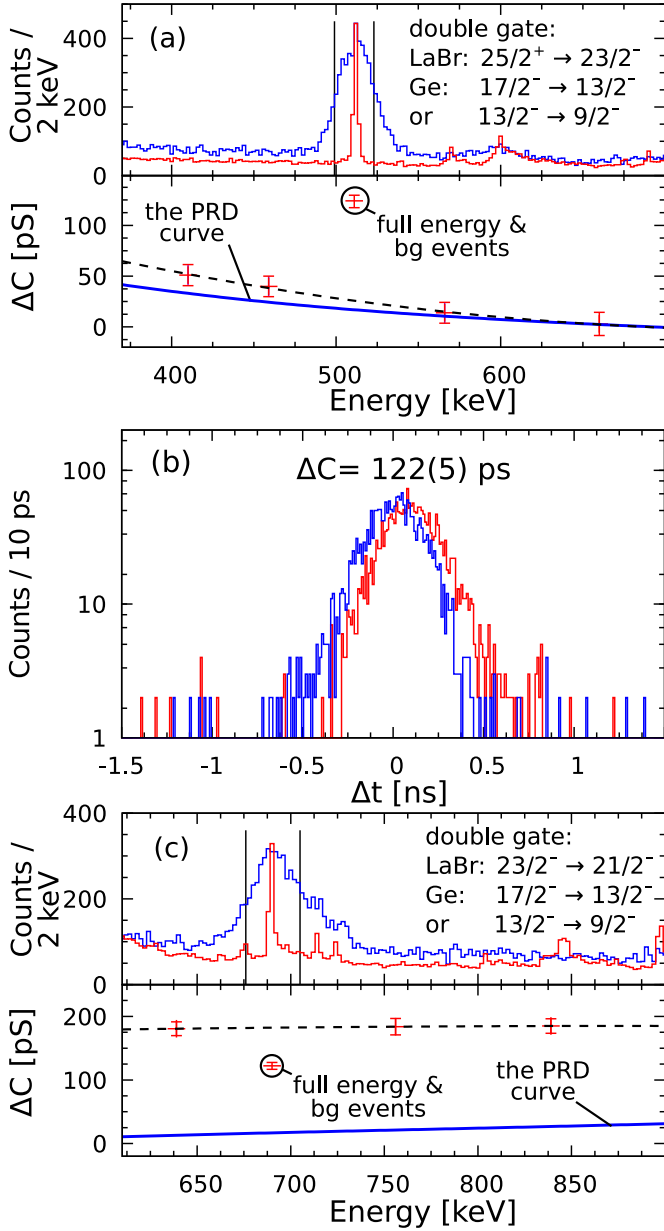


FIG. 4. Analogous to Fig. 3 but for the 23/2⁻ state. The corresponding peak-to-background ratios are 4.7 and 2.1.

probabilities obtained from the new lifetimes are presented in Table II.

III. DISCUSSION

A. Single- j calculation

In this subsection it is assumed that the protons are confined to a single orbital j and that their states are classified in the seniority scheme. In the application to ²¹⁰Po and ²¹¹At the orbital is $0h_{9/2}$ and therefore $j = 9/2$. In the Appendix analytic results are derived relating the observables in a j^2 configuration (e.g., ²¹⁰Po) to those in a j^3 configuration (e.g., ²¹¹At). One is primarily interested in relations between properties of the yrast states, in which case the additional labels [I] can be dropped from Eqs. (A3) and (A7), which can be

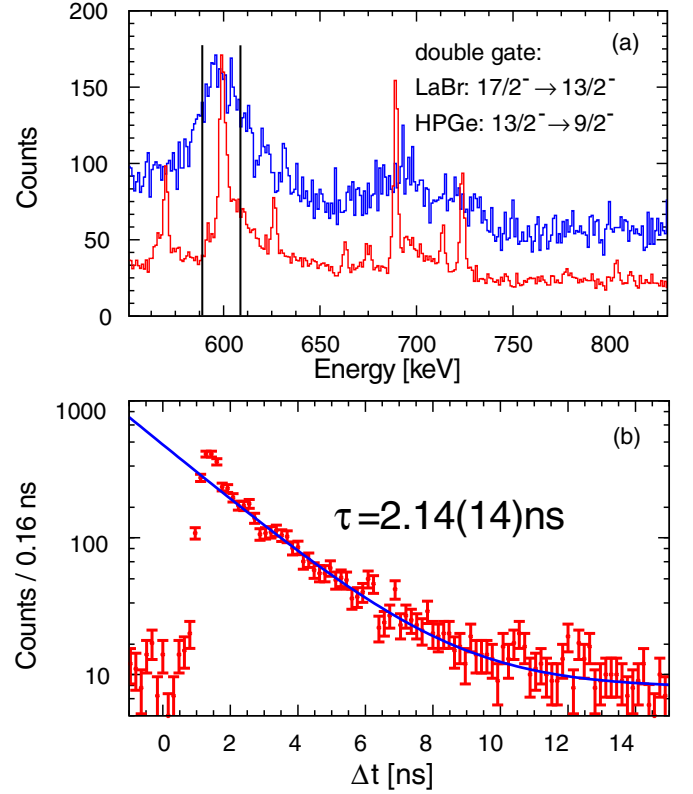


FIG. 5. (a) LaBr (blue) and HPGe (red) detector projection in HPGe-LaBr gates. (b) Time-difference spectrum (see text for details). The line indicates the fit to the data used to extract the lifetime of the 17/2⁻ state.

rewritten as

$$E(j^3J) = \sum_R h_j(J, R) E(j^2R) \quad (4)$$

and

$$B(E2; j^3J_i \rightarrow j^3J_f) = \left(\sum_R g_j(J_i, J_f, R) \sqrt{B_R} \right)^2 \quad (5)$$

with $B_R = B(E2; j^2R \rightarrow j^2R - 2)$, where the quantities on the left-hand side refer to the three-particle nucleus and those on the right-hand side to the two-particle nucleus. For $j \leq 7/2$ all two- and three-particle states are uniquely specified by the angular momentum J . This is also the case for $j = 9/2$, except for three particles with $J = 9/2$, in which case there are two independent states with seniority $\nu = 1$ and 3, respectively. In

TABLE I. Measured lifetimes in ²¹¹At and the feeder and decay energies used to obtain the time-difference spectra. Adopted literature values taken from Ref. [9] are given for comparison.

State J^π	E_{feeder} (keV)	E_{decay} (keV)	HPGe gate (keV)	τ (expt.) (ps)	τ (lit.) (ps)
13/2 ⁻	254	1067	511	≤7	≤200
17/2 ⁻	599	254	1067	2140(140)	≤100
23/2 ⁻	689	511	254 and 1067	56(5)	≤300

TABLE II. Reduced transition probabilities in ^{211}At , deduced from the measured lifetimes. The multiplicities of the transitions are taken from Ref. [9], while the internal conversion coefficients α used in the calculations are obtained using the code BrIccFO [10].

Transition $J_i^\pi \rightarrow J_f^\pi$	E_{decay} (keV)	$B(M1)$ (μ_N^2)	$B(E2)$ ($e^2 \text{fm}^4$)	α
$13/2^- \rightarrow 9/2^-$	1067		≥ 84	0.0070(1)
$17/2^- \rightarrow 13/2^-$	254		300(20)	0.223(4)
$23/2^- \rightarrow 21/2^-$	511	$0.67(6) \times 10^{-2}$		0.131(2)

the following we give the expressions for the $J = 9/2_1$ state and assume it has seniority $\nu = 1$.

The coefficients $h_j(J, R)$ in the energy relation (4) are well known [1] but for completeness they are given here in Table III for $j = 9/2$. The coefficients $g_j(J_i, J_f, R)$ in the $B(E2)$ relation (5) are given in Table IV also for $j = 9/2$.

If the $E2$ operator is of one-body character with a single effective charge, then all $B(E2)$ values can be expressed in terms of a single one, for example, the one associated with the $2_1^+ \rightarrow 0_1^+$ transition in the two-particle nucleus. If, in addition, the interaction conserves seniority, then the relations (5) are satisfied. However, these relations have a wider scope since they also apply if the $B(E2)$ values of the two-particle nucleus cannot be described with a one-body $E2$ operator with a single effective charge. In general, effective charges can be state dependent, which in a two-particle configuration corresponds to two-body components in the operator. In order to eliminate the need for experimental quadrupole moments, the derivation in Appendix, in particular Eq. (A5), assumes that the effective charge entering the calculation of the quadrupole moment of the state $|j^2; R\rangle$ is the same as that for the calculation of the $B(E2; j^2R \rightarrow j^2R - 2)$ value. With this assumption the relations (5) follow.

An application of the j^2-j^3 relations for the case of $j = 7/2$ was presented in Ref. [11] for the nuclei ^{134}Te and ^{135}I . Here we apply the relations to the nuclei ^{210}Po and ^{211}At , where $j = 9/2$. In Table V are shown the excitation energies of the lowest levels in ^{210}Po and ^{211}At . In first approximation they can be described as two and three protons in the $0h_{9/2}$

TABLE III. The coefficients $h_j(J, R)$ in the energy relation (4) for $j = 9/2$.

J	$R = 0$	$R = 2$	$R = 4$	$R = 6$	$R = 8$
$3/2$	–	–	$\frac{24}{11}$	$\frac{9}{11}$	–
$5/2$	–	$\frac{5}{6}$	$\frac{13}{22}$	$\frac{52}{33}$	
$7/2$	–	$\frac{52}{33}$	$\frac{60}{143}$	$\frac{1}{165}$	$\frac{714}{715}$
$9/2_1$	$\frac{4}{5}$	$\frac{1}{4}$	$\frac{9}{20}$	$\frac{13}{20}$	$\frac{17}{20}$
$11/2$	–	$\frac{17}{33}$	$\frac{170}{143}$	$\frac{56}{165}$	$\frac{684}{715}$
$13/2$	–	$\frac{10}{11}$	$\frac{27}{143}$	$\frac{17}{22}$	$\frac{323}{286}$
$15/2$	–	–	$\frac{57}{143}$	$\frac{21}{11}$	$\frac{9}{13}$
$17/2$	–	–	$\frac{125}{143}$	$\frac{57}{110}$	$\frac{209}{130}$
$21/2$	–	–	–	$\frac{7}{10}$	$\frac{23}{10}$

TABLE IV. The coefficients $g_j(J_i, J_f, R)$ in the $B(E2)$ relation (5) for $j = 9/2$.

J_i	J_f	$R = 2$	$R = 4$	$R = 6$	$R = 8$
$3/2$	$5/2$	–	$\frac{307}{121} \sqrt{\frac{2}{35}}$	$\frac{5447}{1650} \sqrt{\frac{1}{11}}$	–
$3/2$	$7/2$	–	$\frac{178}{121} \sqrt{\frac{3}{91}}$	$\frac{61}{275} \sqrt{\frac{2}{2145}}$	$\frac{51}{143} \sqrt{\frac{21}{10}}$
$5/2$	$7/2$	$-\frac{5}{9} \sqrt{\frac{65}{154}}$	$\frac{272}{847} \sqrt{2}$	$\frac{9913}{4950} \sqrt{\frac{1}{385}}$	$\frac{34}{11} \sqrt{\frac{1}{65}}$
$5/2$	$9/2_1$	$\frac{17}{12} \sqrt{\frac{1}{6}}$	$-\frac{13}{22} \sqrt{\frac{39}{770}}$	$\frac{479}{3300} \sqrt{\frac{13}{3}}$	$\frac{17}{2} \sqrt{\frac{1}{231}}$
$7/2$	$9/2_1$	$\frac{269}{132} \sqrt{\frac{13}{165}}$	$\frac{3368}{7865} \sqrt{\frac{3}{7}}$	$\frac{56227}{16500} \sqrt{\frac{1}{330}}$	$\frac{1853}{55} \sqrt{\frac{1}{2730}}$
$11/2$	$7/2$	$\frac{26}{1089} \sqrt{119}$	$\frac{422}{1573} \sqrt{\frac{85}{143}}$	$\frac{36353}{680625} \sqrt{\frac{119}{26}}$	$\frac{278}{3575} \sqrt{\frac{34}{11}}$
$11/2$	$9/2_1$	$\frac{97}{132} \sqrt{\frac{17}{165}}$	$\frac{1049}{15730} \sqrt{\frac{357}{13}}$	$\frac{929}{4125} \sqrt{\frac{17}{4290}}$	$\frac{799}{715} \sqrt{\frac{17}{210}}$
$11/2$	$13/2$	$\frac{5}{242} \sqrt{\frac{1785}{13}}$	$\frac{228}{20449} \sqrt{\frac{51}{11}}$	$\frac{906}{39325} \sqrt{\frac{714}{5}}$	$\frac{57}{11} \sqrt{\frac{51}{1430}}$
$13/2$	$9/2_1$	$\frac{27}{11} \sqrt{\frac{1}{22}}$	$\frac{1359}{1573} \sqrt{\frac{1}{910}}$	$\frac{3067}{1100} \sqrt{\frac{1}{143}}$	$\frac{204}{143} \sqrt{\frac{1}{7}}$
$15/2$	$11/2$	–	$\frac{3043}{40989} \sqrt{\frac{19}{2}}$	$\frac{4034}{10725} \sqrt{\frac{133}{55}}$	$-\frac{9}{572} \sqrt{\frac{19}{65}}$
$15/2$	$13/2$	–	$\frac{3381}{81796} \sqrt{\frac{57}{5}}$	$\frac{333}{14300} \sqrt{\frac{399}{22}}$	$\frac{123}{572} \sqrt{\frac{57}{26}}$
$17/2$	$13/2$	–	$\frac{1855}{1573} \sqrt{\frac{2}{13}}$	$\frac{4891}{3300} \sqrt{\frac{7}{715}}$	$\frac{722}{429} \sqrt{\frac{1}{5}}$
$17/2$	$15/2$	–	$\frac{855}{1573} \sqrt{\frac{7}{442}}$	$-\frac{863}{550} \sqrt{\frac{13}{935}}$	$\frac{753}{26} \sqrt{\frac{1}{595}}$
$21/2$	$17/2$	–	–	$\frac{277}{1250} \sqrt{\frac{77}{26}}$	$\frac{373}{325} \sqrt{\frac{1}{2}}$

orbital, respectively, and therefore the relations (4) with $j = 9/2$ should apply. This is confirmed by the row “Eq. (4)” of Table V. With the exception of $7/2_1^-$ (mainly originating from $1f_{7/2}$), observed and calculated levels are in one-to-one correspondence with deviations in energy of the order of ~ 50 keV. Of interest is that this semiempirical approach gives smaller deviations in energy than the multi- j calculation to be discussed in Sec. III B and shown in Table V under “KHP.”

The measured $B(E2)$ values of the $8_1^+ \rightarrow 6_1^+ \rightarrow 4_1^+ \rightarrow 2_1^+ \rightarrow 0_1^+$ decays in ^{210}Po cannot be explained in a single- j calculation with a constant effective charge. This is illustrated in the first part of Table VI: If the charge is adjusted to the $B(E2; 2_1^+ \rightarrow 0_1^+)$ value, then other $B(E2)$ values are too small by a factor 2. The table also summarizes the $E2$ results for ^{211}At . The second column lists the measured $B(E2)$ values, taken from Refs. [9, 12–14] or from this work. The numbers in the third column are obtained assuming a single- j configuration with a seniority-conserving Hamiltonian with up to two-body interactions and with a one-body $E2$ operator. The first number gives a low estimate based on the $B(E2; 2_1^+ \rightarrow 0_1^+)$ value in ^{210}Po while the second number follows from its $B(E2; 8_1^+ \rightarrow 6_1^+)$ value. Clearly, the two possibilities cover a large range. The fourth column lists the results obtained with Eq. (5), taking the measured $B(E2)$ values and their uncertainties in ^{210}Po in order to estimate the $B(E2)$ values and their uncertainties in ^{211}At . The table also gives the experimental $B(E2; 3/2_1^- \rightarrow 7/2_1^-)$ value in ^{211}At , which is outside the simple j^3 description. With reference to Table IV,

TABLE V. Experimental and calculated excitation energies (in MeV) of levels in ^{210}Po and ^{211}At . Experimental data from Refs. [9,12].

Nucleus		0_1^+	2_1^+	4_1^+	6_1^+	8_1^+						
^{210}Po	Expt.	0.000	1.181	1.427	1.473	1.557						
	KHP	0.000	1.200	1.466	1.482	1.533						
		$9/2_1^-$	$7/2_1^-$	$7/2_2^-$	$5/2_1^-$	$13/2_1^-$	$3/2_1^-$	$11/2_1^-$	$15/2_1^-$	$17/2_1^-$	$21/2_1^-$	$23/2_1^-$
^{211}At	Expt.	0.000	0.674	0.866	0.947	1.067	1.116	1.123	1.270	1.320	1.416	1.927
	Eq. (4)	0.000	–	0.805	0.930	1.021	1.100	1.076	1.241	1.296	1.394	–
	KHP	0.000	0.733	0.928	1.073	1.123	1.282	1.216	1.357	1.391	1.441	1.863

one notes that the first two (if one discards $3/2_1^- \rightarrow 7/2_1^-$) and the last five transitions in ^{211}At have no relation to the $B(E2; 2_1^+ \rightarrow 0_1^+)$ value in ^{210}Po . As a result the high-end estimate in the third column (“Seniority”) is close to the value in the fourth column, obtained with Eq. (5). In contrast, the seven transitions in between (i.e., from $5/2_1^- \rightarrow 7/2_2^-$ to $13/2_1^- \rightarrow 9/2_1^-$) do depend on all four $B(E2)$ values in ^{210}Po , which can lead to a significant difference between the seniority estimate and the one based on Eq. (5). Unfortunately, none of the associated $B(E2)$ values is known experimentally.

TABLE VI. Observed and calculated $B(E2)$ values for transitions in ^{210}Po and ^{211}At .

$J_i^\pi \rightarrow J_f^\pi$	$B(E2; J_i^\pi \rightarrow J_f^\pi) (e^2 \text{fm}^4)$			
	Expt. ^a	Seniority ^e	Eq. (5)	KHP
$2_1^+ \rightarrow 0_1^+$	136(21) ^b	136–264	136(21)	260
$4_1^+ \rightarrow 2_1^+$	331(13)	157–303	331(13)	331
$6_1^+ \rightarrow 4_1^+$	227(5) ^c	109–210	227(5)	227
$8_1^+ \rightarrow 6_1^+$	83(3)	44–83	83(3)	90
$3/2_1^- \rightarrow 5/2_1^-$	955(104)	324–624	678(9)	740
$3/2_1^- \rightarrow 7/2_1^-$	30(3)	–	–	0.7
$3/2_1^- \rightarrow 7/2_2^-$	133(13)	47–89	94(4)	130
$5/2_1^- \rightarrow 7/2_2^-$	–	26–49	83(10)	107
$5/2_1^- \rightarrow 9/2_1^-$	–	143–274	195(12)	279
$7/2_1^- \rightarrow 9/2_1^-$	–	–	–	14.7
$7/2_2^- \rightarrow 9/2_1^-$	–	270–518	419(13)	459
$11/2_1^- \rightarrow 7/2_2^-$	–	60–115	95(6)	102
$11/2_1^- \rightarrow 9/2_1^-$	–	88–170	149(7)	154
$11/2_1^- \rightarrow 13/2_1^-$	–	155–298	266(6)	252
$13/2_1^- \rightarrow 9/2_1^-$	≥ 84 ^d	156–299	226(11)	291
$15/2_1^- \rightarrow 11/2_1^-$	127(22)	80–153	167(4)	169
$15/2_1^- \rightarrow 13/2_1^-$	28(6)	24–46	48(2)	50
$17/2_1^- \rightarrow 13/2_1^-$	300(20) ^d	151–290	306(6)	332
$17/2_1^- \rightarrow 15/2_1^-$	–	46–87	86(4)	82
$21/2_1^- \rightarrow 17/2_1^-$	198(7)	87–167	173(3)	191

^aFrom Refs. [9,12] unless otherwise indicated.^bFrom Ref. [13].^cFrom Ref. [14].^dThis work.^eAssuming conservation of seniority and a one-body $E2$ operator. The low (high) values are obtained adjusting the effective charge to the $2^+ \rightarrow 0^+$ ($8^+ \rightarrow 6^+$) transition in ^{210}Po .

B. Multi- j calculation

Results of interacting SM calculations are presented for the multi- j model space, which includes the proton orbitals $0h_{9/2}$, $1f_{7/2}$, $0i_{13/2}$, $1f_{5/2}$, $2p_{3/2}$, and $2p_{1/2}$. The modified Kuo-Herling particle (KHP) interaction is used, together with the single-particle energies relative to the ^{208}Pb core as given in Ref. [15]. The calculations are performed with the code NuShellX@MSU [16] without any truncation and the results are denoted with “KHP” in the text.

1. Electric quadrupole moments and transitions

Similarly to Ref. [17] we use harmonic oscillator radial wave functions with the parametrization $\hbar\omega = 45A^{-1/3} - 25A^{-2/3}$ MeV with an effective charge $e_\pi = 1.5e$ for calculating $E2$ transitions and quadrupole moments, which seem to overall best reproduce the data. In contrast, in neighboring nuclei with both valence protons and neutrons, the usage of a Woods-Saxon potential may be needed to account for the asymmetry between proton and neutron distributions as done in Ref. [15]. The KHP calculated $B(E2)$ values for the yrast-band transitions in ^{210}Po (see the last column of Table VI) show an almost perfect agreement with the experiment, except for the $B(E2; 2_1^+ \rightarrow 0_1^+)$ value, which is predicted to be about a factor of 2 higher than the experimental one. This is most probably due to the correlations in the 0_1^+ ground state, which are absent from the calculation. Particle-hole (p-h) excitations across the ^{208}Pb core (2p-2h and higher) play an important role in the ground state of ^{210}Po , while the 82–126 model space excludes such configurations and the effect of core excitations is accounted for only partially, i.e., up to 1p-1h, in the KHP interaction [15]. More specifically, in ^{210}Po the KHP calculation yields yrast 2^+ , 4^+ , 6^+ , and 8^+ states with a nearly pure (96 to 100%) $(0h_{9/2})^2$ character, while the 0_1^+ state has a mixed character with dominant configurations of about 69% $(0h_{9/2})^2$, 15% $(0i_{13/2})^2$, and 13% $(1f_{7/2})^2$. The adequacy of the SM wave function for the 6_1^+ and 8_1^+ states in ^{210}Po is supported by the reproduction by KHP of their experimental magnetic moments (see Sec. III B 2). Furthermore, the $B(E2; 6_1^+ \rightarrow 4_1^+)$ and $B(E2; 4_1^+ \rightarrow 2_1^+)$ values are also well reproduced by the KHP interaction, and one may thus assume that the SM description of the 4_1^+ and 2_1^+ states is also good. Therefore, the most plausible explanation of the discrepancy between experimental and SM $B(E2; 2^+ \rightarrow 0^+)$ is the presence of the above-mentioned higher-order core-excitation components in wave function of the ground state of ^{210}Po , which makes the wave-function overlap of the 2^+ state

and the 0^+ ground state smaller, reducing the $B(E2)$, which is not accounted for by the KHP Hamiltonian.

The $B(E2)$ values calculated for transitions in ^{211}At (see Table VI) in general also agree with the experimental values, though a discrepancy is found for the $3/2_1^- \rightarrow 7/2_1^-$ transition. The SM calculates a $3/2_1^-$ with a 97% $(0h_{9/2})^3$ configuration while the $7/2_1^-$ state has dominant components of 73% $(0h_{9/2})^2 1f_{7/2}$, 14% $(0i_{13/2})^2 1f_{7/2}$, and 9% $(1f_{7/2})^3$, i.e., configurations in which a $1f_{7/2}$ proton is coupled to a pair of protons in one of the three lowest orbitals above ^{208}Pb . The $7/2_1^-$ state may thus be described as the coupling of a proton in the $1f_{7/2}$ orbital to the 0_1^+ ground state of ^{210}Po . Therefore, in analogy to the above discussion regarding the structure of the ^{210}Po ground state, one can again argue that the discrepancy between the calculated and measured $B(E2; 3/2_1^- \rightarrow 7/2_1^-)$ value can be explained by the inadequacy of the KHP wave function of the $7/2_1^-$ state in ^{211}At . Extending the analogy further, all states in ^{211}At , which can be described as one valence proton coupled to the ^{210}Po ground state, for example, the $9/2_1^-$ ground state $[(0h_{9/2})_0 \otimes (0h_{9/2})]$ or the $13/2_1^+$ state $[(0h_{9/2})_0 \otimes (i_{13/2})]$, etc., should inherit the deficiency of the KHP wave function of the ^{210}Po ground state, leading to clear deviations between the calculated and experimental transition strengths. Unfortunately, no other relevant experimental results for ^{211}At are currently known to further test the above statement.

For the three lightest $N = 126$ isotones above the ^{208}Pb core, we also have calculated the static quadrupole moments of $(0h_{9/2})^n$ configurations that are maximally aligned in angular momentum, i.e., the $9/2_1^-$ ground state of ^{209}Bi , the 8_1^+ state in ^{210}Po , and the $21/2_1^-$ state in ^{211}At .

In ^{209}Bi , the currently adopted value of $Q(9/2_1^-)$ by the national nuclear data center (NNDC) is $-0.55(1)$ e b [18,19], while the recent compilation of nuclear electric quadrupole moments by Stone [20] recommends a value of $-0.516(15)$ e b [21]. With an effective proton charge $e_\pi = 1.27e$, as suggested for the KHP interaction [15], the calculated value is -0.363 e b, which is very close to the adopted values from earlier times, i.e., -0.38 e b from the 1970s [22] and $-0.370(26)$ e b from the 1980s and 1990s [23]. With $e_\pi = 1.5e$ the KHP calculation yields -0.428 e b, which is lower than the currently adopted and recommended values and which indicates the presence of higher-order np - nh ($n \geq 2$) core excitations, as discussed above and in Refs. [15,24]. On the other hand, the calculated value of -0.428 e b matches quite well the recent more precise value of $-0.420(8)$ e b [25], which has been used recently in the quadrupole moment systematics of $N = 126$ isotones and compared to other SM calculations [26]. Since ^{209}Bi is used as reference isotope for calculating the quadrupole moments of the ground states of $^{202-208,210-213}\text{Bi}$, it would be of great interest to have a common adopted value for ^{209}Bi .

Very recently, the quadrupole moment of the ground state $9/2_1^-$ in ^{211}At was measured to be $-0.33(12)$ {20} b [27], where the statistical error bars are given in round brackets and the estimated systematic ones in curly brackets. Using $e_\pi = 1.5e$ the KHP value for the ^{211}At ground state of -0.266 b agrees with the experimental values within the statistical

uncertainty. We note that the KHP result is identical with the SM calculation in the slightly different SM space [26], because the PBPKE interaction used there comprises the Kuo-Herling two-body matrix elements for $\pi\pi$ and $\nu\nu$. Unfortunately, the large experimental uncertainty prevents drawing further conclusions on the nuclear structure and the amount of possible 2p-2h configurations in the wave function of the ground state of ^{211}At .

The situation concerning the quadrupole moments is much clearer for the 8_1^+ state in ^{210}Po and the $21/2_1^-$ state in ^{211}At . In the KHP calculations these have an almost pure $(0h_{9/2})^n$ configuration. The measured quadrupole moments of the two states are $Q(8_1^+) = (-)0.57(2)$ e b [23] or $-0.55(2)$ e b [20] and $Q(21/2_1^-) = (-)0.524(10)$ e b [20] while the KHP calculations with $e_\pi = 1.5e$ yield -0.580 e b and -0.527 e b, respectively. On the other hand, the quadrupole moment of the 11_1^- state in ^{210}Po , which has a pure maximum aligned $(0h_{9/2} 0i_{13/2})$ configuration in the KHP model space, $Q(11_1^-) = -0.86(11)$ e b, is reproduced with a reduced effective charge $e_\pi = 1.33e$. Practically the same effective charge, $e_\pi = 1.34e$, is needed to reproduce exactly the experimental value of $Q(29/2^+) = 1.00(5)$ e b [9], where the calculated $29/2_1^+$ state has a pure (99,97% in the KHP wave function) maximum aligned $\pi(0h_{9/2} 2 0i_{13/2})$ configuration.

2. Magnetic dipole moments and M1 transitions

Magnetic properties in the ^{208}Pb region have long been addressed. In particular, one should note the theoretical works of Arima, Bauer, Yamazaki, Hamamoto, and others [28–35], who introduce an effective magnetic-moment operator and calculate corrections to the free nucleon g factors due to core polarization and mesonic-exchange currents in nuclei. We first calculate magnetic moments and $M1$ transitions with the average correction factors relative to the free nucleon values, i.e., $\delta_s^\pi = -2.050$, $\delta_s^\nu = 1.800$, $\delta_l^\pi = 0.13$, and $\delta_l^\nu = -0.08$. The nuclei considered here have only valence protons in this model space and the relevant effective g factors for protons are thus $g_s^\pi = 3.536$ and $g_l^\pi = 1.13$. With these effective g factors and the wave functions of the KHP calculation one reproduces very well the magnetic moments of the $9/2_1^-$ ground state in ^{209}Bi , the 6_1^+ , 8_1^+ , and 11_1^- in ^{210}Po , and the $21/2_1^-$ and $29/2_1^+$ in ^{211}At (see Table VII). In contrast to the discussion concerning the quadrupole moments, the effect of the core polarization and meson-exchange currents is explicitly taken into account in the corrections of the g factors [32], thus perfectly reproducing the experimental value of the $\mu(9/2_1^-)$ of ^{209}Bi .

Although the average g -factor corrections by Arima *et al.* [32], in conjunction with the KHP wave functions, are very successful in reproducing static magnetic moments of the listed states, the calculated $M1$ strength for the $23/2_1^- \rightarrow 21/2_1^-$ transition in ^{211}At underestimates the experimental value by a factor of five.

Several comments are in order. The KHP calculation yields $23/2_1^-$ and $21/2_1^-$ states with almost pure configurations of 99.3% $(0h_{9/2})^2 1f_{7/2}$ and 98.5% $(0h_{9/2})^3$, respectively. Thus, $23/2_1^- \rightarrow 21/2_1^-$ corresponds to a proton transition from the $1f_{7/2}$ to the $0h_{9/2}$ orbital, in the presence of another two

TABLE VII. Observed and calculated magnetic moments μ and reduced $B(M1)$ transition probabilities using effective proton g factors $g_s^\pi = 3.536$ and $g_l^\pi = 1.13$.

Nucleus	State or transition	μ (μ_N) or $B(M1)$ (μ_N^2)	
		Expt. ^a	KHP
²⁰⁹ Bi	9/2 ⁻	+4.1103(5)	+4.101
²¹⁰ Po	6 ⁺	5.48(5)	+5.476
	8 ⁺	+7.35(5) ^b	+7.296
	11 ⁻	+12.20(9)	+12.650
²¹¹ At	2 ₂ ⁺ → 2 ₁ ⁺	0.014(7) ^c	0.003
	21/2 ⁻	+9.56(9)	+9.594
	29/2 ⁺	+15.31(13)	+15.841
	23/2 ⁻ → 21/2 ⁻	0.0067(6) ^d	0.0013

^aFrom Nucl. Data Sheets for $A = 209$ [18], $A = 210$ [12], and $A = 211$ [9] unless otherwise indicated.

^bFrom Ref. [36].

^cFrom Ref. [13].

^dThis work.

protons in $0h_{9/2}$, aligned to angular momentum $J = 8$. Note that $1f_{7/2} \rightarrow 0h_{9/2}$ is a spin-flip transition and that $\Delta L = 2$ is not allowed for $M1$ single-particle transitions if only spin and orbital (and no tensor) terms are taken in the $M1$ operator. For example, without tensor term the SM would give a zero $B(M1; 7/2_1^- \rightarrow 9/2_1^-)$ value if this transition in ²⁰⁹Bi is of pure single-particle character. Another $B(M1)$ value which was measured recently in ²¹⁰Po [13] represents the same single-particle $1f_{7/2} \rightarrow 0h_{9/2}$ transition. The KHP calculation predicts that the 2_2^+ state in ²¹⁰Po has a 94% pure $(0h_{9/2}1f_{7/2})$ configuration while the 2_1^+ state is 96% $(0h_{9/2})^2$. The $M1$ branch of the $2_2^+ \rightarrow 2_1^+$ transition in ²¹⁰Po was measured to be $0.014(7) \mu_N^2$ [13]. Similarly to the $M1$ transition in ²¹¹At, the KHP calculations with average g -factor corrections by Arima *et al.* [32] underestimates the $M1$ strength again by about a factor of five (see Table VII).

IV. SUMMARY AND CONCLUSIONS

In summary, we have studied transition strengths between excited states in ²¹¹At, using the electronic γ - γ fast-timing technique following a fusion-evaporation reaction. The lifetimes of the $17/2_1^-$ and $23/2_1^-$ states and an upper limit for the lifetime of the $13/2_1^-$ state were determined and compared to single- and multi- j SM calculations. The formalism for connecting the observables of the j^2 and j^3 configurations has been extended from energy to $B(E2)$ relations and applied to the $\pi 0h_{9/2}$ orbital ($j = 9/2$) above the ²⁰⁸Pb core. It was shown to provide a generally good description of level energies and $E2$ strengths in the j^3 system ²¹¹At, while specific disagreements with experiment, such as an additional $7/2^-$ level at low energy, hint at a more complex structure than just single- j . Furthermore, we have compared large-basis SM calculations with the modified Kuo-Herling particle interaction in the proton $82 \leq Z \leq 126$ model space and effective proton charge $e_\pi = 1.5e$ to experimental energies and $E2$ transition strengths, including the new values, resulting mostly in a very

good agreement. The discrepancies between experiment and KHP calculations or the $B(E2; 2_1^+ \rightarrow 0_1^+)$ value in ²¹⁰Po and the $B(E2; 3/2_1^- \rightarrow 7/2_1^-)$ in ²¹¹At have been discussed and attributed to missing 2p-2h and higher-order core excitations in the SM description of the 0_1^+ state of ²¹⁰Po and the $7/2_1^-$ state of ²¹¹At. Electric quadrupole moments for states with nearly pure $(\pi 0h_{9/2})^n$ configurations were very well reproduced in the KHP calculations with $e_\pi = 1.5e$. The newly measured $B(M1)$ value allowed to test the KHP interaction also for the magnetic transitions. Unlike the very good reproduction of static magnetic moments along the $N = 126$ isotones, the KHP calculations with the effective g factors suggested by Arima *et al.* [32], failed to reproduce the observed $M1$ strength. Most probably an addition of a tensor term in the $M1$ operator will be needed in order to reproduce of the $M1$ strength for the spin-flip transition $\pi 1f_{7/2} \rightarrow \pi 0h_{9/2}$.

ACKNOWLEDGMENTS

J.J. and P.V.I. acknowledge financial support from the Inter-university Attraction Poles Program of the Belgian State-Federal Office for Scientific and Cultural Affairs (IAP Grant P7/12) and from GANIL (Caen France) were the origin of this work was laid. M.S. acknowledges the support by Bulgarian National Science Fund under Grant No. DN08/23/2016. V.K. thanks Georgi Rainovski and Kalin Gladnishki from Sofia University for the helpful discussions during the experiment. Support of the University of Cologne in operating the Tandem accelerator is acknowledged. A.E. and V.K. acknowledge the financial support by the BMBF under Grant No. 05P19PKFNA.

APPENDIX: SINGLE- j SHELL FORMULAS

In this Appendix we derive the formulas necessary for the application to ²¹¹At.

We start with a few elementary properties of antisymmetric three-particle states [1]. A three-particle state can be written as $|j^2(I)j; J\rangle$, where two particles are first coupled to angular momentum I and antisymmetrized in both particles, which is subsequently coupled with the third particle to total angular momentum J . This state is not antisymmetric in all three particles; it can be made so by applying the antisymmetry operator \mathcal{A} ,

$$\mathcal{A}|j^2(I)j; J\rangle \propto |j^3[I]J\rangle = \sum_R c_{j^3[I]J}^{j^2(R)} |j^2(R)j; J\rangle, \quad (\text{A1})$$

where $c_{j^3[I]J}^{j^2(R)} \equiv [j^2(R)jJ|j^3[I]J]$ is a $(3 \rightarrow 2)$ -particle coefficient of fractional parentage (CFP). The notation in round brackets in $|j^2(R)j; J\rangle$ implies coupling of two particles to intermediate angular momentum R . The square brackets $[I]$ label a three-particle state and indicate that it has been obtained after antisymmetrization of $|j^2(I)j; J\rangle$. The label $[I]$ defines an overcomplete, nonorthogonal basis. The states $|j^3[I]J\rangle$ are normalized but not all $I = 0, 2, \dots$ are necessarily independent. The $(3 \rightarrow 2)$ -particle CFP is known in closed form [1].

The expansion (A1) can be used to express matrix elements of a k -body operator $\hat{T}_k^{(\lambda)}$, with $k = 1$ or 2 and where λ is its

tensor character under rotations, between three-particle states in terms of those between two-particle states,

$$\begin{aligned} & \langle j^3[I']J' || \hat{T}_k^{(\lambda)} || j^3[I]J \rangle \\ &= \frac{3}{3-k} (-)^{j+J+\lambda} \sum_{RR'} c_{j^3[I]J}^{j^2(R)} c_{j^3[I']J'}^{j^2(R')} \\ & \times [J][J'] \begin{Bmatrix} J & J' & \lambda \\ R' & R & j \end{Bmatrix} \langle j^2R' || \hat{T}_k^{(\lambda)} || j^2R \rangle, \end{aligned} \quad (\text{A2})$$

where $[x] \equiv \sqrt{2x+1}$.

The result (A2) enables the derivation of relations between properties of the j^2 and j^3 systems. Relations of this kind are well known for energies. Their derivation requires the use of Eq. (A2) with $\lambda = 0$ and $k = 2$, that is, for a two-body interaction $\hat{V} = \hat{T}_2^{(0)}$. If diagonal energies are considered, $I = I'$, then the following relation is obtained:

$$E(j^3[I]J) = 3 \sum_R (c_{j^3[I]J}^{j^2(R)})^2 E(j^2R), \quad (\text{A3})$$

where the notation

$$\begin{aligned} E(j^2R) &\equiv \langle j^2R | \hat{V} | j^2R \rangle, \\ E(j^3[I]J) &\equiv \langle j^3[I]J | \hat{V} | j^3[I]J \rangle, \end{aligned} \quad (\text{A4})$$

is used for the diagonal matrix elements in the two- and three-body systems, respectively. We recall that the relation (A3) is satisfied for a seniority-conserving Hamiltonian with up to two-body interactions in a single- j orbital.

The derivation of relations between electric quadrupole transitions require the use of Eq. (A2) with $\lambda = 2$ and $k = 1$, that is, for a one-body electric quadrupole operator $\hat{T}(E2) = \hat{T}_1^{(2)}$. A relation of this kind is not very useful as it involves both quadrupole moments of and $E2$ transitions between states of the two-particle system. A simplification occurs by noting that the ratio between the ‘‘moment’’ and the

‘‘transition’’ matrix element equals

$$\begin{aligned} & \frac{\langle j^2R || \hat{T}(E2) || j^2R \rangle}{\langle j^2R - 2 || \hat{T}(E2) || j^2R \rangle} \\ &= \frac{[R]}{[R-2]} \begin{Bmatrix} j & j & 2 \\ R & R & j \end{Bmatrix} \begin{Bmatrix} j & j & 2 \\ R-2 & R & j \end{Bmatrix}^{-1} \equiv f_j(R). \end{aligned} \quad (\text{A5})$$

This relation is satisfied for a one-body $E2$ operator in a single- j orbital, independent of whether the interaction conserves seniority or not.

With the help of the ratio (A5) the double sum in Eq. (A2) can be written in terms of the transition matrix elements $\langle j^2R - 2 || \hat{T}(E2) || j^2R \rangle$, which in turn are related to $B(E2)$ values in the two-particle system,

$$\langle j^2R - 2 || \hat{T}(E2) || j^2R \rangle = \sqrt{(2R+1)} B_R, \quad (\text{A6})$$

where $B_R \equiv B(E2; j^2R \rightarrow j^2R - 2)$. The double sum can then be rearranged to give

$$B(E2; j^3[I]J \rightarrow j^3[I']J') = \left[\sum_R g_j(J, I, J', I', R) \sqrt{B_R} \right]^2, \quad (\text{A7})$$

with

$$\begin{aligned} & g_j(J, I, J', I', R) \\ &= \frac{3}{2} [J'] [R] \left[c_{j^3[I']J'}^{j^2(R-2)} c_{j^3[I]J}^{j^2(R)} \begin{Bmatrix} J & J' & 2 \\ R-2 & R & j \end{Bmatrix} \right. \\ & \quad + f_j(R) c_{j^3[I']J'}^{j^2(R)} c_{j^3[I]J}^{j^2(R)} \begin{Bmatrix} J & J' & 2 \\ R & R & j \end{Bmatrix} \\ & \quad \left. + c_{j^3[I']J'}^{j^2(R)} c_{j^3[I]J}^{j^2(R-2)} \begin{Bmatrix} J & J' & 2 \\ R & R-2 & j \end{Bmatrix} \right]. \end{aligned} \quad (\text{A8})$$

Care should be taken to choose a phase convention for the CFPs that is consistent with the choice (A6).

[1] I. Talmi, *Simple Models of Complex Nuclei* (Harwood, Chur, 1993).
 [2] A. Poves and A. Zuker, *Phys. Rep.* **70**, 235 (1981).
 [3] A. Gottardo *et al.*, *Phys. Rev. Lett.* **109**, 162502 (2012).
 [4] J.-M. Régis *et al.*, *Nucl. Instr. Methods A* **823**, 72 (2016).
 [5] J.-M. Régis *et al.*, *Nucl. Instr. Methods A* **726**, 191 (2013).
 [6] S. Bayer, A. P. Byrne, G. D. Dracoulis, A. M. Baxter, T. Kibédi, and F. G. Kondev, *Nucl. Phys. A* **694**, 3 (2001).
 [7] J.-M. Régis, J. Jolie, N. Saed-Samii, N. Warr, M. Pfeiffer, A. Blanc, M. Jentschel, U. Koster, P. Mutti, T. Soldner, G. S. Simpson, F. Drouet, A. Vancraeynest, G. de France, E. Clement, O. Stezowski, C. A. Ur, W. Urban, P. H. Regan, Z. Podolyak, C. Larijani, C. Townsley, R. Carroll, E. Wilson, L. M. Fraile, H. Mach, V. Pazyi, B. Olaizola, V. Vedia, A. M. Bruce, O. J. Roberts, J. F. Smith, M. Scheck, T. Kroll, A. L. Hartig, A. Ignatov, S. Ilieva, S. Lalkovski, W. Korten, N. Marginean, T. Otsuka, N. Shimizu, T. Togashi, and Y. Tsunoda, *Phys. Rev. C* **95**, 054319 (2017).

[8] S. Bayer, A. P. Byrne, and G. D. Dracoulis, *Nucl. Phys. A* **591**, 104 (1995).
 [9] B. Singh, D. Abriola, C. Baglin, V. Demetriou, T. Johnson, E. McCutchan, G. Mukherjee, S. Singh, A. Sonzogni, and J. Tuli, *Nucl. Data Sheets* **114**, 661 (2013).
 [10] T. Kibédi, T. W. Burrows, M. B. Trzhaskovskaya, P. M. Davidson, and C. W. Nestor Jr., *Nucl. Instr. Methods A* **589**, 202 (2008).
 [11] P. Spagnoletti, G. S. Simpson, R. Carroll, J.-M. Régis, A. Blanc, M. Jentschel, U. Koster, P. Mutti, T. Soldner, G. de France, C. A. Ur, W. Urban, A. M. Bruce, F. Drouet, L. M. Fraile, L. P. Gaffney, D. G. Ghita, S. Ilieva, J. Jolie, W. Korten, T. Kroll, C. Larijani, S. Lalkovski, R. Lica, H. Mach, N. Marginean, V. Pazyi, Z. Podolyak, P. H. Regan, M. Scheck, N. Saed-Samii, G. Thiamova, C. Townsley, A. Vancraeynest, V. Vedia, A. Gargano, and P. Van Isacker, *Phys. Rev. C* **95**, 021302 (2017).
 [12] M. S. Basunia, *Nucl. Data Sheets* **121**, 561 (2014).
 [13] D. Kocheva *et al.*, *Eur. Phys. J. A* **53**, 175 (2017).

- [14] O. Häusser, T. K. Alexander, J. R. Beene, E. D. Earle, A. B. McDonald, F. C. Khanna, and I. S. Towner, *Nucl. Phys. A* **273**, 253 (1976).
- [15] E. K. Warburton and B. A. Brown, *Phys. Rev. C* **43**, 602 (1991).
- [16] B. A. Brown and W. D. M. Rae, *Nucl. Data Sheets* **120**, 115 (2014).
- [17] E. Caurier, M. Rejmund, and H. Grawe, *Phys. Rev. C* **67**, 054310 (2003).
- [18] J. Chen and F. G. Kondev, *Nucl. Data Sheets* **126**, 373 (2015).
- [19] J. Dembczyński, B. Arcimowicz, E. Stachowska, and H. Rudnicka-Szuba, *Z. Phys. A* **310**, 27 (1983).
- [20] N. J. Stone, *At. Data Nucl. Data Tables* **111-112**, 1 (2016).
- [21] J. Bieroń and P. Pyykkö, *Phys. Rev. Lett.* **87**, 133003 (2001).
- [22] M. J. Martin, *Nucl. Data Sheets* **22**, 545 (1977).
- [23] P. Raghavan, *At. Data Nucl. Data Tables* **42**, 189 (1989).
- [24] N. A. F. M. Poppelier and P. W. M. Glaudemans, *Z. Phys. A Atomic Nuclei* **329**, 275 (1988).
- [25] T. Q. Teodoro and R. L. A. Haiduke, *Phys. Rev. A* **88**, 052504 (2013).
- [26] R. Ferrer *et al.*, *Nat. Commun.* **8**, 14520 (2017).
- [27] J. G. Cubiss *et al.*, *Phys. Rev. C* **97**, 054327 (2018).
- [28] A. Arima and H. Horie, *Prog. Theor. Phys.* **12**, 623 (1954).
- [29] R. Bauer, J. Speth, V. Klemm, P. Ring, E. Werner, and T. Yamazaki, *Nucl. Phys. A* **209**, 535 (1973).
- [30] T. Yamazaki, *Mesons in Nuclei*, edited by M. Rho and D. H. Wilkinson, Vol. 2 (North-Holland, Amsterdam, 1979), p. 651.
- [31] A. Arima and H. Hyuga, *Mesons in Nuclei*, edited by M. Rho and D. H. Wilkinson, Vol. 2 (North-Holland, Amsterdam, 1979), p. 683.
- [32] A. Arima, K. Shimizu, W. Bentz, and H. Hyuga, *Advances in Nuclear Physics*, edited by E. Vogt and J. W. Negele, Vol. 18 (Plenum, New York, 1987).
- [33] F. Petrovich, *Nucl. Phys. A* **203**, 65 (1973).
- [34] I. Hamamoto, *Phys. Lett. B* **61**, 343 (1976).
- [35] I. S. Towner, F. C. Khanna, and O. Häusser, *Nucl. Phys. A* **277**, 285 (1977).
- [36] N. J. Stone, IAEA Vienna Report No. **INDC(NDS)-0658** (2014).

Pre-print publication:

3 Particle-hole excitations above ^{208}Pb

Particle-hole excitations above ^{208}Pb

V. Karayonchev, A. Blazhev, J. Jolie, A. Dewald, A. Esmaylzadeh, C. Fransen,
G. Häfner, L. Knafla, C. Müller-Gatermann,^a J.-M. Régis, and K. Schomacker
Institut für Kernphysik, Universität zu Köln, 50937 Köln, Germany

G. Rainovski

Faculty of Physics, St. Kliment Ohridski University of Sofia, 1164 Sofia, Bulgaria

P. Van Isacker

Grand Accélérateur National d'Ions Lourds, CEA/DRF-CNRS/IN2P3, Bvd Henri Becquerel, F-14076 Caen, France

(Dated: April 20, 2021)

Lifetimes of low-energy states in the semi-magic nucleus ^{211}At were measured employing the recoil-distance Doppler shift and the Doppler-shift attenuation methods. The deduced transition probabilities are compared to two shell-model calculations, one using the modified Kuo-Herling interaction and the other using a semi-empirical interaction for protons confined to the single-j $0h_{9/2}$ orbital. The Kuo-Herling calculations overestimate some of the ground-state transition probabilities. This has been interpreted as a presence of particle-hole excitation in the ground-state wave function. The good agreement of the data with the calculations performed in the single-j approximation shows that seniority could still be regarded as a good quantum number.

I. INTRODUCTION

The nuclear shell model is the most successful microscopic model of the atomic nucleus. In this model, nucleons are occupying shells that are formed by a central potential, a mean-field, created by the nucleon themselves, with a strong spin-orbital term [1]. A two-body residual interaction, acting between nucleons introduces mixing of the different configurations resulting in a set of new nuclear configurations. A starting point in constructing the residual nuclear interaction is usually a realistic effective nucleon-nucleon potential. Such are the approaches of Kuo and Herling [2] based on the Hamada-Johnson potential [3] and the Bonn model [4]. However, a renormalization is required for the energy regime of nucleons confined to a nucleus, which requires experimental input. The study of nuclei with only a few valence nucleons is the first step in understanding and tuning the nuclear residual interaction. With only a few nucleons, the number of the possible configurations induced by the residual interaction is limited and permits calculations in a full basis. The predictions of the shell model can then be compared to experimental observables to test the adequacy of the used residual interaction. The ^{208}Pb nucleus is the heaviest doubly-magic nucleus. The nuclei in its vicinity have attracted significant experimental and theoretical interest. Experimentally, the nuclei around the stable ^{208}Pb could be accessed relatively easy and there is a large amount of spectroscopic data already available. Theoretically, the fact that ^{208}Pb has a good doubly-magic character has motivated many shell-model calculations [5–9] which were successful at describing the energy spectrum

of the nuclei in the vicinity of ^{208}Pb . Particularly successful has been the residual interaction of Kuo and Herling [2] which has been modified in Ref. [7]. However, the experimental information on the transition probabilities of the nuclei in the region is rather scarce. The transition probabilities are important observables since they are some times sensitive to small contributions in the nuclear wave functions which could not be distinguished by only looking at the energy spectrum of the nuclei. Indeed, recent lifetimes measurements in ^{210}Po [10] and ^{212}Po [11] revealed that the shell model calculation done using the modified Kuo-Herling [7] interaction significantly overestimates the $B(E2; 2_1^+ \rightarrow 0_1^+)$. This has been attributed to the presence of higher-order particle-hole excitations in the ground state of ^{210}Po [12]. To further study the effects of particle-hole excitation, our group has studied the neighboring ^{211}At nucleus in a fusion-evaporation reaction [12]. The $B(E2; 17/2_1^- \rightarrow 13/2_1^-)$ value was determined using the fast-timing technique. However, no firm conclusion was possible based only on this transition probability. In the same study, we have also discussed the ^{211}At nucleus in the framework of shell-model calculations done using a semi-empirical interaction, assuming that the protons are confined only to the $0h_{9/2}$ orbital. The single-j calculations gave a good description of the energy spectrum and could account for the $B(E2; 17/2_1^- \rightarrow 13/2_1^-)$ value. However, the situation for the low-spin states remains unclear. To further investigate the effect of particle-hole excitation on the low-energy structure of the nucleus and to test the adequacy of the single-j calculations, a recoil-distance Doppler-shift (RDDS) and a Doppler-shift attenuation (DSA) lifetime measurements were performed. This paper reports on the measurement of the lifetimes of the $7/2_1^-$, $7/2_2^-$, $5/2_1^-$, $13/2_1^-$, $11/2_1^-$, and $13/2_1^+$ states in ^{211}At .

^a Present address: Physics Division, Argonne National Laboratory, Argonne, Illinois 60439, USA

II. EXPERIMENT

The ^{211}At nucleus was populated in the $^{209}\text{Bi}(^{16}\text{O},^{14}\text{C})^{211}\text{At}$ two-proton transfer reaction. A ^{16}O beam with energy of 84 MeV was provided by the FN-Tandem accelerator at the University of Cologne. The target used for the RDDS experiment was a 1.1-mg/cm^2 ^{209}Bi evaporated on a 0.4 mg/cm^2 Mg backing facing the beam. It was stretched inside the Cologne Plunger device [13] in parallel to a 1.1 mg/cm^2 Mg stopper used to stop the ejecting ^{211}At nuclei. The target used in the DSA measurement was a 0.5 mg/cm^2 ^{209}Bi evaporated on a 1.5 mg/cm^2 Mg backing. γ rays emitted from the targets were detected by eleven high-purity germanium detectors positioned in two rings at 45° and 142° . Recoiling beam-like nuclei were detected by an array of six solar cells placed at backward angles. The data was recorded in triggerless mode and sorted offline. The RDDS data was taken at 6 target-to-stopper distances (32, 42, 57, 77, 127, $327\ \mu\text{m}$) determined relative to a zero point which has been obtained by the capacitive method [13, 14]. These distances were kept constant by the active feed-back system of the Cologne Plunger device [13]. Additionally, data was collected without the active feed-back system, at electrical contact between the target and the stopper, achieving smaller distances than $32\ \mu\text{m}$. This measurement run served as a feasibility test for the later conducted DSA measurement. The particle spectrum observed in the solar cells is displayed in Fig. 1. A clear distinction could be made between the four main channels – the Coulomb excitation of the target, the single-proton, the two-proton, and the α -transfer reactions. A gate set on the group of particles as indicated in Fig. 1 yields a clean γ -ray spectrum of ^{211}At displayed in Fig. 2. The information on the observed γ rays is summarized in Table I. A previously known transition feeding the $17/2_1^-$ state from a state of unknown spin and parity [15] is observed in the experiment and is designated as “A”. The intensity of this transition could not be determined reliably, since it lays on the neutron edge, produced by the $(n,n'\gamma)$ reaction on the ^{74}Ge of the germanium detectors. The intensity of the $23/2_1^- \rightarrow 21/2_1^-$ transition could not be determined either, because the transition energy coincides with the 511-keV annihilation peak commonly present in in-beam γ -ray experiments. Using γ - γ coincidences a level scheme relevant for this experiment has been build and is displayed in Fig. 3.

III. ANALYSIS AND RESULTS

A. RDDS analysis

The RDDS technique in combination with Bateman equations was used to extract the lifetimes longer than 5 ps. For a detailed review of the technique, the reader is

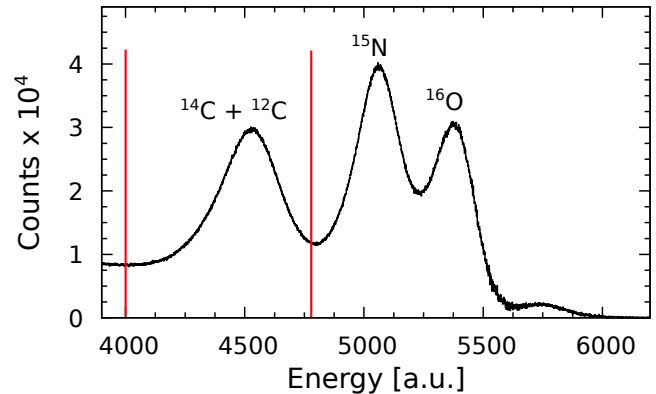


Figure 1. (Color online) Spectrum of back-scattered particles in coincidence with one γ ray obtained during the RDDS experiment. The main reaction products are indicated. The vertical red lines indicate the gate used to obtain the γ -ray spectra used in the experiment.

Table I. γ -ray transitions observed in the $^{209}\text{Bi}(^{16}\text{O},^{14}\text{C})^{211}\text{At}$ reaction. Transition intensities are normalized to the $13/2_1^- \rightarrow 9/2_1^-$ transition intensity.

Index	Transition	Energy [keV]	Intensity
1	$15/2_1^- \rightarrow 11/2_1^-$	147	2.6(10)
2	$15/2_1^- \rightarrow 13/2_1^-$	203	4.0(10)
3	$17/2_1^- \rightarrow 13/2_1^-$	254	44.5(20)
4	$13/2_1^+ \rightarrow 13/2_1^-$	288	5.0(10)
5	$3/2_1^- \rightarrow 7/2_1^-$	442	2.3(10)
6	A $\rightarrow 17/2_1^-$	599	—
7	$7/2_1^- \rightarrow 9/2_1^-$	647	37.0(20)
8	$25/2_1^+ \rightarrow 23/2_1^-$	689	2.0(10)
9	$7/2_2^- \rightarrow 9/2_1^-$	866	12.0(20)
10	$5/2_1^- \rightarrow 9/2_1^-$	947	10.0(15)
11	$13/2_1^- \rightarrow 9/2_1^-$	1067	100.0(6)
12	$11/2_1^- \rightarrow 9/2_1^-$	1123	27.0(20)
13	$13/2_1^+ \rightarrow 9/2_1^-$	1355	10.5(7)
—	$23/2_1^- \rightarrow 21/2_1^-$	511	—

referred to the review article. [13].

The average speed of $v = 1.09(6)\% c$ of the ejected ^{211}At nuclei was determined directly by measuring the Doppler shift of the strongest peaks observed in the experiment. This speed was used to determine the time of flight t between the target and the stopper and was used in the Bateman equations.

When determining the lifetime of a given state using the Bateman equations only the lifetime of the state was used as a fit variable. All other parameters, i.e. the lifetime of the states feeding the state of interest and the feeding intensities were fixed. Accordingly, the lifetimes of the higher-lying states were determined first and were used as fixed parameters when determining the lifetimes

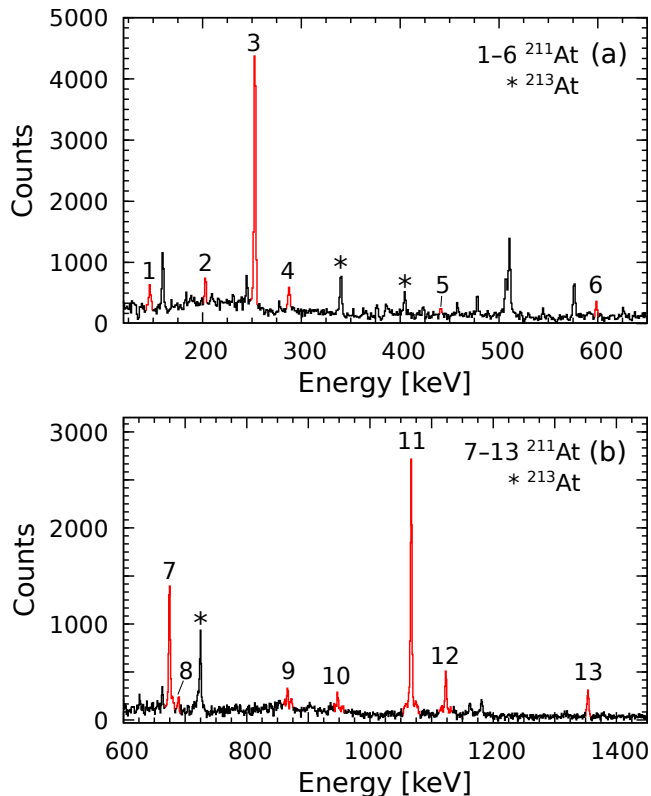


Figure 2. (Color online) Single γ rays of both detector rings in coincidences with the ^{14}C particles, as indicated in Fig. 1, taken at electrical contact. The transitions belonging to ^{211}At are indicated and colored in red. A list of the transitions is given in Table I.

of the lower-lying states. Some of the previously observed low-intensity branchings [15] from states populated in this experiment were not observed explicitly in this experiment but they were taken into account when conducting the lifetime measurements. To obtain the $R(t)$ ratios of a given transition, the shifted and the unshifted components were fitted for each distance using two Gaussian function. The width of the Gaussian functions and their positions were kept constant during the fit for each of the distances. The uncertainties of the ratios include the statistical error and the systematic uncertainty that arise when changing the various fit parameters.

The fit to the data of the $7/2_1^- \rightarrow 9/2_1^-$ transition for three of the distances of the forward detector ring is shown in Fig. 4(a,b,c). Unfortunately, the $9_1^+ \rightarrow 7_1^+$ transition in ^{210}At , which is populated in the $(^{16}\text{O}, ^{13}\text{C})$ reaction has an energy of 675.5 keV, very similar to the energy of the $7/2_1^- \rightarrow 9/2_1^-$ transition in ^{211}At and both peaks appears as a doublet. To obtain the correct intensity of the $7/2_1^- \rightarrow 9/2_1^-$ transition, γ - γ coincidences were sorted. A gate was placed on both the shifted and the unshifted components of the $7_1^+ \rightarrow 5_1^+$ transition in ^{210}At which is in coincidences with the $9_1^+ \rightarrow 7_1^+$ transition. The peak of the $9_1^+ \rightarrow 7_1^+$ transitions appeared

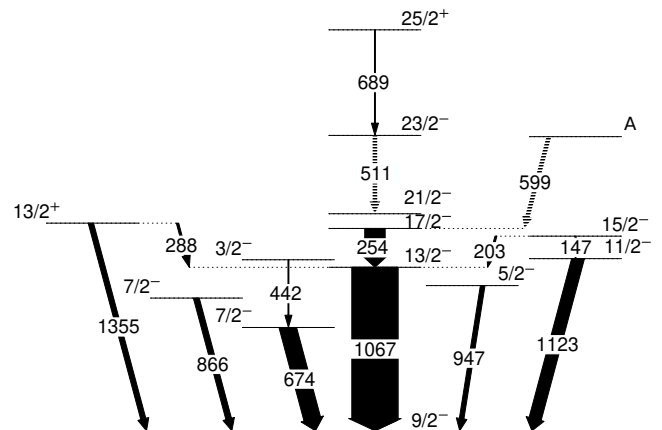


Figure 3. Level scheme of ^{211}At populated in the $^{209}\text{Bi}(^{16}\text{O}, ^{14}\text{C})^{211}\text{At}$ two-proton transfer reaction at 84 MeV beam energy. The line thicknesses are proportional to the γ -ray transition intensities given in Table I.

to be completely stopped and to have no time evolution. Its coincidences intensity has been measured. By measuring the intensity of the $7_1^+ \rightarrow 5_1^+$ transition in the singles spectrum and correcting for the efficiency of the detectors, the singles intensity of the $9_1^+ \rightarrow 7_1^+$ transitions has been determined as 9(2) % of the $7/2_1^- \rightarrow 9/2_1^-$ transition intensity. This can be done because the 7_1^+ decays primarily by the $7_1^+ \rightarrow 5_1^+$ transition [15]. A correction has been applied to the unshifted component of the $7/2_1^- \rightarrow 9/2_1^-$ transition. The corrected data points of the $R(t)$ ratios for all the distances are fitted using the Bateman equations. The fit and the data points are displayed in Fig. 4(d). The feeding coming from the $7/2_2^-$ and the $3/2_1^-$ states was taken into account when determining the lifetime of the $7/2_1^-$ state. The resulting lifetime is 15.5(10) ps. An analogous procedure performed for the backward detector ring yields a lifetime of 14.5(10) ps.

Similarly, the lifetime of the $5/2_1^-$ state was determined using the $5/2_1^- \rightarrow 9/2_1^-$ transition. An analysis was only possible for the forward detector ring due to the presence of an unidentified transition with 936 keV energy. The fits to the spectra used to obtain the decay curve are displayed in Fig. 4(e,f,g), where the 936-keV peak is also seen. The corresponding $R(t)$ ratios are fitted and the result is displayed in Fig. 4(h). The resulting lifetime is 5.4(10) ps. The lifetime of the $13/2_1^+$ has been determined in a similar way. The fit to obtain the $R(t)$ ratios of the forward detector ring is displayed in Fig. 4(i,j,k). The Bateman fit to the data points is displayed in Fig. 4(i) and yields a lifetime of 180(50) ps. The procedure for the backward detector ring gives a lifetime of 260(60) ps. The results of the lifetime analysis using the RDDS technique are summarized in Table II.

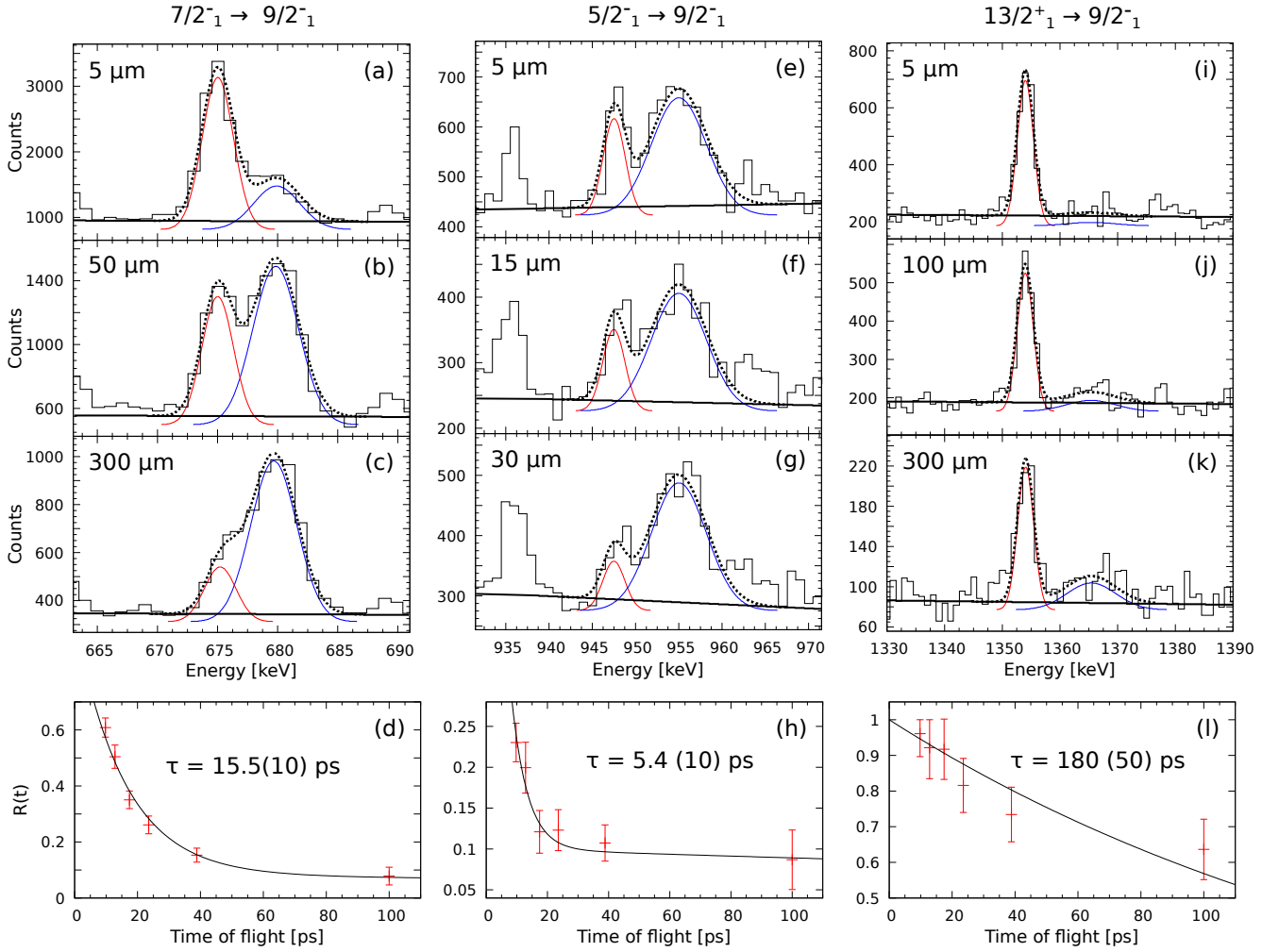


Figure 4. (Color online) (a,b,c) Fits to the $7/2_1^- \rightarrow 9/2_1^-$ transition (dotted black line) of the forward-detector ring for three distances (a,b,c) used to determine the intensity of the shifted (blue solid line) and the unshifted components (red solid line). The black solid line is the background parametrization. (d) The Bateman fit to the obtained $R(t)$ of the $7/2_1^- \rightarrow 9/2_1^-$ transition for all distance used to obtain the lifetime of the $7/2_1^-$ state, together with the obtained lifetime. (e,f,g,h) are same as (a,b,c,d) but for the $5/2_1^-$ state. (i,j,k,l) are same as (a,b,c,d) but for the $13/2_1^+$ state.

B. DSA analysis

The shorter lifetimes were determined using the DSA method. Here only the basic principles of the DSA method are presented. For a detailed review of the method, the reader is referred to Refs. [16, 17].

Excited nuclei produced in the target are allowed to recoil in a stopping material. While slowing down, the nuclei emit γ rays in-flight which appear Doppler shifted in the spectrum of the germanium detectors. Since the slowing down of the nuclei inside the stopper is a continuous process, the γ -ray peak observed in the detectors would display a *Doppler-broadened lineshape*. If the slowing down process of the nuclei is known, the mean lifetime of the excited state emitting the γ rays could be extracted from a fit to the Doppler-broadened lineshape. The DSA analysis was performed using the program APCAD [18].

In APCAD, the stopping of the ^{16}O beam in the target and the stopping of the recoiling ^{211}At ions in the target and the backing are modeled using a Monte-Carlo simulation in the framework of Geant4 [19]. The electronic and nuclear stopping powers are taken from SRIM [20]. The nuclear stopping powers were reduced by 30% to account for microchanneling effects [21]. The doubly-differential cross-section of the $^{209}\text{Bi}(^{16}\text{O}, ^{14}\text{C})^{211}\text{At}$ reaction, which defines the geometry of the reaction, has been calculated using the GRAZING code [22, 23]. After the individual traces of the ^{211}At ions are simulated, APCAD projects the spectra on the detectors, taking into account the detector geometry and resolution and the kinematic restrictions imposed by the solar cells. The resulting *Doppler-broadened lineshapes* are then fitted to the experimental spectra using only the lifetime as a fit parameter. The feeding of the state of interest from other states has also

been taken into account. The uncertainties of the lifetimes determined in the following analysis account for the statistical error during the fit and the systematic errors that arises when assuming 10% uncertainty in the stopping powers and 10% uncertainty in the target thickness. Additionally, the influence of the background parameterization was investigated and was included in the error. In the error determination of the lifetimes, additional slow feeding with intensities up to the observation was also assumed. For the energy region of interest this amount to 1% of the $13/2_1^- \rightarrow 9/2_1^-$ transition intensity. The uncertainty of the lifetimes has been symmetrized by taking the larger of either the low or high uncertainty limits. The lifetime of the $7/2_2^-$ has been determined by performing a DSA fit to the lineshape of the $7/2_2^- \rightarrow 9/2_1^-$ transition. The fits for the forward and the backward detector rings are displayed in Fig. 5(a,b). The resulting lifetimes are 3.0(4) ps and 3.3(4) ps, respectively. Similarly, the lifetimes of the $13/2_1^-$ and $11/2_1^-$ states have been determined by DSA fits to the lineshapes of the $13/2_1^- \rightarrow 9/2_1^-$ and the $11/2_1^- \rightarrow 9/2_1^-$ transitions, respectively. The results of the fits are displayed in Fig. 5(c-f).

The results of the performed lifetime analysis are summarized in Table II. With the newly measured lifetimes and the branching ratios, conversion coefficients, and the multipolarity mixing ratios from Ref. [15], reduced transition probabilities were calculated and are listed in Table III. Due to the large uncertainty of the multipolarity-mixing ratio $\delta = -0.06(18)$ of the $7/2_2^- \rightarrow 7/2_1^-$ transition [24], the reduced transition probability $B(E2, 7/2_2^- \rightarrow 7/2_1^-)$ could not be determined with sufficient accuracy. To obtain a proper value of the $B(E2, 7/2_2^- \rightarrow 7/2_1^-)$ a more accurate measurement of the multipolarity-mixing ratio is needed. There is also a discrepancy in the intensity of the $7/2_2^- \rightarrow 7/2_1^-$ transition. In the fusion-evaporation reactions $^{208}\text{Pb}({}^7\text{Li}, 3n)$ [25] and $^{209}\text{Bi}(\alpha, 2n)$ [26] the branching of this transition has been reported as 4.4(13) and 7.7, respectively, while in the electron capture of ^{211}Rn [27] it has been determined as 11.4(6). The value has been evaluated as 11.4(6) in Ref. [15]. If the evaluated branching ratio is used, a large $B(M1, 7/2_2^- \rightarrow 7/2_1^-) = 0.213_{-0.023}^{+0.027} \mu_N^2$ values is obtained. However, the branching of the $7/2_2^- \rightarrow 7/2_1^-$ transition needs to be corroborated.

IV. DISCUSSION

The newly extracted $B(E2)$ values are compared to two shell-model calculations, one using the modified Kuo-Herling interaction in a multi- j model space and the other using a semi-empirical interaction for three particles in a single $j = 9/2$ shell. The calculations are performed in Ref. [12] and are discussed in detail in the same reference. Here, we only concentrate on discussing the newly acquired reduced transition probabilities. However, it

Table II. Measured lifetimes of excited states in ^{211}At using the RDDS and DSAM methods.

State	Lifetime [ps]		
	Forward	Backward	Adopted
	RDDS		
$7/2_1^-$	15.5(10)	14.5(10)	15.0(7)
$5/2_1^-$	5.4(10)	—	5.4(10)
$13/2_1^+$	180(50)	260(60)	220(80)
	DSAM		
$7/2_2^-$	3.0(4)	3.3(4)	3.15(30)
$13/2_1^-$	2.6(3)	2.6(3)	2.6(2)
$11/2_1^-$	3.3(3)	3.1(3)	3.2(2)

is worth mentioning that both calculations give a good overall description for the energies of the low-lying levels.

A. Single- j calculations

^{211}At is a semi-magic nucleus with three valence protons above a ^{208}Pb core. ^{208}Pb is considered as a good closed-shell nucleus, therefore, it is reasonable to assume that its low-spin structure can be described in a single- j approximation, limiting the model space to three protons in the $0h_{9/2}$ orbital. A shell-model description confined to a single- j orbital has the advantage that simple analytic predictions can be made for the physical properties of the nuclei [32]. If seniority is conserved and operators are of two-body character, the energy spectrum of the three-nucleon system (^{211}At) can be related to that of the two-nucleon system (^{210}Po). This has already been done in Ref. [12] and showed a good agreement with the observed energy spectrum. Similarly, electric quadrupole matrix elements in the three-particle system can be related to those of the two-particle system as:

$$B(E2; j^3 J_i \rightarrow j^3 J_f) = \left(\sum_R g_j(J_i, J_f, R) \sqrt{B_R} \right)^2 \quad (1)$$

with $B_R = B(E2; j^2 R \rightarrow j^2 R - 2)$, where the quantities on the left-hand side refer to the three-particle nucleus and those on the right-hand side to the two-particle nucleus. This relation holds if seniority is conserved and the quadrupole operator is of an one-plus-two-body type [12]. The coefficients $g_j(J_i, J_f, R)$ are given in Ref. [12]. Using Eq. 1, the reduced transition probabilities in ^{211}At have been calculated based on those in ^{210}Po , taking into account the experimental uncertainties. The results are presented in Table III. The newly measured $B(E2)$ values coincide well within the experimental uncertainties with the calculated values. The remarkably good agreement of this simple model with the experiment points out that the assumptions made in the model are to some extent true,

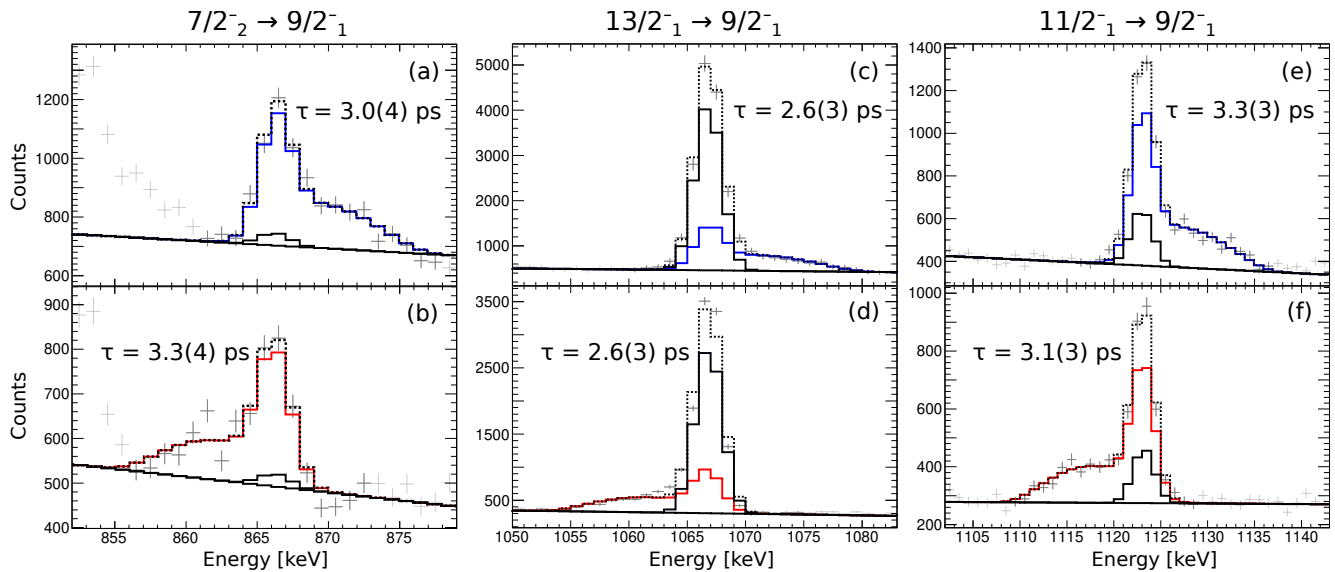


Figure 5. (Color online) (a) DSA fit to the Doppler-broadened lineshape of the $7/2_2^- \rightarrow 9/2_1^-$ transition of the forward detector ring used to determine the lifetimes of the $7/2_2^-$ state. The black solid line is the background parametrization, the solid black peak represents the long-lived feeding of the $7/2_2^-$ state, the blue solid line is the DSA fit to the spectrum excluding the long-lived feeding and the dotted black line is the DSA fit to the data including the long-lived feeding. (b) Same as (a) but for the backward detector ring and the DSA fit excluding the long-lived feeding is a solid red line. (c,d) same as (a,b) but for the $13/2_1^-$ state. (e,f) same as (a,b) but for the $11/2_1^-$ state.

i.e. the nuclear interaction is of a two-body type and conserves seniority, and the electric quadrupole operator $E2$ is of a one-plus-two-body type. A microscopic justification of the above hypothesis can be based on the fact that the Fermi levels for protons which occupy the $0h_{9/2}$ and for the neutrons which occupy the $2p_{1/2}$ orbitals are separated by 3.6 MeV [7, 33]. The large energy difference of the Fermi levels leads to small neutron-proton couplings resulting in parity conservation. Additionally, the two orbitals have a large spin difference, further weakening the proton-neutron interaction.

The $7/2_1^-$ and the $13/2_1^-$ states, which lifetimes have been measured in this experiment are outside the model space of the single- j approximation.

B. Multi- j shell-model calculations

The shell-model calculations are performed using the modified Kuo-Herling particle (KHP) interaction [7] in a multi- j model space, which includes the proton orbitals $0h_{9/2}$, $1f_{7/2}$, $0i_{13/2}$, $1f_{5/2}$, $2p_{3/2}$, and $2p_{1/2}$ above a ^{208}Pb core. The single-particle energies are as given in Ref. [7]. The calculations are performed with the code NuShellX@MSU [34] without any truncation. The results are denoted with ‘KHP’ in the text and are presented in Table. III. The newly measured $B(E2; 7/2_2^- \rightarrow 9/2_1^-)$ and $B(E2; 11/2_1^- \rightarrow 9/2_1^-)$ are described by the KHP calculation even though they are slightly overestimated. The measured $B(E2; 5/2_1^- \rightarrow 9/2_1^-)$ and $B(E2; 13/2_1^- \rightarrow 9/2_1^-)$ values, however, are significantly lower than the

KHP prediction. As stated in Ref. [12], the reason for that could be the presence of particle-hole excitations of 2particle-2hole order and higher which are not included in the KHP model space. Such effects play a role for all $J = 0$ states [7]. The presence of particle-hole excitations of higher-order in the ground state of ^{210}Po was also given as a plausible reason to explain the reduced collectivity of the $2_1^+ \rightarrow 0_1^+$ transition in ^{210}Po , where the KHP calculation overestimates about two times the experimental transition probability. In the case of ^{211}At , the ground state could be presented as a single proton coupled to the ground state of ^{210}Po ($(0h_{9/2}^2)_0 \otimes (0h_{9/2})$). The $13/2_1^- \rightarrow 9/2_1^-$ transition could then be considered as a seniority analog transition to the $2_1^+ \rightarrow 0_1^+$ transition in ^{210}Po and is again overestimated by KHP calculations. However, in this case, the calculated value of $291 e^2 fm^4$ is much closer to the experimental value of $226_{-16}^{+18} e^2 fm^4$. This shows that the effect of the particle-hole excitations of higher order diminishes as more proton-particles are added to the ^{208}Pb core.

An obvious advantage of the single- j description is that any "defects" of the wave function which play a role in the transition probabilities present in the two-particle system are inherently carried over in the three-particle system. As a result, the predictions of the single- j calculations give a better agreement for the reduced transition probabilities than the shell-model calculations done with the KHP residual interaction.

An interesting result comes from the measured lifetime of the $13/2_1^+$ state. Assuming a pure $M2$ transition, the value of $B(M2; 13/2_1^+ \rightarrow 9/2_1^-) = 43_{-11}^{+24} \mu_N^2 fm^2$

Table III. Observed and calculated $B(E2)$ values for transitions in ^{210}Po and ^{211}At . This table has been adopted from Ref. [12] and expanded with the new data.

$J_i^\pi \rightarrow J_f^\pi$	$B(E2; J_i^\pi \rightarrow J_f^\pi) [e^2\text{fm}^4]$		
	Expt ^a	Eq. (1)	KHP
$2_1^+ \rightarrow 0_1^+$	136(21) ^b	136(21)	260
$4_1^+ \rightarrow 2_1^+$	331(13)	331(13)	331
$6_1^+ \rightarrow 4_1^+$	227(5) ^c	227(5)	227
$8_1^+ \rightarrow 6_1^+$	83(3)	83(3)	90
$3/2_1^- \rightarrow 5/2_1^-$	955(104)	678(9)	740
$3/2_1^- \rightarrow 7/2_1^-$	30(3)	—	0.7
$3/2_1^- \rightarrow 7/2_2^-$	133(13)	94(4)	130
$5/2_1^- \rightarrow 7/2_2^-$	—	83(10)	107
$5/2_1^- \rightarrow 9/2_1^-$	198 ⁺⁴⁵ ₋₃₁ ^d	195(12)	279
$7/2_1^- \rightarrow 9/2_1^-$	136 ⁺¹⁹ ₋₁₉ ^d	—	14.7
$7/2_2^- \rightarrow 9/2_1^-$	400 ⁺⁴³ ₋₃₆ ^d	419(13)	459
$11/2_1^- \rightarrow 7/2_2^-$	—	95(6)	102
$11/2_1^- \rightarrow 9/2_1^-$	141 ⁺⁹ ₋₈ ^d	149(7)	154
$11/2_1^- \rightarrow 13/2_1^-$	—	266(6)	252
$13/2_1^- \rightarrow 9/2_1^-$	226 ⁺¹⁹ ₋₁₆ ^d	226(11)	291
$15/2_1^- \rightarrow 11/2_1^-$	127(22)	167(4)	169
$15/2_1^- \rightarrow 13/2_1^-$	28(6)	48(2)	50
$17/2_1^- \rightarrow 13/2_1^-$	300(20) ^e	306(6)	332
$17/2_1^- \rightarrow 15/2_1^-$	—	86(4)	82
$21/2_1^- \rightarrow 17/2_1^-$	198(7)	173(3)	191

^a From Refs. [15, 28] unless otherwise indicated.

^b From Ref. [10].

^c From Ref. [29].

^d This work.

^e From Ref. [12].

has been determined. This value is very similar to the $B(M2; 13/2_1^+ \rightarrow 9/2_1^-) = 38(5) \mu_N^2 fm^2$ in ^{209}Bi obtained in Ref. [35]. Calculations using an effective magnetic operator in the framework of finite Fermi systems give the value $33 \mu_N^2 fm^2$ [36, 37]. The calculations have been performed for a transition between the $0i_{13/2}$ and $0h_{9/2}$ orbitals in ^{209}Bi . This result coincides with both experimental values for ^{209}Bi and ^{211}At . This shows that the addition of two protons to ^{209}Bi does not affect considerably the transition probability of the $13/2_1^+ \rightarrow 9/2_1^-$ transition which in both nuclei could be considered as a single-particle transition between the $0i_{13/2}$ and $0h_{9/2}$ proton orbitals. This argument could be straightened by the fact that the $0i_{13/2}$ orbital is a unique parity orbital and interacts weakly with the rest of the orbitals which results in relatively pure $13/2_1^+$ states in both ^{209}Bi and ^{211}At .

Table IV. Observed and calculated magnetic moments μ and reduced $B(M1)$ transition probabilities, using effective proton g-factors $g_s^\pi = 3.536$ and $g_l^\pi = 1.13$.

Nucleus	State or transition	$\mu[\mu_N]$ or $B(M1)[\mu_N^2] \times 10^{-3}$	
		^a Expt.	KHP
^{209}Bi	$9/2^-$	+4.1103(5)	+4.101
^{210}Po	6^+	5.48(5)	+5.476
	8^+	+7.35(5) ^b	+7.296
	11^-	+12.20(9)	+12.650
	$2_2^+ \rightarrow 2_1^+$	0.014(7) ^c	0.003
^{211}At	$21/2^-$	+9.56(9)	+9.594
	$29/2^+$	+15.31(13)	+15.841
	$23/2^- \rightarrow 21/2^-$	0.0067(6) ^d	0.0013
	$7/2_1^- \rightarrow 9/2_1^-$	9.4(7) ^e	9.3×10^{-2}
	$7/2_2^- \rightarrow 7/2_1^-$	213 ⁺²⁷ ₋₂₃ ^e	2
	$3/2_1^- \rightarrow 5/2^-$	0.23(7)	0.003

^aFrom Nucl. Data Sheets for $A = 209$ [30], $A = 210$ [28] and $A = 211$ [15] unless otherwise indicated.

^bFrom Ref. [31]; ^cFrom Ref. [10]; ^dFrom Ref. [12] ^eThis work.

V. CONCLUSION AND OUTLOOK

Lifetimes of low-energy states in ^{211}At have been measured using the RDDS and DSA methods. The obtained reduced transition probabilities have been compared to two shell-model calculations, using the Kuo-Herling residual interaction and using a single-j approximation. The KHP calculations which account only for single particle-hole excitations significantly overestimate some of the ground state transition probabilities, especially the $B(E2; 13/2_1^- \rightarrow 9/2_1^-)$ value. This discrepancy has been attributed to the presence of the higher-order particle-hole excitation in the wave function of the ground state. These effects are, however, weaker than the ones present in ^{210}Po . The newly obtained reduced transition probabilities are very well described by the single-j shell model calculation. This indicates that seniority could still be regarded as a good quantum number. It would be interesting to continue the same study along the other $N=126$ isotones, where information on the important $B(E2; 2_1^+ \rightarrow 0_1^+)$ and $B(E2; 13/2_1^- \rightarrow 9/2_1^-)$ in even-even and odd-even nuclei, respectively, is still missing.

VI. ACKNOWLEDGMENTS

JJ and PVI acknowledge financial support from the Inter-university Attraction Poles Program of the Belgian State-Federal Office for Scientific and Cultural Affairs (IAP Grant P7/12) and from GANIL (Caen France) where the origin of this work was laid. GR acknowledges

the support by BGNSF under grant DN08/23/2016.

Support of the University of Cologne in operating the Tandem accelerator is acknowledged.

-
- [1] Maria Goeppert Mayer, *Phys. Rev.* **78**, 16 (1950).
- [2] G.H. Herling and T.T.S. Kuo, *Nuc. Phys. A* **181**, 113 (1972).
- [3] T. Hamada and I.D. Johnston, *Nuc. Phys.* **34**, 382 (1962).
- [4] R. Machleidt, K. Holinde, and Ch. Elster, *Phys. Rep.* **149**, 1 (1987).
- [5] J.B. McGrory and T.T.S. Kuo, *Nucl. Phys. A* **247**, 283 (1975).
- [6] T.R. McGoram, G.D. Dracoulis, A.P. Byrne, A.R. Poletti, and S. Bayer, *Nucl. Phys. A* **637**, 469 (1998).
- [7] E. K. Warburton and B. A. Brown, *Phys. Rev. C* **43**, 602 (1991).
- [8] L. Coraggio, A. Covello, A. Gargano, N. Itaco, and T. T. S. Kuo, *Phys. Rev. C* **58**, 3346 (1998).
- [9] E. Caurier, M. Rejmund, and H. Grawe, *Phys. Rev. C* **67**, 054310 (2003).
- [10] D. Kocheva *et al.*, *Eur. Phys. J. A* **53**, 175 (2017).
- [11] D. Kocheva *et al.*, *Phys. Rev. C* **96**, 044305 (2017).
- [12] V. Karayonchev, A. Blazhev, A. Esmaylzadeh, J. Jolie, M. Dannhoff, F. Diel, F. Dunkel, C. Fransen, L. M. Gerhard, R.-B. Gerst, L. Knafla, L. Kornwebel, C. Müller-Gatermann, J.-M. Régis, N. Warr, K. O. Zell, M. Stoyanova, and P. Van Isacker, *Phys. Rev. C* **99**, 024326 (2019).
- [13] A. Dewald, O. Möller, and P. Petkov, *Progr. Part. Nucl. Phys.* **67**, 786 (2012).
- [14] T.K. Alexander and A. Bell, *Nucl. Instr. Meth.* **81**, 22 (1970).
- [15] B. Singh, D. Abriola, C. Baglin, V. Demetriou, T. Johnson, E. McCutchan, G. Mukherjee, S. Singh, A. Sonzogni, and J. Tuli, *Nucl. Data Sheets* **114**, 661 (2013).
- [16] D.B. Fossan and E.K. Warburton, in *Nuclear Spectroscopy and Reactions, Part C*, Vol. 40 (Elsevier, 1974) p. 307.
- [17] P. J. Nolan and J. F. Sharpey-Schafer, *Rep. Prog. Phys.* **42**, 1 (1979).
- [18] C. Stahl, J. Leske, M. Lettmann, and N. Pietralla, *Comp. Phys. Comm.* **214**, 174 (2017).
- [19] S. Agostinelli *et al.*, *Nucl. Inst. Meth. Phys. Res. Sect. A* **506**, 250 (2003).
- [20] J. F. Ziegler, M.D. Ziegler, and J.P. Biersack, *Nucl. Inst. Meth. Phys. Res. Sect. A* **268**, 1818 (2010).
- [21] J. Keinonen, AIP Conf. Proc. , 557 (1985).
- [22] A. Winther, *Nucl. Phys. A* **572**, 191 (1994).
- [23] R. Yanez and W. Loveland, *Phys. Rev. C* **91**, 044608 (2015).
- [24] D Venos, I Adam, N A Bonch-Osmolovskaja, P Caloun, K I Erohina, Y I Isakov, O D Kjostarova, V A Morozov, Ju V Norseev, and V I Stegajlov, *J. Phys. G* **16**, 1009 (1990).
- [25] S. Bayer, A.P. Byrne, G.D. Dracoulis, A.M. Baxter, T. Kibédi, and F.G. Kondev, *Nucl. Phys. A* **694**, 3 (2001).
- [26] I. Bergström, B. Fant, C.J. Herrlander, P. Thieberger, K. Wikström, and G. Astner, *Phys. Lett. B* **32**, 476 (1970).
- [27] G Astner, *Phys. Scr.* **5**, 31 (1972).
- [28] M. Shamsuzzoha Basunia, *Nuclear Data Sheets* **121**, 561 (2014).
- [29] O. Häusser, T.K. Alexander, J.R. Beene, E.D. Earle, A.B. McDonald, F.C. Khanna, and I.S. Towner, *Nucl. Phys. A* **273**, 253 (1976).
- [30] J. Chen and F.G. Kondev, *Nuclear Data Sheets* **126**, 373 (2015).
- [31] N. J. Stone, IAEA Vienna Report No. **INDC(NDS)-0658** (2014).
- [32] I. Talmi, *Simple Models of Complex Nuclei* (Harwood, Chur, 1993).
- [33] M. Stoyanova *et al.*, *Phys. Rev. C* **100**, 064304 (2019).
- [34] B.A. Brown and W.D.M. Rae, *Nuclear Data Sheets* **120**, 115 (2014).
- [35] O. J. Roberts *et al.*, *Phys. Rev. C* **93**, 014309 (2016).
- [36] P. Ring, R. Bauer, and J. Speth, *Nucl. Phys. A* **206**, 97 (1973).
- [37] R. Bauer, J. Speth, V. Klemm, P. Ring, E. Werner, and T. Yamazaki, *Nucl. Phys. A* **209**, 535 (1973).

Provisionally accepted publication:

4 Lifetimes and structures of low-lying
negative-parity states of ^{209}Po

Lifetimes and structures of low-lying negative-parity states of ^{209}Po

V. Karayonchev,¹ M. Stoyanova,² G. Rainovski,^{2,*} J. Jolie,¹ A. Blazhev,¹
 M. Djongolov,² A. Esmaylzadeh,¹ C. Fransen,¹ K. Gladnishki,² L. Knafla,¹
 D. Kocheva,² L. Kornwebel,¹ J. -M. Régis,¹ G. De Gregorio,^{3,4} and A. Gargano⁴

¹*Institut für Kernphysik, Universität zu Köln, 50937 Köln, Germany*

²*Faculty of Physics, St. Kliment Ohridski University of Sofia, 1164 Sofia, Bulgaria*

³*Dipartimento di Matematica e Fisica,*

Università degli Studi della Campania "Luigi Vanvitelli", I-81100 Caserta, Italy

⁴*INFN Sezione di Napoli, IT-80126 Napoli, Italy*

(Dated: December 20, 2020)

Abstract

The $5/2_1^-$, $9/2_1^-$ and $11/2_1^-$ states in ^{209}Po were populated in the β decay of ^{209}At and their lifetimes measured using the electronic $\gamma-\gamma$ fast timing technique. The lifetime of the $9/2_1^-$ state is measured for first time. The lifetime of the $5/2_1^-$ is measured to be shorter than the value adopted in the literature while the lifetime of the $11/2_1^-$ state agrees well with the previous measurement. In order to get deeper insight into the structure of the states, a shell-model calculation was carried out adopting a microscopic effective interaction derived from the realistic CD-Bonn potential. The comparison between theoretical and experimental data for the low-lying negative-parity states of ^{209}Po supports the reliability of the predicted wave functions, which are found to be dominated by the coupling of a neutron hole to the yrast states of ^{210}Po . However, it also points to the important role played by minor wave-function components in describing the reduced electromagnetic strengths, suggesting the need of additional configuration mixing for achieving a better quantitative agreement.

PACS numbers: 21.10.Tg, 21.60.Cs, 23.20.-g, 27.80.+w

*rig@phys.uni-sofia.bg

I. INTRODUCTION

One of the main tasks of modern nuclear structure studies is to seek a comprehensive description of nuclei by simultaneously explaining the rich variety of single-particle and collective phenomena they exhibit. In this regard, it is of particular interest to understand the development of collectivity starting from microscopic degrees of freedom.

A successful framework for microscopic nuclear structure calculations is the shell model, which is based on the assumption that nucleons move independently in a central mean field with a strong spin-orbit term giving rise to the observed shell structure and the corresponding magic numbers [1, 2]. Within this model the valence nucleons external to the filled shells interact through the two-body residual interaction (the part of the interaction that is not absorbed into the central potential), which induces a mixing of different configurations. It is well known that the proton-neutron component of the residual interaction tends to drive collective behaviors, and collectivity emerges when this component, which increases with the number of valence protons and neutrons [3], overcomes the pairing interaction [4]. In this context, the evolution of the nuclear states with the number of valence nucleons from single-particle configurations towards multi-configurational mixture is a matter of great relevance, which may give important information on the properties of the interaction in nuclear medium.

The initial step in addressing this question is to understand the structure of low-lying states of nuclei in the vicinity of shell closures. In fact, nuclei with only few valence protons and neutrons particles (or holes) provide a suitable ground for testing and tuning residual interactions used in the shell-model calculations. They can be particularly useful when interactions are derived within a microscopic approach from realistic nucleon-nucleon potentials, which do not contain free parameters fixed to reproduce experimental data.

The nuclei in the vicinity of the doubly magic nucleus ^{208}Pb have attracted significant interest over the years. In particular, many shell-model calculations have been performed in this region [5–14], motivated by the fact that ^{208}Pb is considered to be a good closed core [5]. It has to be stressed, however, that most of these studies are focused on semi-magic lead nuclei or on semi-magic $N = 126$ isotones [5, 7–11]. Furthermore, in the cases where open-shell nuclei are considered, shell-model calculations are based on empirical interactions [6] and usually focused on the structure of the high-spin isomers [8]. As a matter of fact, the

nature of low-spin states of nuclei in the vicinity of ^{208}Pb is still poorly understood, as it was noticed long ago in Ref. [15]. This is due partially to the lack of experimental data, especially on the electromagnetic transition rates. For example, the yrast states of even-even polonium isotopes are thought to be built on the $\pi(h_{9/2})^2$ configuration. This is in agreement with the available experimental data for the 8_1^+ and 6_1^+ states which can be well described in the framework of the shell model with phenomenological interactions [16, 17]. However, even in ^{210}Po , where all transition strengths for the yrast states are experimentally well known [18], no consistent description which includes the $B(E2; 2_1^+ \rightarrow 0_1^+)$ exists [11, 18]. For ^{208}Po no experimental data on the $E2$ transitions strengths from the 4_1^+ and 2_1^+ states are available, while in $^{204,206}\text{Po}$ there are experimental indications that the 4_1^+ and 2_1^+ states are already of collective nature [19].

To fill the gap in the evolution between the states of single-particle seniority-type character in ^{210}Po and those of collective nature in $^{204,206}\text{Po}$, we have studied the low-lying negative-parity states of ^{209}Po . The properties of these states may provide information on the increased collectivity with respect to ^{210}Po as it has been demonstrated recently in the case of ^{129}Sb by observing total electric quadrupole strength significantly larger than in the ^{128}Sn core [20].

The ^{209}Po nucleus has been studied extensively in the past mainly through the electron-capture decay of ^{209}At (see Refs. [21, 22] and the references therein). Therefore, its level scheme is well established with the spin-parity assignment of the states based mostly on measured electron conversion coefficients [21, 22]. In particular, the $17/2_1^-$ isomeric state at 1472 keV has been discovered by Yamazaki and Matthias [23] and its lifetime has been measured precisely by Hüsser *et al.* [24], while the lifetimes of the $5/2_1^-$, the $13/2_1^-$ and the $11/2_1^-$ states have been reported in Ref. [21]. Alpsten *et al.* [21] have interpreted these results in the framework of semi-realistic shell-model calculations [25], which suggest that the low-lying negative-parity states of ^{209}Po arise from a weak coupling of a single neutron hole to the excited states of ^{210}Po . This interpretation is in overall agreement with the available experimental data on the magnetic dipole moments [24] and the electric quadrupole moments [26] of the isomeric $13/2_1^-$ and $17/2_1^-$ states. However, all previous studies [21–24] also suggest that contributions of minor components in the wave functions of the low-lying negative-parity states of ^{209}Po may play an important role, especially for the description of the electromagnetic properties.

To clarify further the role of the configuration mixing in the structure of low-lying negative parity states of ^{209}Po , more experimental data on electromagnetic transition strengths for states other than the isomeric ones are needed. Moreover, the comparison with the theoretical results would also provide a good test for the realistic interactions used in shell-model calculations. However, the lifetimes of these states are expected to be in order of few tens of picoseconds and their precise determination has not been possible in the past.

Nowadays, with the development of the ultra-fast timing technique for γ -ray coincidence spectroscopy [27] which is based on fast $\text{LaBr}_3(\text{Ce})$ scintillator detectors with high energy resolution [28], such measurements have become possible. It is the purpose of the present study to measure the lifetimes of the the low-lying negative-parity states of ^{209}Po by utilizing the electronic $\gamma - \gamma$ fast timing technique and thus to provide data for testing shell-model calculations based on a realistic interaction.

II. EXPERIMENT

The experiment was performed at the FN-Tandem facility of the University of Cologne. The isotope ^{209}Po was populated after the successive alpha and electron capture (e.c.) decay of ^{213}Fr which was produced in the $^{206}\text{Pb}(^{11}\text{B},4n)^{213}\text{Fr}$ fusion-evaporation reaction at a beam energy of 56 MeV. The target consists of a ^{206}Pb foil with a thickness of 14.5 mg/cm^2 on a 130 mg/cm^2 gold backing, the latter being used to stop the beam in order to prevent further reactions in the reaction chamber. The γ rays were detected by a mixed array consisting of 8 HPGe detectors and 12 LaBr scintillators mounted at the Cologne HORUS spectrometer. To suppress the Compton background, six of the LaBr detectors were placed inside bismuth-germanate oxide (BGO) anti-Compton shields. The other LaBr detectors had lead shields to suppress background events associated with scattered γ rays. The time differences of every unique combination of LaBr detectors were recorded using time to amplitude converters (TAC) applying the multiplexed-start and multiplexed-stop electronics setup [29]. The target was activated for a period of 90 h at an average beam current of 1.8 pA. Afterwards, the decay data were acquired off-beam for a period of 100 h. The detector energy signals and the TAC amplitudes were recorded without triggers in a list-mode format. These data were used in the following analysis.

The full projection of HPGe-HPGe coincidence data is displayed in Fig. 1(a). The α

decay of ^{213}Fr ($T_{1/2} = 34.14(6)$ s) leads almost exclusively (99.44(5)%) [30] to the ground state ($J^\pi = 9/2^-$) of ^{209}At . ^{209}At decays ($T_{1/2} = 5.42(5)$ h) mainly via electron capture (95.9(5)%) [31] to excited states of ^{209}Po . The γ rays from the decays of these states, are delineated in red in Fig. 1(a). The transitions in blue are from the decays of the excited states of ^{210}Po which is produced in a similar way from the 3n channel of the fusion-evaporation reaction. All γ rays, observed in coincidence with the $5/2_1^- \rightarrow 1/2_{1(g.s)}^-$ transition in ^{209}Po (cf. Fig. 1(b)), are from known transitions in ^{209}Po [31]. A partial level scheme of ^{209}Po summarizing the observed γ transitions and their coincidence relationship is shown in the inlay of Fig. 1(b).

The lifetimes were extracted using the fast-timing technique by applying the Generalized Centroid Difference (GCD) method [32]. In this analysis, an asymmetric timing of the γ - γ fast-timing setup is considered. In this case for a given feeder-decay combination of a certain state two independent time-difference spectra are generated. When a feeding transition provides the start signal and the decay transition provides the stop signal, the delayed spectrum is produced. Conversely, when the decay transition provides the start signal and the feeding transition the stop signal, the anti-delayed spectrum is produced. In the case where no background is present, the centroids of the delayed and the anti-delayed time distributions are shifted by two times the mean lifetime τ of the state plus an energy-dependent time-walk characteristics of the setup, dubbed Prompt Response Difference (PRD) [33]:

$$C_d - C_a = \Delta C = 2\tau + PRD, \quad (1)$$

here C_d and C_a are the centroids of the delayed anti-delayed time distributions. The PRD describes the combined mean time-walk characteristics of the fast-timing setup. Its energy dependence is determined by a standard calibration procedure using a ^{152}Eu source [33]. By selecting a feeder-decay combination of a state with a known lifetime the delayed and the anti-delayed time-difference spectra are generated. By measuring the centroid difference ΔC and using Eq. (1) the PRD is obtained. The data points are fitted with the function [33]:

$$PRD(E_\gamma) = \frac{a}{\sqrt{E_\gamma + b}} + cE_\gamma + d \quad (2)$$

The result of the fit is presented in Fig. 2. The systematic uncertainty of the the PRD is defined as two times the standard root-mean-squared deviation (2σ), corresponding to 4 ps.

When extracting the lifetimes triple HPGe-LaBr-LaBr coincidences were used. The additional HPGe gate allows a γ cascade to be selected precisely, reducing the influence of

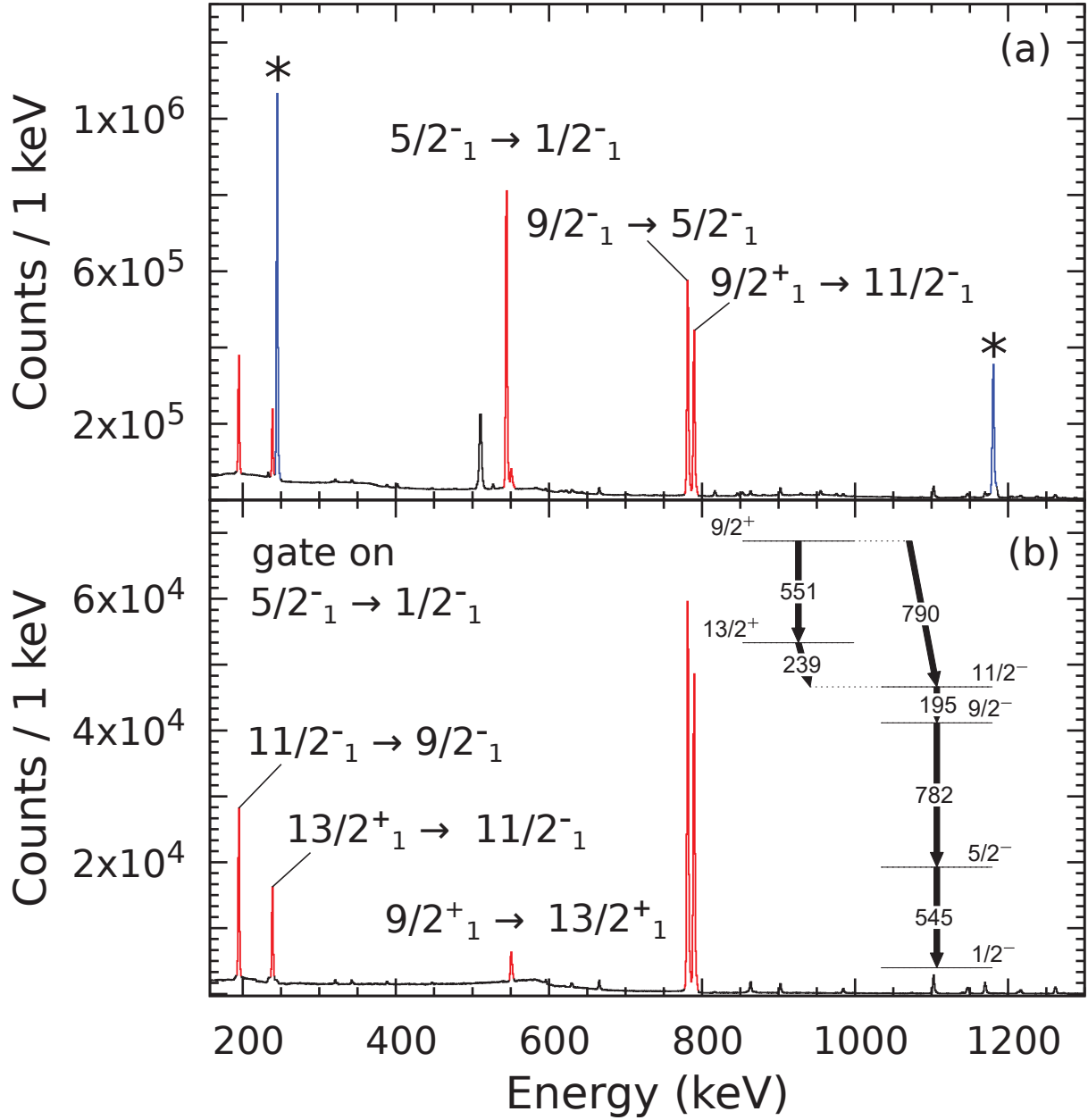


FIG. 1: (Color online) (a) The full projections of off-beam HPGe-HPGe coincidence data. (b) γ spectrum in coincidence with the $5/2^-_1 \rightarrow 1/2^-_1$ transition in ^{209}Po , together with a level scheme of ^{209}Po populated in the e.c. decay of ^{209}At . Transitions belonging to the ^{209}Po are indicated and colored in red. Transitions belonging to ^{210}Po are indicated with an asterisks and colored in blue.

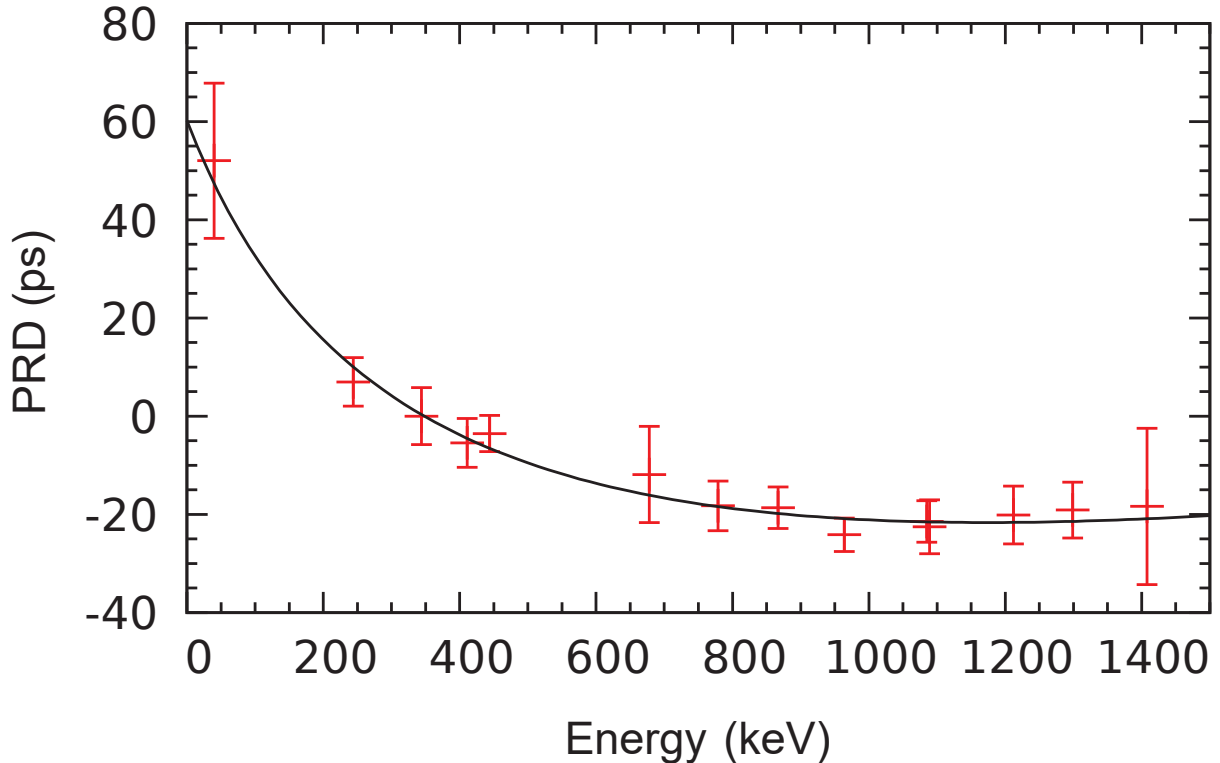


FIG. 2: (Color online) The prompt response difference (PRD) of the setup, together with the data points used to fit the curve. The calibration was performed with a ^{152}Eu source.

unwanted transitions. In addition, the peak to background ratio in the LaBr detectors is also improved thus reducing the impact of the time-correlated background.

The doubly gated LaBr spectrum, relevant for the analysis of the $5/2_1^-$ state, is shown in Fig. 3(a). Here the LaBr gate is placed on the decay transition. Additionally, doubly gated HPGe spectrum is generated from HPGe-HPGe-LaBr triple coincidences. The high resolution of the HPGe spectrum generated under the same coincidence conditions allows for a check for unwanted contaminant transitions which would not be otherwise resolved by the LaBr scintillators. After placing a second gate in the LaBr spectrum on the feeding transition as indicated in Fig. 3(a) the time difference spectra are generated and displayed in Fig. 3(c). Measuring the centroid difference ΔC between the delayed and the anti-delayed spectra and using Eq. 1, a lifetime of $66(5)$ ps is obtained. An analogous investigation is performed using the spectra generated when the first LaBr gate is placed on the feeding transition (see Fig. 3(b)). In both cases, the same two LaBr gates are used resulting in the same time distributions displayed in Fig. 3(c). The background contributions under

the full-energy peaks (FEP) of both the feeder and the decay are very low therefore no time-correlated background correction is necessary.

Using the same procedure, the lifetime of the $9/2_1^-$ and the $11/2_1^-$ states were extracted. The corresponding spectra are presented in Fig. 3(d,e,f) and Fig. 3(g,h,i), respectively. Even though, all the spectra are very clean there is a small background contribution under the 195-keV transition ($11/2_1^- \rightarrow 9/2_1^-$). In this case the measured the centroid difference ΔC cannot be used directly for determining the lifetimes since it contains contributions from the time-correlated Compton background which comes from the counts underneath the full energy peaks (FEP's). A correction for these contributions can be done by sampling the time response of the background at several positions on either side of the FEP of the decay transition [34]. The data points are then fitted and extrapolated to the position of the FEP to obtain the response of the background under the decay peak ΔC_d^{bg} . The same procedure is applied for the background around the FEP of the feeding transition to obtain ΔC_f^{bg} . The correction to the measured centroid ΔC_{exp} difference is applied according to the formula [34]:

$$\begin{aligned} \Delta C &= \Delta C_{exp} + \Delta C_{corr}, \\ \Delta C_{corr} &= \frac{(\Delta C_{exp} - \Delta C_d^{bg})(p/b)_f^2 + (\Delta C_{exp} - \Delta C_f^{bg})(p/b)_d^2}{(p/b)_d(p/b)_f [(p/b)_d + (p/b)_f]}, \end{aligned} \quad (3)$$

where $(p/b)_d$ and $(p/b)_f$ are the peak to background ratios of the feeding and the decay peaks, respectively. Since the peak to background ratios of the $9/2_1^- \rightarrow 5/2_1^-$ and the $9/2_1^+ \rightarrow 11/2_1^-$ are larger no correction is needed for the background under these peaks. The correction to the measured centroid difference can be than simplified to:

$$\Delta C_{corr} = \frac{\Delta C_{exp} - \Delta C^{bg}}{p/b}, \quad (4)$$

where ΔC^{bg} and (p/b) refer the $11/2_1^- \rightarrow 9/2_1^-$ transition, which for the $9/2_1^-$ state is a feeding transition while for the $11/2_1^-$ state is a decay transition. In both cases the background correction is about 4 ps. After applying the corrections to the measured centroid differences, the lifetimes of the $9/2_1^-$ and the $11/2_1^-$ states were extracted by using Eq. (1) to be 26(6) ps and 97(6) ps, respectively.

The final results for the lifetimes are summarized in Table I, together with the resulting transition strengths. The present result for the lifetime of the $11/2_1^-$ state agrees well with

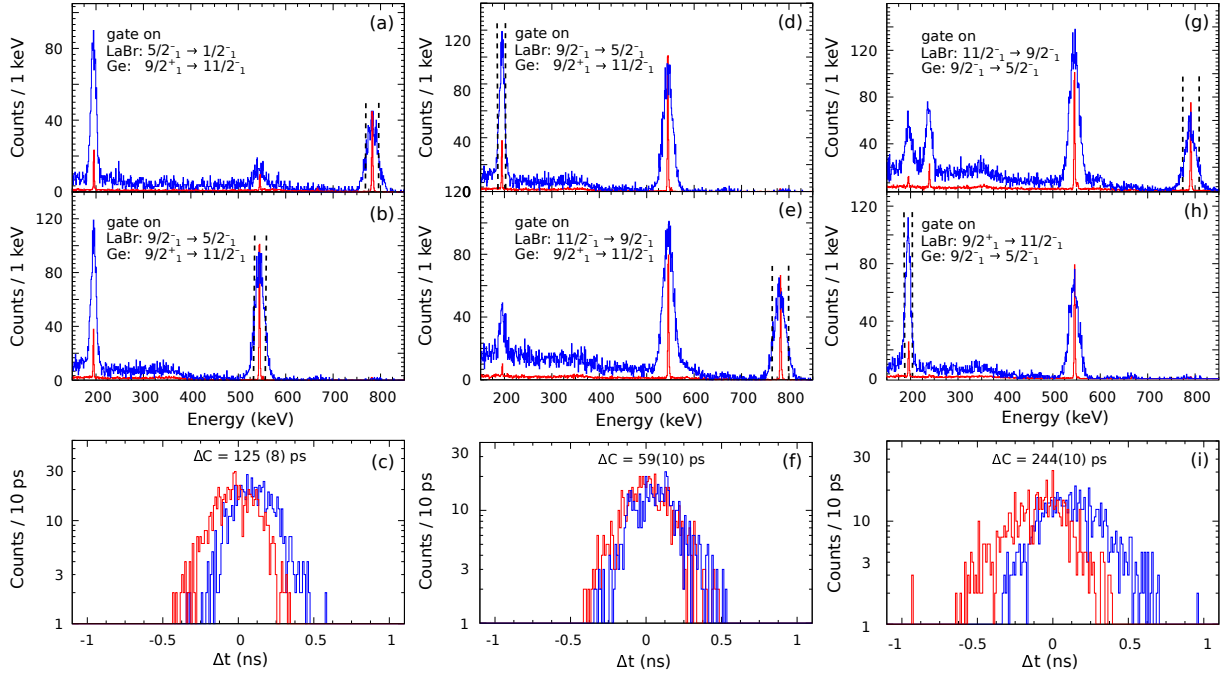


FIG. 3: (Color online) (a) LaBr (blue) and HPGe (red) detector projections in HPGe-LaBr gates, where the gate in the LaBr spectrum is set on the decay transition. The vertical dashed lines indicate the gates used to produce the time difference spectra displayed in (c). (b) same as (a) but the LaBr gate is set on the feeding transition. (c) Time-difference spectra for the 782-545 keV used to extract the lifetime of the $5/2_1^-$ state. (d,e,f) and (g,h,i) represent data taken as in (a,b,c) but used to extract the lifetimes of the $9/2_1^-$ and the $11/2_1^-$ states, respectively.

the previous measurement, while the result for the lifetime of the $5/2_1^-$ state is about 35% shorter than the adopted value [21]. It has to be noted that there is a certain ambiguity for the value of the multipole mixing ratio of the 195-keV ($11/2_1^- \rightarrow 9/2_1^-$) transition. The value adopted in Ref. [31] is based on α_K electron conversion coefficients [21, 22], while a smaller value results from a γ -ray angular distribution measurement from an oriented source [35]. A precise determination of multipole mixing ratios which are close to zero is a difficult task and measurements based on electron conversion coefficients are in general more reliable. However, in the particular case of 195-keV transition, it has to be noted that the α_L electron conversion coefficient reported in [22] also indicates that this transition is a pure $M1$. Therefore, we have included in Table I the transitions strengths extracted with both values of the multipole mixing ratio of 195-keV transition. As can be seen the multipole mixing ratio strongly affects the results for the $B(E2)$ strength of the 195-keV transition

TABLE I: Properties of the three investigated low-lying states of ^{209}Po and the γ -ray transitions originating from their decays.

E_{level} (keV)	J_i^π	J_f^π	E_γ (keV)	I_γ^a (%)	α^b	δ	$\tau_{(lit.)}^c$ (ps)	τ^d (ps)	Transition strength d,e $J_i^\pi \rightarrow J_f^\pi$
545	$5/2_1^-$						101(29)	66(5)	
		$1/2_1^-$	545	100	0.0262				$B(E2) = 251_{-18}^{+21}$
1327	$9/2_1^-$							26(6)	
		$5/2_1^-$	782	100(3)	0.0120				$B(E2) = 106_{-20}^{+32}$
		$5/2_2^-$	151	0.097(18)	1.319				$B(E2) = 378_{-96}^{+139}$
1522	$11/2_1^-$						101(29)	97(6)	
		$9/2_1^-$	195	100(5)	1.51(13)	$+0.40_{-0.22}^{+0.17f}$			$B(M1) = 0.019(3)$ $B(E2) = 1129_{-718}^{+893}$
					1.66(3)	0.077(55) ^g			$B(M1) = 0.021(2)$ $B(E2) = 46_{-39}^{+79}$
		$7/2_1^-$	113	0.78(16)	4.29				$B(E2) = 977_{-211}^{+226h}$ $B(E2) = 937_{-201}^{+213i}$
		$13/2_1^-$	104	10.1(16)	9.87				$B(M1) = 0.014(2)^h$ $B(M1) = 0.014(2)^i$

^aRelative γ -ray intensities. From Ref. [31] and references therein.

^bTheoretical total internal conversion coefficients. From Ref. [31] and references therein.

^cFrom Ref. [21].

^dFrom the present work.

^e $B(E2)$ values are given in e^2fm^4 ($1\text{W.u.} = 73.67 \text{ e}^2\text{fm}^4$), and $B(M1)$ values are given in μ_N^2 .

^fThe adopted multipole mixing ratios. From Ref. [31].

^gThe multipole mixing ratio from Ref. [35].

^hThe value is calculated in the case when the multipole mixing ratio and the total conversion coefficient of the 195-keV transition are adopted to be $+0.40_{-0.22}^{+0.17}$ and 1.51(13), respectively.

ⁱThe value is calculated in the case when the multipole mixing ratio and the total conversion coefficient of the 195-keV transition are adopted to be $+0.077(55)$ and 1.66(3), respectively.

while all other transition strengths, including the $B(M1)$ ones, remain virtually intact.

III. DISCUSSION

In order to check to what extent the new experimental data in Table I complies with the widely accepted view that the low-lying states of ^{209}Po arise from a weak coupling of a single neutron hole to the excited states of ^{210}Po [21], we have performed a realistic shell-model calculation. Moreover, the comparison between calculated and experimental data, especially the ones on the absolute transition strengths, also serves to test the reliability and the limits of the adopted Hamiltonian. The calculations have been performed using the code KSHELL [36], by assuming ^{208}Pb as a closed inert core, while the valence proton particles and neutron holes are let to occupy the orbitals $2p_{3/2}, 2p_{1/2}, 1f_{7/2}, 1f_{5/2}, 0h_{9/2}, 0i_{13/2}$ which are labeled with nlj , n starting from 0. The proton single-particle and neutron single-hole energies of the shell-model effective Hamiltonian have been taken from the experimental spectra of ^{209}Bi [31] and ^{207}Pb [37], and are reported in Table II.

TABLE II: Proton single-particle and neutron single-hole energies adopted in the calculation.

$\pi(nlj)$	ϵ (keV)	$\nu(nlj)^{-1}$	ϵ (keV)
$0h_{9/2}$	0	$2p_{1/2}$	0
$1f_{7/2}$	896	$1f_{5/2}$	570
$0i_{13/2}$	1608	$2p_{3/2}$	898
$1f_{5/2}$	2826	$0i_{13/2}$	1633
$2p_{3/2}$	3118	$1f_{7/2}$	2340
$2p_{1/2}$	3633	$0h_{9/2}$	3415

As regards the two-body effective interaction, the proton-proton, neutron-neutron, and proton-neutron matrix elements have been derived, respectively, in the particle-particle, hole-hole, and particle-hole formalism by mean of the \hat{Q} box folded-diagram approach [38, 39]. In particular, we have used the perturbative diagrammatic expansion of the \hat{Q} box by including one- and two-body diagrams up to second order in the interaction. The starting point of this procedure is the CD-Bonn nucleon-nucleon potential [40] renormalized by means of the $V_{\text{low-k}}$ approach [41] with a cutoff parameter $\Lambda = 2.2 \text{ fm}^{-1}$. The Coulomb potential is also taken into account for the proton-proton interaction.

It is worth mentioning that this Hamiltonian was already used in the past, even if with

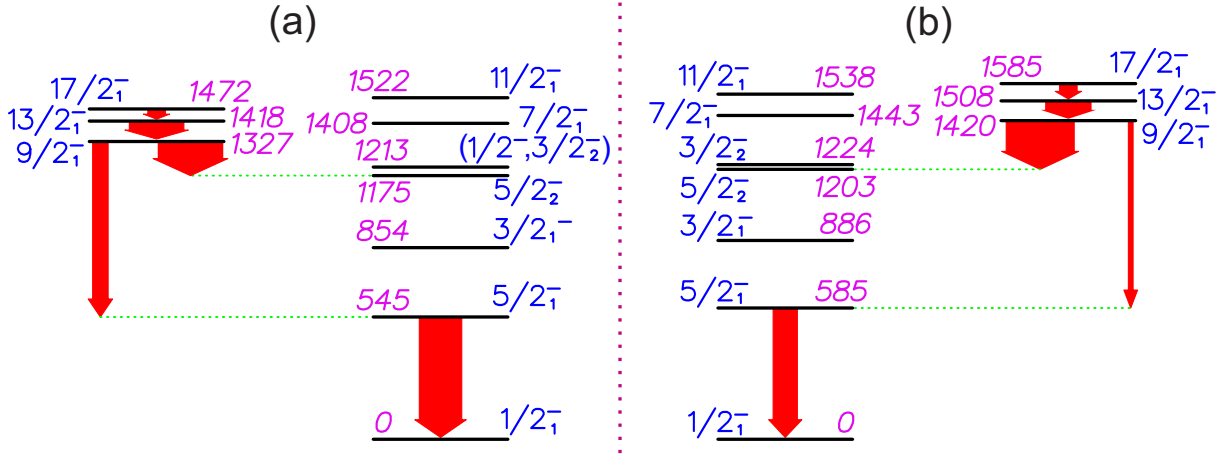


FIG. 4: (Color online) Comparison of experimental low-lying negative-parity excited states of ^{209}Po (a) with the calculated ones (b) (for details see the text). The experimental data is taken from Ref. [31]. The energies of the levels are given in keV. The arrows represent some of the transitions discussed the text. The widths of the arrows are proportional to the absolute $E2$ transition strengths.

a slightly smaller cutoff parameter ($\Lambda = 2.1\text{fm}^{-1}$), to study the particle-hole multiplets in ^{208}Bi [42]. It was shown that the three experimental multiplets $\pi 0h_{9/2}\nu 2p_{1/2}^{-1}$, $\pi 0h_{9/2}\nu 1f_{5/2}^{-1}$ and $\pi 0h_{9/2}\nu 0i_{13/2}^{-1}$ are well reproduced by theory with an accuracy within 100 keV.

Experimental and calculated spectra of ^{209}Po are shown in Fig. 4, where we have reported energy levels up to 1.6 MeV. The calculated excitation energies are in a very good agreement with the experimental data, discrepancies being less than 110 keV for almost all the states.

The calculated wave functions were used to compute the transition probabilities and moments that are compared with the experimental data in Table III. They have been calculated by employing the empirical effective charges $e_\pi = 1.5e$, $e_\nu = 0.92e$, whereas the adopted values for the effective gyromagnetic factors are $g_\pi^l = 1.2$, $g_\nu^l = -0.2$, $g_{\pi,\nu}^s = 0.7(g_{\pi,\nu}^s)_{bare}$. This choice of the effective charges and gyromagnetic factors leads to an overall good description of electromagnetic properties of ^{206}Pb , ^{207}Pb , ^{209}Bi and ^{210}Po , although we should mention that the predicted $B(E2; 2_1^+ \rightarrow 0_1^+)$ in ^{210}Po is ~ 6.5 times larger than the experimental value reported in Ref. [31] and twice the data reported in Ref. [18] in line with the results of Refs. [8, 9, 17, 43], and the magnetic dipole moments of the yrast $1/2_1^-$ and $5/2_1^-$ states in ^{207}Pb area about half of the measured ones.

It can be seen from Table III that the measured $B(M1; 11/2_1^- \rightarrow 13/2_1^-)$ is very well

TABLE III: Calculated and experimental reduced transition probabilities and moments in ^{209}Po . The $B(E2)$ values are given in $e^2\text{fm}^4$, the quadrupole moments are in efm^2 , the magnetic moments are in μ_N and $B(M1)$ in μ_N^2 .

Quantity	Calculated value	Experimental value ^a
$\mu(1/2_1^-)$	+0.31	+0.61(5)
$\mu(13/2_1^-)$	+6.05	+6.13(9)
$\mu(17/2_1^-)$	+7.84	+7.75(5)
$Q(13/2_1^-)$	-12.6	12.6(5)
$Q(17/2_1^-)$	-64.4	65.9(7)
$B(E2; 5/2_1^- \rightarrow 1/2_1^-)$	142	251_{-18}^{+21b}
$B(E2; 9/2_1^- \rightarrow 5/2_2^-)$	404	378_{-96}^{+139b}
$B(E2; 9/2_1^- \rightarrow 5/2_1^-)$	29	106_{-20}^{+32b}
$B(E2; 13/2_1^- \rightarrow 9/2_1^-)$	276	322(7)
$B(E2; 17/2_1^- \rightarrow 13/2_1^-)$	104	105(4)
$B(M1; 11/2_1^- \rightarrow 13/2_1^-)$	0.012	0.014(2) ^{b,c,d}
$B(E2; 11/2_1^- \rightarrow 7/2_1^-)$	262	$977_{-211}^{+226b,c}$ $937_{-201}^{+213b,c}$
$B(E2; 11/2_1^- \rightarrow 9/2_1^-)$	10	$1129_{-718}^{+893b,c}$ $46_{-39}^{+79b,d}$
$B(M1; 11/2_1^- \rightarrow 9/2_1^-)$	0.010	0.019(3) ^{b,c} 0.021(2) ^{b,d}

^aThe data is taken from Ref. [31] unless otherwise stated.

^bFrom the present work.

^cThe value is calculated in the case when the multipole mixing ratio and the total conversion coefficient of the 195-keV transition are adopted to be $+0.40_{-0.22}^{+0.17}$ and 1.51(13), respectively. (cf. Table I).

^dThe value is calculated in the case when the multipole mixing ratio and the total conversion coefficient of the 195-keV transition are adopted to be $+0.077(55)$ and 1.66(3), respectively. (cf. Table I).

reproduced. As regard the $B(M1; 11/2_1^- \rightarrow 9/2_1^-)$, the calculated value is in quite good agreement with the two very close experimental values corresponding to the two adopted multipole mixing ratios.

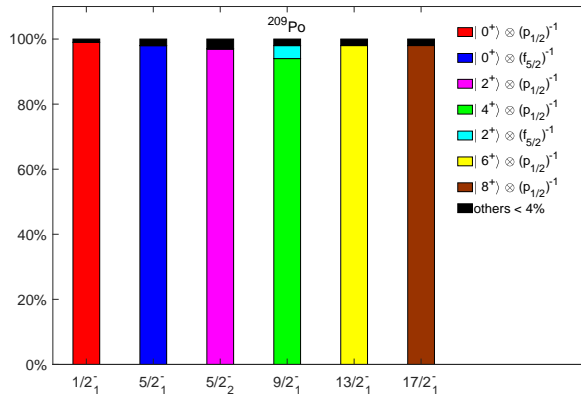


FIG. 5: Composition of selected states in ^{209}Po . See text for details.

On the other hand, the quality of the agreement between theory and experiment for the $B(E2)$'s strongly depends on the involved states. In fact, leaving out the $E2$ transitions from the $11/2_1^-$ state (we shall discuss these cases at the end of the section), the difference between theory and experiment for the other $B(E2)$ values ranges from 1 to about $100 e^2\text{fm}^4$. As regards the moments, a very good agreement is found for the $13/2_1^-$ and $17/2_1^-$ states, while the magnetic dipole moment of the $1/2_1^-$ state is underestimated by a factor ~ 2 .

To understand the reasons of these discrepancies we have analyzed the composition of the wave functions of ^{209}Po , by writing them in terms of a neutron hole coupled to the states of ^{210}Po . In Fig. 5, we report the components of such a development together with their probability amplitudes ($> 4\%$) for the $1/2_1^-$, $5/2_{1,2}^-$, $9/2_1^-$, $13/2_1^-$ and $17/2_1^-$ states. These amplitudes are strictly related to the one neutron pick-up spectroscopic factors from ^{210}Po , which are reported in Table IV for the sake of completeness.

All these states are characterized by a dominant component accounting for 94 – 99% of the calculated wave functions. In particular, the first $1/2^-$ and $5/2^-$ states are of single-hole nature resulting from the coupling of a $2p_{1/2}$ and $1f_{5/2}$ neutron hole, respectively, to the ground state of ^{210}Po . On the other hand, the other states arise mainly from $|\pi J^\pi \neq 0^+\rangle \otimes (\nu 2p_{1/2})^{-1}$ configurations, with $J^\pi = 2^+, 4^+, 6^+, 8^+$ for the $5/2_2^-$, $9/2_1^-$, $13/2_1^-$, $17/2_1^-$ states, respectively.

For each $E2$ transition involving these states, we have calculated the $|\langle J_f || E2 || J_i \rangle|$ matrix element by including only the dominant component of the initial and final wave functions. Their values are shown (in blue) in Fig. 6, where we have also reported the remaining contri-

TABLE IV: One neutron pick-up spectroscopic factors from ^{210}Po for selected states in ^{209}Po .

J_f^π	(nlj)	J_i^π	C^2S
$1/2_1^-$	$2p_{1/2}$	0_1^+	1.982
$5/2_1^-$	$1f_{5/2}$	0_1^+	5.863
$5/2_2^-$	$2p_{1/2}$	2_1^+	1.158
$9/2_1^-$	$2p_{1/2}$	4_1^+	1.048
	$1f_{5/2}$	2_1^+	0.085
$13/2_1^-$	$2p_{1/2}$	6_1^+	1.056
$17/2_1^-$	$2p_{1/2}$	8_1^+	1.034

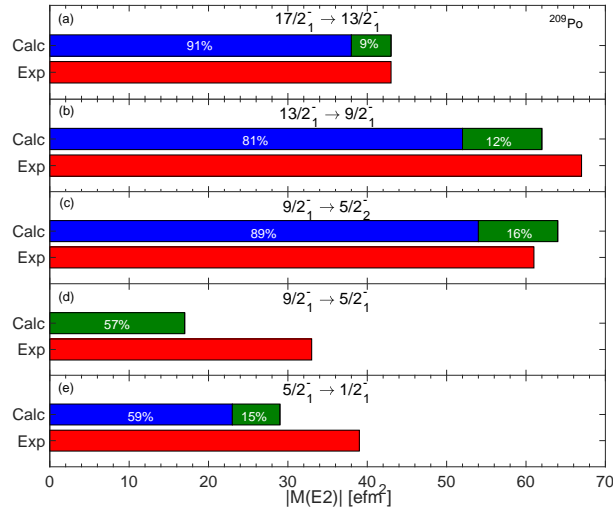


FIG. 6: Calculated and experimental $|\langle J_f || E2 || J_i \rangle|$ matrix elements. For each $E2$ transition, the blue bar represents the contribution from the dominant component of the initial and final wave function, while the green bar the remaining one. The percentages refer to experimental data.

Contributions (in green) due to the presence of minor components in the wave functions together with the experimental data (in red). The percentages of the two calculated contributions relative to the experimental values are also indicated.

A first observation is that the $B(E2; 17/2_1^- \rightarrow 13/2_1^-)$, $B(E2; 13/2_1^- \rightarrow 9/2_1^-)$, and $B(E2; 9/2_1^- \rightarrow 5/2_2^-)$ strengths, for which we obtain a good agreement, are mostly determined by the transitions between the dominant components of the involved states. It turns out that 91%, 81%, and the 89% of the experimental value of these three $B(E2)$'s is

covered, respectively, by the $|\pi 8^+\rangle \otimes (\nu p_{1/2})^{-1} \rightarrow |\pi 6^+\rangle \otimes (\nu p_{1/2})^{-1}$, $|\pi 6^+\rangle \otimes (\nu p_{1/2})^{-1} \rightarrow |\pi 4^+\rangle \otimes (\nu p_{1/2})^{-1}$, and $|\pi 4^+\rangle \otimes (\nu p_{1/2})^{-1} \rightarrow |\pi 2^+\rangle \otimes (\nu p_{1/2})^{-1}$ transition. Clearly, each of these three transitions only contributes through the proton term, namely through the corresponding transition in ^{210}Po .

For the other two $B(E2)$ strengths in ^{209}Po , *i.e.* $B(E2; 9/2_1^- \rightarrow 5/2_1^-)$, $B(E2; 5/2_1^- \rightarrow 1/2_1^-)$, the dominant components of the wave functions play a minor role. As a matter of fact, no contribution is given to the $B(E2; 9/2_1^- \rightarrow 5/2_1^-)$ by the transition $|\pi 4^+\rangle \otimes (\nu p_{1/2})^{-1} \rightarrow |\pi 0^+\rangle \otimes (\nu f_{5/2})^{-1}$, while the $|\pi 0^+\rangle \otimes (\nu f_{5/2})^{-1} \rightarrow |\pi 0^+\rangle \otimes (\nu p_{1/2})^{-1}$ transition accounts only for 57% of the experimental $B(E2; 5/2_1^- \rightarrow 1/2_1^-)$ value. On the other hand, the minor components of the $1/2_1^-$, $5/2_1^-$, $9/2_1^-$ wave functions do not give the required additional strength to reproduce the experimental $B(E2)$ values.

We have verified that a few percentage increase of components other the dominant one, as for instance the $|\pi 2^+\rangle \otimes (\nu f_{5/2})^{-1}$ component in the $1/2_1^-$ and $9/2_1^-$ states and the $|\pi 2^+\rangle \otimes (\nu p_{1/2})^{-1}$ component in the $5/2_1^-$ state, is able to lead to the correct $B(E2; 9/2_1^- \rightarrow 5/2_1^-)$, $B(E2; 5/2_1^- \rightarrow 1/2_1^-)$ values and, also to improve the agreement for the $B(E2; 9/2_1^- \rightarrow 5/2_2^-)$.

This is a clear signature that our calculations predict a too small percentage of components other than the dominant one. In other words, although these calculations give a quite reasonable account of the main features of the ^{209}Po wave functions, they are not able to produce the needed configuration mixing. This finding points to some uncertainty in the determinations of the off-diagonal matrix elements of the adopted proton-neutron effective interaction. Therefore, a fine tuning of the latter would be needed to improve the agreement with experiment.

It is worth noting, however, that the reduced fragmentation predicted by our calculations cannot account for the discrepancy we find between theory and experiment for the magnetic dipole moment of the $1/2_1^-$ state as well as for the two $E2$ transitions from the $11/2_1^-$ state. For the magnetic moment, the discrepancy is expected to arise also from the underestimation of the corresponding moment in ^{207}Pb , as mentioned above. The deficiencies in describing the magnetic moments of ground states of ^{209}Po and ^{207}Pb , as well as the overestimation of the $B(E2; 2_1^+ \rightarrow 0_1^+)$ in ^{210}Po , may be related to core-excited components of the ^{208}Pb core, which are outside the used model space and are not completely accounted for by the effective charges and effective g-factors. This is also the case when using the Kuo-Herling interaction [12] and has recently been discussed with respect to $B(E2; 2_1^+ \rightarrow 0_1^+)$ in ^{210}Po [43].

Our predicted value for the $B(E2; 11/2_1^- \rightarrow 7/2_1^-)$ differs from the possible experimental values (cf. Table III) by about $700 e^2\text{fm}^4$, which seems to indicate a more serious lack in our wave functions. The $11/2_1^-$ and $7/2_1^-$ states, as those reported in Fig. 5, are characterized by a single main component, namely $|\pi 6^+\rangle \otimes (\nu 2p_{1/2})^{-1}$ and $|\pi 4^+\rangle \otimes (\nu 2p_{1/2})^{-1}$, and a small increase in the weight of the minor components cannot provide the so large missing contributions. Moreover, the same big discrepancies between theoretical and experimental $B(E2)$'s from the $11/2_1^-$ state were found in Ref. [17], where shell-model calculations were performed for several nuclei of this region adopting a phenomenological Hamiltonian. On this basis, a re-measurement of this transition, which is affected by a large error, is certainly required. As for the $11/2_1^- \rightarrow 9/2_1^-$ transition, the ambiguity on the multipole mixing ratio gives rise to two very different values of the $B(E2)$ (cf. Table III). The very large $B(E2)$ value corresponding to $\delta = +0.40$ implies a more substantial change in our predicted wave functions than that discussed for the $11/2_1^- \rightarrow 7/2_1^-$ transition. The other δ value leads to a $B(E2)$ strength whose value is only $30 e^2\text{fm}^4$ larger than that predicted by theory and, consistently with the analysis made for the other transitions, can be explained by a small additional configuration mixing.

IV. SUMMARY

In the present study we have measured the lifetimes of the $11/2_1^-$, the $9/2_1^-$ and the $5/2_1^-$ states of ^{209}Po . The derived absolute $M1$ and $E2$ transition strengths together with the previously available experimental data on the low-lying negative-parity states of ^{209}Po have been compared to results of shell-model calculations with a realistic effective interaction derived from the CD-Bonn nucleon-nucleon potential within the framework of \hat{Q} box folded-diagram approach.

The experimental excitation energies of the low-lying negative states of ^{209}Po are very well reproduced by theory, while the agreement for the electromagnetic properties is less satisfactory. It turns out, in fact, that the quality of agreement, especially for the $B(E2)$'s, depends on the involved states. This may be seen as a clear indication of some deficiency inherent in the structure of our calculated wave functions. We predict that the low-lying negative-parity states of ^{209}Po are dominated by the coupling of a neutron hole to the yrast states of ^{210}Po , which implies that the removal of one neutron from the ^{210}Po does not

induce any additional quadrupole collectivity. A detailed analysis of the $B(E2)$ transitions confirms this finding, although it also suggests that we underestimate the weight of the minor components of the wave functions. We have verified that a few percentage increase of these components is required to obtain a quantitative description of all transition strengths. The presence of such a small but apparently essential configuration mixing clearly evidences the role of the proton-neutron part of the effective interaction and the need of a fine tuning of its matrix elements.

Acknowledgments

We thank H. Naïdja and S. Dimitrova for the fruitful discussions. G. De Gregorio and A. Gargano acknowledge the CINECA award under the ISCRA initiative and through the INFN-CINECA agreement for the availability of high performance computing resources and support. G. De Gregorio acknowledges also the support by the funding program "VALERE" of Università degli Studi della Campania "Luigi Vanvitelli". This work was supported by the DAAD partnership agreement between the University of Cologne and University of Sofia, and by the Bulgarian National Science Fund under Grant No. DN08/23/2016.

-
- [1] M.G. Mayer, Phys. Rev. **75**, 1969 (1949).
 - [2] O. Haxel, J. H. D. Jensen, H. E. Suess, Phys. Rev. **75**, 1766 (1949).
 - [3] R. F. Casten, Phys. Lett. 152B, 145 (1985).
 - [4] A. de Shalit and I. Talmi, Nuclear Shell Theory (Academic Press, New York, 1963).
 - [5] J. B. Mcgrory and T. T. S. Kuo, Nucl. Phys. A **247**, 283 (1975).
 - [6] C.W.Ma and W. W. True, Phys. Rev. C **8**, 2313 (1973).
 - [7] D.Zwarts and P.W.M. Glaudemans, Z. Phys.A **320**, 487 (1985).
 - [8] T. R. McGoram, G. D. Dracoulis, A. P. Byrne, A. R. Poletti, and S. Bayer, Nucl. Phys. A **637**, 469 (1998).
 - [9] L. Coraggio, A. Covello, A. Gargano, N. Itaco, and T. T. S. Kuo, Phys. Rev. C **58**, 3346 (1998).
 - [10] L. Coraggio, A. Covello, A. Gargano, N. Itaco, and T. T. S. Kuo, Phys. Rev. C **60**, 064306

- (1999).
- [11] E. Caurier, M. Rejmund, and H.Grawe, Phys. Rev. C **67**, 054310 (2003).
 - [12] E. K. Warburton and B. A. Brown, Phys. Rev. C **43**, 602 (1991).
 - [13] B. Silvestre and J. P. Boisson, Phys. Rev. C **24**, 717 (1981);
 - [14] L. Rydstrom, J. Blomqvist, R. J. Liotta, and C. Pomar, Nucl. Phys. A **512**, 217 (1990).
 - [15] A. Zemel and J. Dobes, Nucl. Phys. A **27**, 2311 (1983).
 - [16] Z.Y. Xu, Y. Lei, Y.M. Zhao, S.W. Xu, Y.X. Xie, and A. Arima, Phys. Rev. C **79**, 054315 (2009).
 - [17] E. Teruya, K. Higashiyama, and N. Yoshinaga. Phys. Rev. C **93** 064327 (2016) *and references therein*.
 - [18] D. Kocheva, G. Rainovski, J. Jolie, N. Pietralla, A. Blazhev, A. Astier, Th. Braunroth, M.L. Cortés, A. Dewald, M. Djongolov, C. Fransen, K. Gladnishki, A. Hennig, V. Karayonchev, J.M. Keatings, J. Litzinger, C. Müller-Gatermann, P. Petkov, M. Scheck, P. Spagnoletti, Ph. Scholz, C. Stahl, R. Stegmann, M. Stoyanova, P. Thöle, N. Warr, V. Werner, W. Witt, D.Wölk, K.O. Zell, P. Van Isacker, V. Yu. Ponomarev, Eur. Phys. J. A **53**, 175 (2017).
 - [19] M. Stoyanova, G. Rainovski, J. Jolie, N. Pietralla, A. Blazhev, M. Beckers, A. Dewald, M. Djongolov, A. Esmaylzadeh, C. Fransen, L.M. Gerhard, K.A. Gladnishki, S. Herb, P.R. John, V. Karayonchev, J.M. Keatings, R. Kern, L. Knafla, D. Kocheva, L. Kornweibel, Th. Kröll, M. Ley, K.M. Mashtakov, C. Müller-Gatermann, J.-M. Régis, M. Scheck, K. Schomacker, J. Sinclair, P. Spagnoletti, C. Sürder, N. Warr, V. Werner and J. Wiederhold, Phys. Rev. C **100**, 064304 (2019).
 - [20] T.J. Gray, J.M. Allmond, A.E. Stuchbery, C.-H. Yu, C. Baktash, A. Gargano, A. Galindo-Uribarri, D.C. Radford, J.C. Batchelder, J.R. Beene, C.R. Bingham, L. Coraggio, A. Covello, M. Danchev, C.J. Gross, P.A. Hausladen, N. Itaco, W. Krolas, J.F. Liang, E. Padilla-Rodal, J. Pavan, D.W. Stracener, R.L. Varner, Phys. Rev. Lett. **124**, 032502 (2020).
 - [21] M. Alpsten, Å. Appelqvist, G. Astner, Phys. Scr. **4**, 137 (1971).
 - [22] L.J. Jardine, S.G. Prussin, J.M. Hollander, Nucl. Phys. A **233**, 25 (1974).
 - [23] T. Yamazaki and E. Matthias, Phys. Rev. **175**, 1476 (1968).
 - [24] O. Häusser, T.K. Alexander, J.R. Beene, E.D. Earle, A.B. McDonald, F.C. Khanna, I.S. Towner, Nucl. Phys. A **273**, 253 (1976).
 - [25] W. Baldrige, N. Freed, J. Gibbons, Phys. Lett B **36**, 179 (1971).

- [26] G. Nicolescu, E. A. Ivanov, and D. Plostinaru, *Phys. Rev. C* **79**, 044314 (2009).
- [27] J.-M. Régis, G. Pascovici, J. Jolie, M. Rudigier, *Nucl. Instr. Meth. Phys. Res. A* **622**, 83 (2010).
- [28] A. Iltis, M.R. Mayhugh, P. Menge, C.M. Rozsa, O. Selles, V. Solovyev, *Nucl. Instr. Meth. Phys. Res. A* **563**, 359 (2006).
- [29] J.-M. Régis, N. Saed-Samii, M. Rudigier, S. Ansari, M. Dannhoff, A. Esmaylzadeh, C. Fransen, R.-B. Gerst, J. Jolie, V. Karayonchev, C. Müller-Gatermann and S. Stegemann, *Nucl. Instr. Meth. Phys. Res. A* **823**, 72 (2016).
- [30] Pragati, A.Y. Deo, Zs. Podolyák, P.M. Walker, A. Algora, B. Rubio, J. Agramunt, L.M. Fraile, N. Al-Dahan, N. Alkhomashi, J.A. Briz, M.E. Estevez Aguado, G. Farrelly, W. Gelletly, A. Herlert, U. Köster, and A. Maira, *Phys. Rev. C* **94**, 064316 (2016).
- [31] J. Chen, F.G. Kondev, *Nuclear Data Sheets* **126**, 373 (2015).
- [32] J.-M. Régis, H. Mach, G.S. Simpson, J. Jolie, G. Pascovici, N. Saed-Samii, N. Warr, A. Bruce, J. Degenkolb, L.M. Fraile, C. Fransen, D.G. Ghita, S. Kisiov, U. Koester, A. Korgul, S. Lalkovski, N. Mărginean, P. Mutti, B. Olaizola, Z. Podolyak, P.H. Regan, O.J. Roberts, M. Rudigier, L. Stroe, W. Urban and D. Wilmsen, *Nucl. Instr. Meth. Phys. Res. A* **726**, 191 (2013).
- [33] J.-M. Régis, M. Rudigier, J. Jolie, A. Blazhev, C. Fransen, G. Pascovici and N. Warr, *Nucl. Instr. Meth. Phys. Res. A* **684**, 36 (2012).
- [34] J.-M. Régis, A. Esmaylzadeh, J. Jolie, V. Karayonchev, L. Knafla, U. Köster, Y.H. Kim, E. Strub, *Nucl. Instr. Meth. Phys. Res. Sect. A* **955**, 163258 (2020).
- [35] P. Šimeček, I. Procházka, Chan Kim Kchung, M. Finger, M. I. Fominykh, B. A. Gvozdev, A. P. Kabachenko, T. Lešner, P. Malinský, V. N. Pavlov, M. Vobecký, *Hyperfine Interact* **34**, 131 (1987).
- [36] N. Shimizu, T. Mizusaki, T. Utsuno, and Y. Tsunoda. *Comput. Phys. Commun.* **244**, 372 (2019).
- [37] F.G. Kondev, S. Lalkovski *Nuclear Data Sheets* **112**, 707 (2011).
- [38] L. Coraggio, A. Covello, A. Gargano, N. Itaco and T.T.S.Kuo. *Prog. Part. Nucl. Phys.* **62**, 135 (2009).
- [39] L. Coraggio, A. Covello, A. Gargano et al. *Ann. Phys.* **327**, 2125 (2012).
- [40] R. Machleidt, *Phys. Rev. C* **63**, 024001 (2001).
- [41] S. Bogner, T. T. S. Kuo, and L. Coraggio, *Nucl. Phys. A* **684**, 432c (2001).

- [42] A. Covello, L. Coraggio, A. Gargano, and N. Itaco. *Physics of Atomic Nuclei*, **67**, (2004).
- [43] V. Karayonchev, A. Blazhev, A. Esmaylzadeh, J. Jolie, M. Dannhoff, F. Diel, F. Dunkel, C. Fransen, L. M. Gerhard, R.-B. Gerst, L. Knafla, L. Kornwebel, C. Müller-Gatermann, J.-M. Régis, N. Warr, K.O. Zell, M. Stoyanova, P. Van Isacker, *Phys. Rev. C* **99**, 024326 (2019).

Publication II:

5 Lifetimes of the 4_1^+ states of ^{206}Po and ^{204}Po : A study of the transition from noncollective seniority-like mode to collectivity

Lifetimes of the 4_1^+ states of ^{206}Po and ^{204}Po : A study of the transition from noncollective seniority-like mode to collectivity

M. Stoyanova,¹ G. Rainovski,^{1,*} J. Jolie,² N. Pietralla,³ A. Blazhev,² M. Beckers,² A. Dewald,² M. Djongolov,¹ A. Esmaylzadeh,² C. Fransen,² L. M. Gerhard,² K. A. Gladnishki,¹ S. Herb,² P. R. John,³ V. Karayonchev,² J. M. Keatings,⁴ R. Kern,³ L. Knafle,² D. Kocheva,¹ L. Kornweibel,² Th. Kröll,³ M. Ley,² K. M. Mashtakov,⁴ C. Müller-Gatermann,² J.-M. Régis,² M. Scheck,⁴ K. Schomacker,² J. Sinclair,⁴ P. Spagnoletti,⁴ C. Sürder,³ N. Warr,² V. Werner,³ and J. Wiederhold³

¹Faculty of Physics, St. Kliment Ohridski University of Sofia, 1164 Sofia, Bulgaria

²Institut für Kernphysik, Universität zu Köln, 50937 Köln, Germany

³Institut für Kernphysik, Technische Universität Darmstadt, 64289 Darmstadt, Germany

⁴School of Computing, Engineering, and Physical Sciences, University of the West of Scotland, Paisley PA1 2BE, United Kingdom



(Received 7 October 2019; published 6 December 2019)

Low-lying yrast states of ^{204}Po and ^{206}Po were investigated by the γ - γ fast timing technique with $\text{LaBr}_3(\text{Ce})$ detectors. Excited states of these nuclei were populated in the $^{197}\text{Au}(^{11}\text{B}, 4n)^{204}\text{Po}$ and the $^{198}\text{Pt}(^{12}\text{C}, 4n)^{206}\text{Po}$ fusion-evaporation reactions, respectively. The beams were delivered by the FN-Tandem accelerator at the University of Cologne. The lifetimes of the 4_1^+ states of both nuclei were measured, along with an upper lifetime limit for the 2_1^+ state of ^{204}Po . A comparison between the derived $B(E2; 4_1^+ \rightarrow 2_1^+)$ values and results from simplified empirical two-state mixing calculations suggests that for the 4_1^+ states of even-even polonium isotopes the transition from single-particle mode at $N = 126$ to collective mode, when reducing the number of neutrons, occurs above $N = 122$.

DOI: [10.1103/PhysRevC.100.064304](https://doi.org/10.1103/PhysRevC.100.064304)

I. INTRODUCTION

The nuclear shell model represents the most fundamental concept in nuclear structure physics that naturally leads to the appearance of magic numbers due to the existence of large energy gaps, primarily defined by the shape of the potential and the spin-orbit interaction [1]. The shell model, in combination with pairing correlations, provides an easy way to understand low-energy spectra of semimagic nuclei. Low-energy excited states with $J > 0$ in semimagic nuclei, with more than one particle in a single high- j orbital, are formed by recoupling of angular momenta of unpaired nucleons, thus forming multiplets of states that have the same number of unpaired nucleons. This number is called seniority (ν) [2–4] and is generally considered as a good quantum number. In fact, the generalized seniority scheme [3,4] represents a truncation of the nuclear shell model. For the yrast states of even-even nuclei the seniority scheme is manifested by a few clear experimental signatures [5,6]: the excited yrast states have seniority $\nu = 2$ and follow an energy pattern that is equivalent to the one for a j^2 configuration in which the energy spacing between the states decreases towards the state with maximum angular momentum; the absolute $E2$ transition strength for the seniority-changing transition $2_1^+(\nu = 2) \rightarrow 0_1^+(\nu = 0)$ increases in a parabolic way with the filling of the j shell and reaches a maximum at the middle of the j shell; and the absolute $E2$ transition strengths for the seniority-conserving transitions

$J \rightarrow J - 2 (J > 4)$ decrease in a parabolic way with the filling of the j orbital and reaches a minimum at the middle of the j orbital. It can be expected that the features of the seniority scheme persist in open-shell nuclei close to magic numbers in which low-energy excitations are dominated by nucleons of the same kind. However, when the number of the other kind of valence nucleons increases, it can also be expected that the proton-neutron interaction increases [7] and eventually a collective behavior emerges. In fact, this can be deemed as a transition from single-particle (seniority-type) excitations to collective ones. When and how this transition appears, i.e., to what extent the seniority features persist in open shell nuclei, is not entirely clear. A recent similar study for the $N = 50$ isotopes has shown that the breaking down of the seniority symmetry is caused by cross-shell core excitations [8].

The open-shell Po-Rn-Ra nuclei in the vicinity of the double-magic nucleus ^{208}Pb offer a suitable ground for studying the transition from single-particle seniority type excitations to collective mode. It can be expected, as suggested in Ref. [5], that the valence neutrons in $N \leq 126$ nuclei occupy orbitals with high principal quantum number and low angular momentum. As a result, they interact weakly with the protons in the $h_{9/2}$ orbital [9], which dominate the wave functions of the yrast states forming a seniority-like structure. Indeed, for all even-even nuclei in the Po-Rn-Ra isotonic chains with $122 \leq N \leq 126$ the yrast states follow a typical seniority-like pattern. The 8_1^+ states in these nuclei are isomers with wave functions dominated by the $\pi(h_{9/2})^n$ configuration [10]. The latter assignment is in agreement with the almost constant values of the measured magnetic moments of these

*rig@phys.uni-sofia.bg

states [11]. Moreover, the $B(E2; 8_1^+ \rightarrow 6_1^+)$ values decrease with the increase of proton number for all even-even nuclei in the Po-Rn-Ra isotonic chains with $120 \leq N \leq 126$ [5]. Based on these arguments Ressler *et al.* [5] suggested that the noncollective seniority regime persists for nuclei from the Po-Rn-Ra isotonic chains with $122 \leq N \leq 126$ up to ^{210}Ra [10], and a collective behavior emerges around $N = 118$ –120.

However, it has to be noted that due to lack of experimental data, the interpretation in Ref. [5] does not include the evolution of the absolute $E2$ transition strengths for the seniority-changing transitions $2_1^+(\nu = 2) \rightarrow 0_1^+(\nu = 0)$. Recently $B(E2; 2_1^+ \rightarrow 0_1^+)$ values of 18_{-10}^{+14} W.u. and 13(6) W.u. have been reported for the $N = 122$ isotones ^{206}Po and ^{208}Rn , respectively [12]. These values suggest a constant, or slightly increasing trend with respect to the $B(E2; 2_1^+ \rightarrow 0_1^+)$ value in ^{204}Pb , instead of the expected more rapid increase, should the seniority regime persist. Based on this observation and QRPA calculations [12], it has been suggested that, at least for the 2_1^+ states of the polonium isotopes, a moderate collectivity sets in immediately when moving away from the closed proton shell [12]. Thus, the energy level pattern and the evolution of the $B(E2; 8_1^+ \rightarrow 6_1^+)$ values suggest that the noncollective seniority regime persists for the $N = 122$ isotones, as suggested in Refs. [5,10], while the newly measured values of the $B(E2; 2_1^+ \rightarrow 0_1^+)$ in ^{206}Po and ^{208}Rn indicate a moderate collectivity [12]. This suggests that the transition from single-particle seniority-type mode to collective mode develops differently for low- and high-spin states. In order to shed more light on this process we have measured the lifetimes of the 4_1^+ states of ^{206}Po and ^{204}Po which determine the $E2$ transition strengths for the seniority-preserving transition $4_1^+(\nu = 2) \rightarrow 2_1^+(\nu = 2)$. Until now, these data were missing due to experimental difficulties that stem from the fact that the 4_1^+ states of these nuclei are positioned between the long-lived 8_1^+ states [$\tau(8_1^+; ^{206}\text{Po}) = 335(6)$ ns [13] and $\tau(8_1^+; ^{204}\text{Po}) = 202(7)$ ns [14]] and the short-lived 2_1^+ states [$\tau(2_1^+; ^{206}\text{Po}) = 3.7_{-1.7}^{+2.8}$ ps [12]].

II. EXPERIMENT

The experiments were performed at the HORUS spectrometer [15] of the FN Tandem facility at the University of Cologne. The excited states of ^{206}Po were populated in the $^{198}\text{Pt}(^{12}\text{C}, 4n)$ fusion-evaporation reaction at a beam energy of 65 MeV. The target used was a ^{198}Pt foil with a thickness of 10 mg/cm² enriched to 91.6%. The excited states of ^{204}Po were populated in the $^{197}\text{Au}(^{11}\text{B}, 4n)$ fusion-evaporation reaction at a beam energy of 55 MeV. A 110-mg/cm²-thick ^{197}Au foil was used as a target. The γ rays from the decay of the excited states were detected by a hybrid array consisting of eight HPGe detectors and nine LaBr₃(Ce) scintillators (hereafter called LaBr), each with dimensions $\phi 1.5 \times 1.5$ in. To suppress the Compton background, six of the LaBr detectors were placed inside bismuth-germanate (BGO) anti-Compton shields. The other three LaBr had lead shields to suppress background events associated with scattered γ rays. The time differences between the timing signals for every unique combination of LaBr detectors were measured using time-

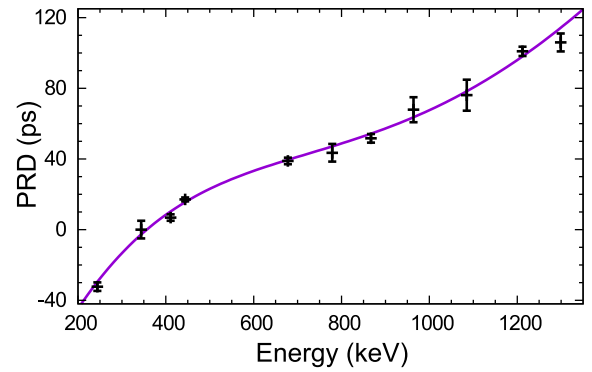


FIG. 1. The PRD curve of the setup measured with a ^{152}Eu source.

to-amplitude converters (TAC) applying the multiplexed-start and multiplexed-stop electronics setup [16]. The detector energy signals and the TAC amplitudes were recorded using 80-MHz synchronized digitizers in a triggerless mode.

The lifetimes of the states of interest were extracted from the time difference spectra by applying the generalized centroid difference (GCD) method. The method is discussed in detail in Ref. [17]. Some aspects of the present analyses along with preliminary results are also presented in Ref. [18]. Here we briefly present the method and the final results from the analyses. In the GCD method, two independent time spectra are obtained, constructed as the time difference between two signals generated by two consecutive γ rays that populate and depopulate an excited state of interest. When a transition which feeds the state (E_f) provides the start signal to the TAC and a decay transition (E_d) from this state provides the stop signal, a time difference distribution labeled as ‘‘Delayed’’ (D) is obtained. In the reverse case, a time difference distribution labeled as ‘‘Antidelayed’’ (AD) is obtained. Both distributions are characterized by their centroids, C^D and C^{AD} , respectively. Assuming no background contributions, the mean lifetime of the state of interest τ can be expressed via the difference between the centroids of the time spectra:

$$\Delta C(E_f, E_d) \equiv C^D - C^{AD} = 2\tau + \text{PRD}(E_f, E_d). \quad (1)$$

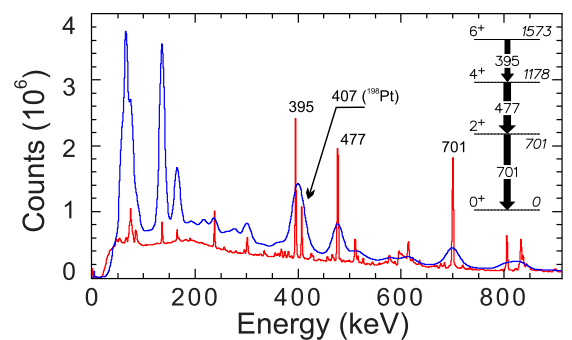


FIG. 2. Full projections of the HPGe-LaBr-LaBr (blue) and HPGe-LaBr-HPGe (red) coincidence data from the $^{198}\text{Pt}(^{12}\text{C}, 4n)$ reaction at a beam energy of 65 MeV. The inset shows a partial level scheme of ^{206}Po . The peaks from the transitions used in the analyses are labeled by their energies.

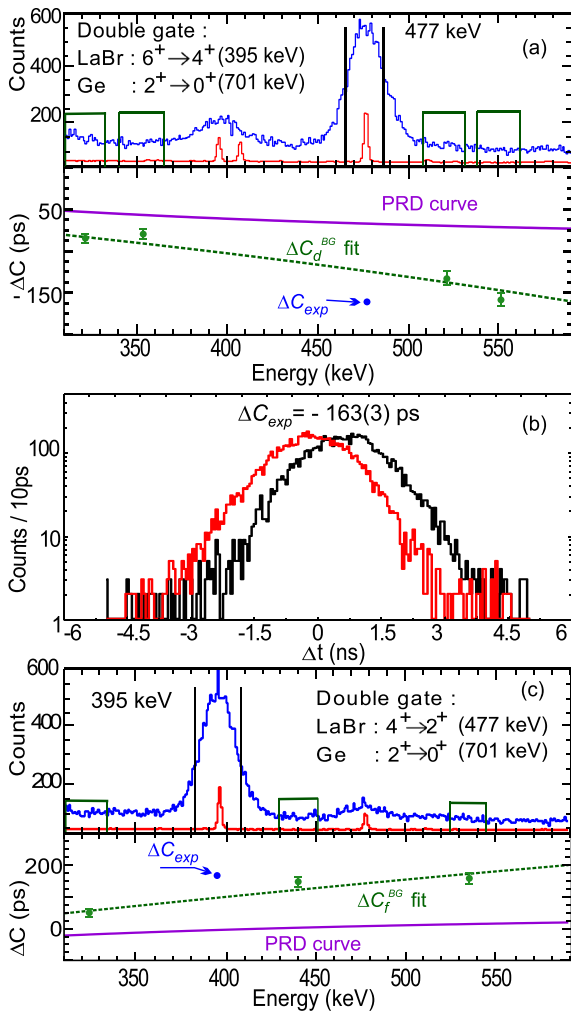


FIG. 3. The procedure for extracting the lifetime of the 4_1^+ state in ^{206}Po . (a) Double-gated spectra from LaBr (blue) detectors and HPGe detectors (red) produced from triple coincidence data by imposing the indicated coincidence conditions (gates). Here the gate on the LaBr detectors is set on the transition feeding the level of interest. The vertical black lines indicate the gate width used to produce the time-difference spectra at the full energy peak (FEP) of the decay transition. The corresponding peak-to-background ratio is 4.38. The vertical green lines indicate the gates used to extract the time response of the background. The panel below presents the fitted time response of the background (dashed green line), together with the PRD curve (magenta line) and the obtained centroid difference (the blue circle). The uncertainty of the latter is within the size of the circle. (b) LaBr delayed and antidelated time-difference spectra for the 395- and 477-keV feeder-decay combination with additional HPGe gate on the 701-keV transition. (c) Same as (a) but the gate on the LaBr detectors is set on the decay transition. The corresponding peak-to-background ratio is 4.41. All presented spectra are not background subtracted.

In this formula, PRD stands for prompt response difference and describes the mean time-walk characteristics of the setup [19]. For the calibration of the PRD, a ^{152}Eu source was used. Two time spectra were produced by selecting feeder-decay combinations for states with well known lifetimes.

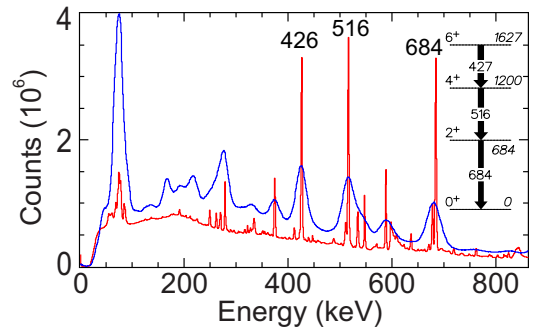


FIG. 4. Full projections of the HPGe-LaBr-LaBr (blue) and HPGe-LaBr-HPGe (red) coincidence data from the $^{197}\text{Au}(^{11}\text{B}, 4n)$ reaction at a beam energy of 55 MeV. The inset shows a partial level scheme of ^{204}Po . The peaks from the transitions used in the analyses are labeled by their energies.

Measuring the centroid differences ΔC and using Eq. (1), the PRD is obtained. The data points are fitted using the function [19,20]

$$\text{PRD}(E_\gamma) = \frac{a}{\sqrt{eE_\gamma^2 + b}} + cE_\gamma + d. \quad (2)$$

The final result of the PRD curve is presented in Fig. 1. The precision of the PRD fit is defined as two times the standard root-mean-squared deviation (2σ), corresponding in our case to 8 ps. More details on constructing the PRD curve for the present setup can be found in Ref. [18].

The lifetimes of interest were extracted by analyzing triple- γ coincidences. The full projections of the triple coincidences together with a level scheme of the yrast states of ^{206}Po relevant for the analysis are shown in Fig. 2. The triple- γ coincidences allow the lifetimes to be extracted from γ - γ data in LaBr detectors which are in an additional coincidence with a certain energy registered in the HPGe detectors. The latter coincidence condition improves the peak-to-background ratio in the LaBr detectors, reduces the influence of the possible contaminant transitions with energies similar to those of the feeder and/or decay transitions, and reduces the influence of the time-correlated background. The doubly gated LaBr and HPGe spectra, relevant for extracting the lifetime of the 4_1^+ state of ^{206}Po , are shown in Figs. 3(a) and 3(c). These spectra are generated from HPGe-LaBr-LaBr and HPGe-LaBr-HPGe triple coincidences data, respectively, by using the same gates in both cases. By comparing the spectra in Fig. 2 and in Figs. 3(a) and 3(c) some advantages of the triple- γ coincidences can clearly be seen. For example, the 407-keV peak which corresponds to the $2_1^+ \rightarrow 0_1^+$ transition in ^{198}Pt is clearly present in Fig. 2 and apparently cannot be resolved from the 395-keV peak in the LaBr spectra. However, once proper HPGe gates are applied, the contribution of the 407-keV peak is significantly reduced while the second LaBr gate completely eliminates it [cf. Figs. 3(a) and 3(c)].

The delayed and the antidelated time distributions, shown in Fig. 3(b), are obtained by setting the first LaBr gate on the full-energy peak (FEP) of the 395-keV transition and

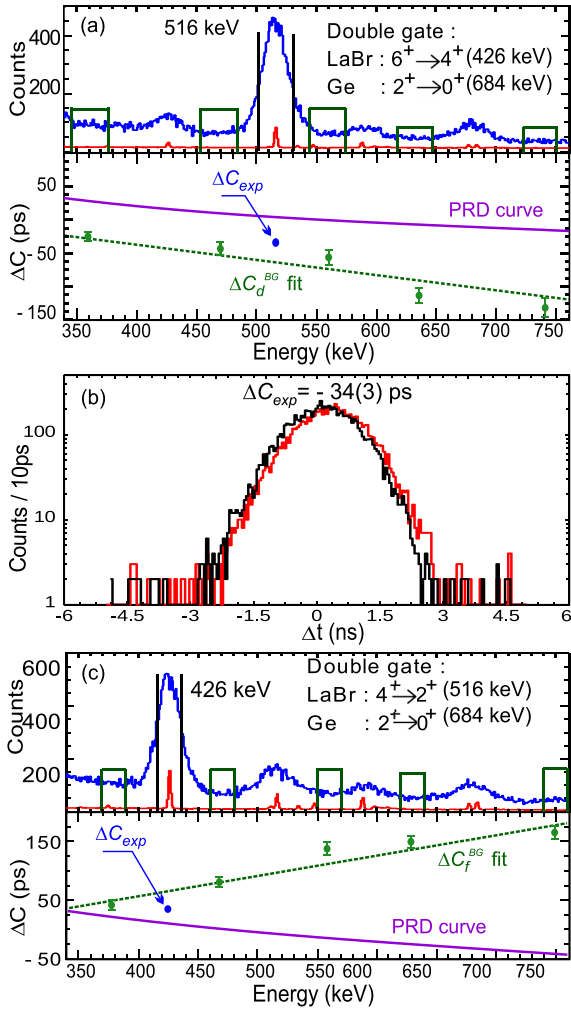


FIG. 5. The procedure of extracting the lifetime of the 4_1^+ state in ^{204}Po . The figure is analogous to Fig. 3. The corresponding peak-to-background ratios are 7.06 and 5.34.

the second LaBr gate on the FEP of the 477-keV transition. The reverse combination of gates, demonstrated in Fig. 3(c), produces the same time distributions but with exchanged “D” and “AD” labels. By measuring the difference between the centroids of these time distributions ΔC_{exp} , the lifetime can be determined. However, this value cannot be directly used in Eq. (1) since it contains contributions from the time-correlated Compton background which comes from the counts underneath the full energy peaks (FEPs). A correction for these contributions can be done by sampling the time response of

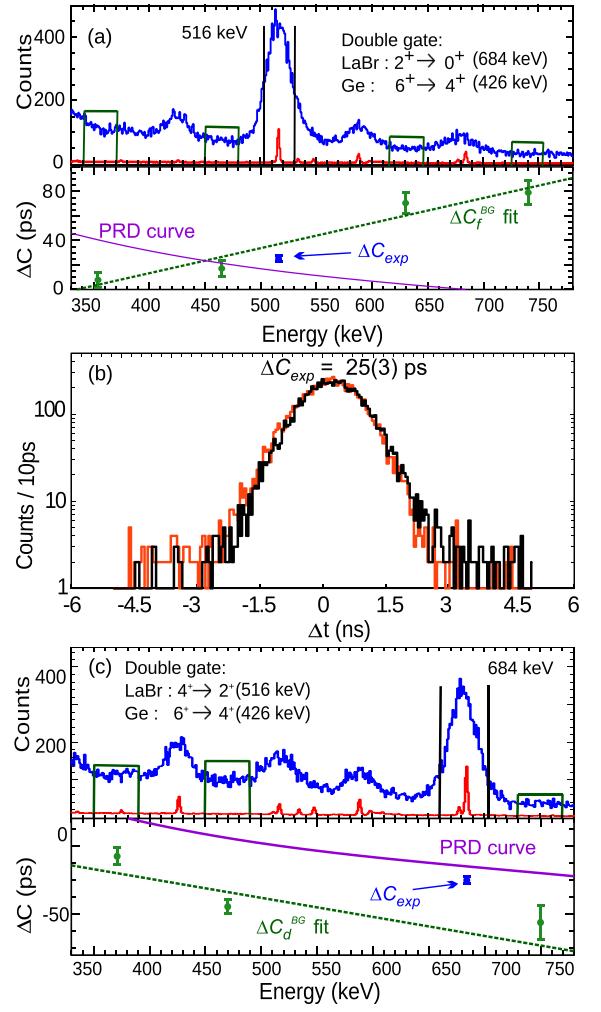


FIG. 6. The procedure of extracting the lifetime of the 2_1^+ states of ^{204}Po . The figure is analogous to Fig. 3. The corresponding peak-to-background ratios are 3.9(1) and 3.8(1).

the background at several positions on either side of the FEP of the decay transition [21], as depicted in Fig. 3(a). The obtained data points are fitted with a quadratic function and the time response of the background at the position of the FEP of the decay ΔC_d^{BG} is determined by interpolation. The data points used to fit the time response of the background are presented on the lower panel of Fig. 3(a). An analogous procedure is performed to obtain the time response of the background ΔC_f^{BG} at the position of the FEP of the feeder as shown in Fig. 3(c). Finally, the centroid difference ΔC which

TABLE I. Lifetimes determined from the fast-timing experiments on ^{204}Po and ^{206}Po and energies of the corresponding coincidence conditions used to obtain time-difference spectra as well as resulting $E2$ reduced transition strengths.

Nucleus	State	E_f (keV)	E_d (keV)	HPGe gate (keV)	α^a	τ (ps)	$B(E2)(e^2 \text{fm}^4)$
^{206}Po	4_1^+	395	477	701	0.0359	89(7)	359(28)
^{204}Po	4_1^+	426	516	684	0.0297	23(6)	939_{-195}^{+326}
	2_1^+	516	684	426	0.01584	≤ 9	≥ 596

^aTotal electron conversion coefficients for the $E2$ decay transitions. From Ref. [22].

can directly be used in Eq. (1) is calculated as suggested in Ref. [21]:

$$\Delta C = \Delta C_{\text{exp}} + \frac{1}{2} \left(\frac{\Delta C_{\text{exp}} - \Delta C_f^{\text{BG}}}{(p/b)_f} + \frac{\Delta C_{\text{exp}} - \Delta C_d^{\text{BG}}}{(p/b)_d} \right), \quad (3)$$

where $(p/b)_{f,d}$ are the peak-to-background ratios observed in the gates indicated in Fig. 3. As a result of this procedure we have measured the lifetime of the 4_1^+ state of ^{206}Po to be $\tau(4_1^+; ^{206}\text{Po}) = 89(7)$ ps.

The same analysis is used to determine the lifetime of the 4_1^+ state of ^{204}Po . The full projections of the triple coincidences, together with a level scheme of the yrast states of ^{204}Po relevant for the analysis, are shown in Fig. 4. In Fig. 5 the procedure of extracting the lifetime is presented. As in the case of ^{206}Po , here the comparison between the spectra in Figs. 4, 5(a), and 5(c) again reveals the advantages of the triple- γ coincidences. Many transitions, clearly present in the full projections in Fig. 4, are essentially eliminated in the doubly gated spectra in Figs. 5(a) and 5(c). The final result for the lifetime of 4_1^+ state of ^{204}Po is $\tau(4_1^+; ^{204}\text{Po}) = 23(6)$ ps. It has to be noted that the larger relative uncertainty is mostly due to the smaller centroid shift difference ΔC_{exp} as can be clearly seen in Fig. 5.

The lifetime of the 2_1^+ state in ^{204}Po is not known. We made an attempt to estimate it from the present data. This is illustrated in Fig. 6. The HPGe gate was set on the 426-keV transition, while LaBr gates were set on the 684- and 516-keV transitions, respectively. Thus, we were able to determine an upper limit of 9 ps for the lifetime of the 2_1^+ state in ^{204}Po . An analogous procedure in the case of the 2_1^+ state of ^{206}Po leads to a similar upper limit for the lifetime which however does not improve the precision of the $B(E2; 2_1^+ \rightarrow 0_1^+)$ value reported in Ref. [12]. The final results for the lifetimes of ^{206}Po and ^{204}Po are summarized in Table I, together with the resulting $E2$ reduced transition strengths.

III. DISCUSSION

The onset and the evolution of quadrupole collectivity in even-even nuclei are traditionally tested against four experimental criteria, namely the energy of the first excited 2^+ state $E_x(2_1^+)$, the ratio $R_{4/2} \equiv E_x(4_1^+)/E_x(2_1^+)$, the absolute transition strength $B(E2; 2_1^+ \rightarrow 0_1^+)$, and the ratio $B_{4/2} \equiv B(E2; 4_1^+ \rightarrow 2_1^+)/B(E2; 2_1^+ \rightarrow 0_1^+)$. Even though two of the criteria are uniquely defined only in several special cases of quadrupole collective excitations such as the rigid-rotor rotations ($R_{4/2} \approx 3.33$ and $B_{4/2} \approx 10/7$) and the harmonic vibrations ($R_{4/2} \approx 2$ and $B_{4/2} \approx 2$), in most cases the criteria altogether can serve well as indicators to discriminating be-

TABLE II. Available magnetic moments of the 6^+ and 8^+ states in even-even polonium isotopes with $N \leq 126$. Data are taken from Ref. [11].

Nucleus	^{210}Po	^{208}Po	^{206}Po	^{204}Po	^{202}Po	^{200}Po
$\mu(8_1^+) (\mu_N)$	+7.35(5)	+7.37(5)	+7.34(7)	+7.38(10)	7.45(12)	+7.44(16)
$\mu(6_1^+) (\mu_N)$	5.48(5)	+5.3(6)				

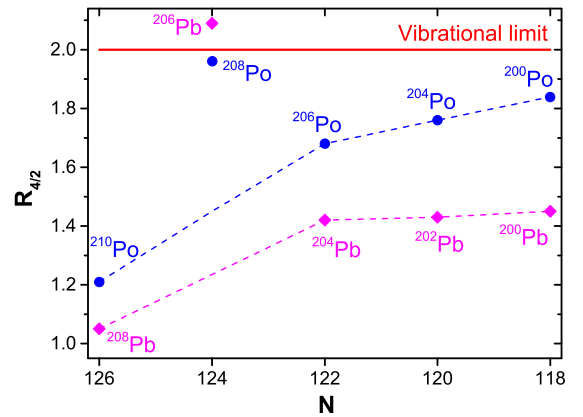


FIG. 7. The evolution of the $R_{4/2}$ ratios in even-even polonium (blue circles) and lead (magenta diamonds) isotopes as a function of neutron number. The dashed lines are drawn to guide the eye in order to highlight the peculiar $R_{4/2}$ ratio at $N = 124$ (^{208}Po and ^{206}Pb).

tween collective [a relatively low $E_x(2_1^+)$, $R_{4/2} \geq 2$, relatively large $B(E2; 2_1^+ \rightarrow 0_1^+)$ value, and $B_{4/2} \geq 1$] and noncollective regimes [a relatively high $E_x(2_1^+)$, $R_{4/2} \leq 2$, relatively low $B(E2; 2_1^+ \rightarrow 0_1^+)$ value, and $B_{4/2} \leq 1.5$]. However, the evolution of these observables in the chain of polonium isotopes with $N \leq 126$ cannot be interpreted unambiguously. Indeed, the energy of the 2_1^+ state decreases significantly from 1181 keV in $^{210}\text{Po}_{126}$ to 686 keV in $^{208}\text{Po}_{124}$ indicating that the 2_1^+ state acquires collectivity after two neutrons are removed from the $N = 126$ shell closure. However, this energy remains almost constant when more neutron pairs are removed down to $^{200}\text{Po}_{116}$ (see Fig. 1 in Ref. [12]), which is a behavior more typical for a seniority type configuration [2–4].

Experimental information on the $B(E2; 2_1^+ \rightarrow 0_1^+)$ values for the even-even polonium isotopes with $N \leq 126$ is scarce. This $E2$ transition strength is not known in the case of ^{208}Po but it apparently increases from 1.84(16) W.u. in ^{210}Po [23] to 18_{-10}^{+14} W.u. in ^{206}Po [12]. This rise in transition strength along with the evolution of the excitation energies of the 2_1^+ states corroborate to the conclusion that the 2_1^+ state of ^{206}Po has already a weakly collective nature [12].

In contrast, the evolution of the $R_{4/2}$ ratios presented in Fig. 7 suggests a different interpretation. It is apparent that besides the unexpectedly high $R_{4/2}$ ratio for ^{208}Po , the ratios for the other nuclei gradually increase towards the vibrational limit but still retain values typical for single-particle seniority-like excitations. The $R_{4/2}$ ratios for ^{206}Po and ^{204}Po , which are 1.68 and 1.76, respectively, agree well with the above observation. It is also worth noting that the evolution of the $R_{4/2}$ ratios in even-even polonium nuclei resembles quite closely the one

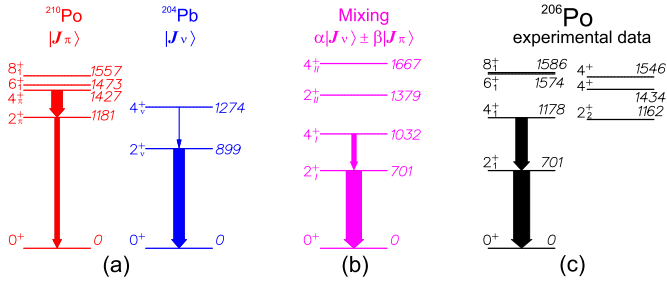


FIG. 8. The mixing scenario for ^{206}Po . Panel (a) shows the pure proton (in red) and neutron (in blue) excitations of ^{206}Po , which are assumed to correspond to the excited states of ^{210}Po and ^{204}Pb , respectively. Panel (b) shows the result from their mixing (in magenta) in comparison with experimental data for ^{206}Po in panel (c). The thickness of the arrows are proportional to the $E2$ transition strengths except for the $B(E2; 2_1^+ \rightarrow 0_1^+)$ value of ^{206}Po (the rightmost level scheme), where the thickness of the arrow represents the lower limit of transition strength.

in the lead isotopes (cf. Fig. 7) including the anomaly at $N = 124$. This observation suggests that the properties of the 2_1^+ and the 4_1^+ states of polonium isotopes are predominately determined by the structures of the 2_1^+ and the 4_1^+ states of the corresponding lead nuclei which are of neutron single-particle seniority-like nature. As a result, it might be expected that the structure of the 2_1^+ and the 4_1^+ states of ^{206}Po and ^{204}Po is dominated by single-particle seniority-like configurations, which is in apparent conflict with the evolution of the $E_x(2_1^+)$ and the $B(E2; 2_1^+ \rightarrow 0_1^+)$ value, as discussed above.

A solution of this ambiguity should be sought by examining the $B_{4/2}$ ratios as a last and decisive criterion for determining the nature of the 2_1^+ and the 4_1^+ states of ^{206}Po and ^{204}Po . In the case of ^{206}Po the new experimental results for the $B(E2; 4_1^+ \rightarrow 2_1^+)$ values (see Table I) and the $B(E2; 2_1^+ \rightarrow 0_1^+) = 1330_{-800}^{+1000} e^2 \text{fm}^4$ reported in Ref. [12] lead to $B_{4/2} = 0.28_{-0.13}^{+0.48}$. Despite the large uncertainties this is a rather small value. Such small $B_{4/2}$ ratios are rarely observed [24–28]. In nuclei near closed shells small $B_{4/2}$ ratios are usually interpreted as a manifestation of seniority dominated structures [4–6]. A comparison of the $B_{4/2}$ ratio for ^{206}Po and the ones for ^{210}Po [$B_{4/2} = 2.43(39)$] [23] and ^{204}Pb [$B_{4/2} = 8.1(2) \times 10^{-4}$] [29] indicates that the structure of the 2_1^+ and the 4_1^+ states of ^{206}Po may arise from a mixing

of the $\pi(h_{9/2})^2$ and the $\nu(f_{5/2})^{-2}$ seniority configurations that determine the structures of the yrast states of ^{210}Po and ^{204}Pb , respectively.

A microscopic justification of the above hypothesis can be based on the fact that the Fermi levels for protons and neutrons in ^{206}Po are quite different. The valence protons are located predominantly in the $\pi h_{9/2}$ orbital just above the $Z = 82$ shell closure, while the valence neutrons occupy predominantly the $\nu f_{5/2}$ orbital below the $N = 126$ shell closure. The energy difference between these two orbitals is about 4 MeV [30]. Due to this decoupling the proton and the neutron excitations of ^{206}Po can be considered relatively independent from each other, i.e., the excited yrast states of ^{206}Po can be considered as a mixture of proton and neutron excitations, the properties of which are determined by the excited yrast states of ^{210}Po and ^{204}Pb , respectively. Since the structure of excited yrast states of ^{210}Po and ^{204}Pb in a first order approximation can be considered as being dominated by the $\pi(h_{9/2})^2$ and the $\nu(f_{5/2})^{-2}$ seniority configurations, respectively, then the excited yrast states of ^{206}Po can be considered to be a mixture of these seniority configurations for the respective angular momenta. It has to be stressed, however, that in reality the structure of excited yrast states of ^{210}Po and ^{204}Pb involve more configurations. Especially in the case of ^{204}Pb , it can be expected that configurations such as $\nu(f_{5/2}^{-1}p_{1/2}^{-1})$, $\nu(f_{5/2}^{-1}p_{3/2}^{-1})$, and $\nu(p_{3/2}^{-2})$ make significant contribution to the structures of the excited 2^+ and 4^+ states. Accounting for all possible configurations requires full scale shell model calculations, which are outside the scope of the present work. Here we simplify the problem by considering only the dominant $\pi(h_{9/2})^2$ and the $\nu(f_{5/2})^{-2}$ seniority $\nu = 2$ configurations in an attempt to obtain a qualitative understanding of the new experimental data for ^{206}Po . There is an important consequence, which follows from this approximation, namely that the described mixing produces only the 2_1^+ and the 4_1^+ states of ^{206}Po . This is a result from the fact that the $\nu(f_{5/2})^{-2}$ configuration can produce states with seniority $\nu = 2$ and spin and parity 2^+ and 4^+ , while for the $\pi(h_{9/2})^2$ the $\nu = 2$ multiplet includes 2^+ , 4^+ , 6^+ , and 8^+ states. Hence, under the above assumptions it can be expected that the yrast 6^+ and 8^+ states of ^{206}Po are dominated by the $\pi(h_{9/2})^2$ configuration, as those of ^{210}Po . This assumption is justifiable at least for the 8_1^+ states in even-even polonium isotopes, as can be seen from the constancy of the magnetic moments of these states (see Table II), which

TABLE III. Properties of the yrast states of ^{210}Po , ^{204}Pb , and ^{202}Pb used as input data for the mixing calculations for ^{206}Po and ^{204}Po .

$^{210}\text{Po}^a$				$^{204}\text{Pb}^b$				$^{202}\text{Pb}^c$			
J_i^π	E_x (keV)	J_f^π	$B(E2; J_i \rightarrow J_f)$ ($e^2 \text{fm}^4$)	J_i^π	E_x (keV)	J_f^π	$B(E2; J_i \rightarrow J_f)$ ($e^2 \text{fm}^4$)	J_i^π	E_x (keV)	J_f^π	$B(E2; J_i \rightarrow J_f)$ ($e^2 \text{fm}^4$)
2_1^+	1181	0_1^+	136(21)	2_1^+	899	0_1^+	334(4)	2_1^+	961	0_1^+	>6.9
4_1^+	1427	2_1^+	335(14)	4_1^+	1274	2_1^+	0.272(6)	4_1^+	1382	2_1^+	20.5(15)
6_1^+	1473	4_1^+	229(7)								
8_1^+	1557	6_1^+	84(3)								

^aThe data are taken from Ref. [23] and references therein.

^bThe data are taken from Ref. [29].

^cThe data are taken from Ref. [33].

TABLE IV. Results from the mixing calculations for ^{206}Po in comparison with the experimental data. The mixing calculations are performed by using input data from Table III and $V_{\text{mix}} = 308$ keV. See text for details.

Results from the mixing calculations						Experimental data			
J_i^π	$E_{x,\text{mix}}$ (keV)	α^2 (neutrons)	β^2 (protons)	J_f^π	$B_{\text{mix}}(E2; J_i \rightarrow J_f)$ ($e^2 \text{fm}^4$)	J_i^π	$E_{x,\text{exp}}$ (keV)	J_f^π	$B_{\text{exp}}(E2; J_i \rightarrow J_f)$ ($e^2 \text{fm}^4$)
2_1^+	701	0.71	0.29	0^+	469(21)	2_1^+	701	0_1^+	$1300_{-800}^{+1000\text{a}}$
2_{II}^+	1379					2_2^+	1162		
4_1^+	1032	0.62	0.38	2_1^+	137(5)	4_1^+	1178	2_1^+	$359(28)^{\text{b}}$
4_{II}^+	1667					4_2^+	1434		

^aFrom Ref. [12].

^bFrom the present work.

can be interpreted as due to a structure dominated by the $\pi(h_{9/2})^2$ configuration perturbed by small admixtures caused by core-polarization effects [31,32]. The fact that the magnetic moments of the 6_1^+ states of ^{210}Po and ^{208}Po are identical (see Table II) implies that these states may also be dominated by the $\pi(h_{9/2})^2$ configuration.

The mixing scenario under the above assumptions is depicted in Fig. 8. The available data for the relevant semimagic nuclei, ^{210}Po and ^{204}Pb , are summarized in Table III and are presented in Fig. 8(a). In our mixing calculations the excited states of these nuclei serve as pure proton and neutron excitations. The mixed $2_{\text{I,II}}^+$ and the mixed $4_{\text{I,II}}^+$ states can be expressed as $|J_{\text{I,II}}\rangle = \alpha|J_\nu\rangle \pm \beta|J_\pi\rangle$ [see Fig. 8(b)], where the “+” and “−” signs are associated with the “I” and “II” labels, respectively. By imposing the condition that the energy of the lower 2_1^+ mixed state coincides with the energy of the 2_1^+ state of ^{206}Po , we have calculated that the effective proton-neutron residual interaction causing the mixing is $V_{\text{mix}} = 308$ keV. The mixing amplitudes for the $2_{\text{I,II}}^+$ states and the $B(E2; 2_1^+ \rightarrow 0^+)$ transition strength are also calculated (see Table IV). The same quantities are calculated for the $4_{\text{I,II}}^+$ states by assuming that the mixing matrix element V_{mix} is identical between the pure $2_{\pi(\nu)}^+$ and $4_{\pi(\nu)}^+$ states.

The results from the mixing calculations for ^{206}Po are summarized and compared to the experimental data in Table IV and in Figs. 8(b) and 8(c). The mixed 2_{II}^+ and 4_{II}^+ states appear at about 200 keV higher than any known off-yrast 2^+ and 4^+ states of ^{206}Po . In addition, there are no experimental data on the transition strengths from the off-yrast states. All this makes the unambiguous assignments of these states to any experimentally known state of ^{206}Po impossible. The mixed 2_1^+ and 4_1^+ states are neutron dominated, though the 2_1^+ is more pronounced (Table IV). The 4_1^+ state is at only 146 keV below the 4_1^+ state of ^{206}Po . The $B_{\text{mix}}(E2; 4_1^+ \rightarrow 2_1^+)$ transition strength accounts for only about 38(3)% of the experimental value. This signals that the main assumption in the mixing calculations, namely that the excited yrast states of ^{206}Po can be considered as an admixture of the seniority $\nu = 2\pi(h_{9/2})^2$ and $\nu(f_{5/2})^{-2}$ configurations, are already breaking down. Apparently, the admixture of the seniority $\nu = 2\pi(h_{9/2})^2$ and $\nu(f_{5/2})^{-2}$ configurations cannot contribute more than 38% to the structure of the 4_1^+ state of ^{206}Po . This allows us to conclude that the structure of the 4_1^+ state of ^{206}Po

is dominated by collective excitations while the contribution of the seniority $\nu = 2\pi(h_{9/2})^2$ and $\nu(f_{5/2})^{-2}$ configurations is secondary by size. The $B_{\text{mix}}(E2; 2_1^+ \rightarrow 0^+)$ transition strength is close to the lower limit of the experimentally determined one. Because of the large uncertainty of the experimental $B(E2; 2_1^+ \rightarrow 0_1^+)$ transition strength it is difficult to quantify to what extent the mixing calculations describe the experimental data. Even though the collective configurations may dominate the structure of the 2_1^+ state of ^{206}Po , the contribution of the admixture of the seniority $\nu = 2\pi(h_{9/2})^2$ and $\nu(f_{5/2})^{-2}$ configurations is still noticeable. It is worth noting that the mixing calculations lead to a ratio $B_{4/2,\text{mix}} = 0.29(2)$, which is considerably smaller than 1 and in agreement with the experimental ratio $B_{4/2} = 0.28_{-0.13}^{+0.48}$. Apparently this small $B_{4/2,\text{mix}}$ ratio results from the small experimental $B(E2; 4_1^+ \rightarrow 2_1^+)$ value in ^{204}Pb (see Table III). A similar mechanism may be the reason for the low experimental $B_{4/2}$ in ^{206}Po —both 2_1^+ and 4_1^+ of ^{206}Po are collective states but the extremely low $B_{4/2}$ ratio in ^{204}Pb propagates to the low $B_{4/2}$ ratio in ^{206}Po .

We have applied the same approach to mixing calculations for ^{204}Po . This mixing scenario is depicted in Fig. 9 and the results of the calculations are summarized in Table V. In this case the properties of the pure neutron excitations of ^{204}Po are approximated by the properties of the yrast states of ^{202}Pb [see Fig. 9(a) and Table III] which are assumed to

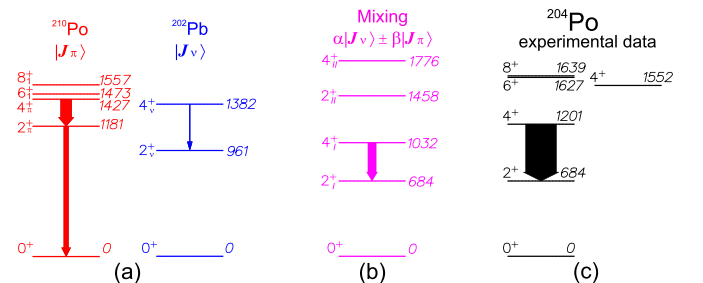


FIG. 9. The mixing scenario for ^{204}Po . Panel (a) shows the pure proton (in red) and neutron (in blue) excitations of ^{204}Po which are assumed to correspond to the excited states of ^{210}Po and ^{202}Pb , respectively. Panel (b) shows the result from their mixing (in magenta) in comparison with experimental data for ^{204}Po in panel (c). The thickness of the arrows are proportional to the $E2$ transition strengths.

TABLE V. Results from the mixing calculations for ^{204}Po in comparison with the experimental data. The mixing calculations are performed by using input data from Table III and $V_{\text{mix}} = 371$ keV. See text for details.

Results from the mixing calculations						Experimental data			
J_i^π	$E_{x,\text{mix}}$ (keV)	α^2 (neutrons)	β^2 (protons)	J_f^π	$B_{\text{mix}}(E2; J_i \rightarrow J_f)$ ($e^2 \text{fm}^4$)	J_i^π	$E_{x,\text{exp}}$ (keV)	J_f^π	$B_{\text{exp}}(E2; J_i \rightarrow J_f)$ ($e^2 \text{fm}^4$)
2_1^+	684	0.64	0.36	0^+		2_1^+	684	0_1^+	
2_{II}^+	1458								
4_1^+	1032	0.53	0.47	2_1^+	251(9)	4_1^+	1201	2_1^+	$939_{-195}^{+326\text{a}}$
4_{II}^+	1776					4_2^+	1552		

^aFrom the present work.

be predominantly determined by the seniority $\nu = 2 \nu(f_{5/2})^2$ configuration. Like in the case of ^{206}Po , the properties of the pure proton excitations of ^{204}Po are assumed to be determined by the properties of the yrast states of ^{210}Po , which are dominated by the $\pi(h_{9/2})^2$ seniority $\nu = 2$ configuration. The requirement that the energy of the lower 2_1^+ mixed state coincides with the energy of the 2_1^+ state of ^{204}Po leads to a mixing matrix element $V_{\text{mix}} = 371$ keV. Since the information of the low-lying 2^+ and 4^+ states of ^{204}Po is more scarce than the one for ^{206}Po [see Fig. 9(c)] the assignment of the mixed 2_{II}^+ and 4_{II}^+ states to any experimentally known state of ^{204}Po is also impossible (see Table V). The mixed 2_1^+ state is still neutron dominated but less pronounced than the one in the case of ^{206}Po . The lack of the experimental $B(E2; 2_1^+ \rightarrow 0_1^+)$ value and the impossibility to calculate the $B_{\text{mix}}(E2; 2_1^+ \rightarrow 0^+)$ value do not allow for any further insights into the structure of the 2_1^+ state of ^{204}Po . The mixed 4_1^+ state appears at 169 keV below the 4_1^+ state of ^{204}Po [see Figs. 9(b) and 9(c)]. This state is calculated to have essentially a balanced proton-neutron character. The $B_{\text{mix}}(E2; 4_1^+ \rightarrow 2_1^+)$ transition strength extracted from the mixing calculations accounts only for about 27(8)% of the experimental value [see Figs. 9(b) and 9(c) and Table V]. The resemblance between the mixing calculations and the experimental data worsens from ^{206}Po to ^{204}Po even though the $B(E2; 4_1^+ \rightarrow 2_1^+)$ value in ^{202}Pb (see Table III) is by a factor of 100 larger than the one in ^{204}Pb . This is a clear indication that the main assumption in our mixing calculations is becoming increasingly invalid when the number of neutron holes increases. This implies that the contribution of the admixture of the seniority $\nu = 2 \pi(h_{9/2})^2$ and $\nu(f_{5/2})^2$ configurations to the excited yrast states of ^{204}Po becomes less important. Hence, the structure of the excited yrast states of ^{204}Po , or at least that of the 4_1^+ state, are dominated by collective excitations.

IV. SUMMARY

In the present study we have measured the lifetimes of the 4_1^+ states of $^{204,206}\text{Po}$ in an attempt to determine at what neutron number the transition from single-particle seniority-like mode to collective mode occurs. The derived absolute transition strengths were analyzed in the framework of a mixing model with the main assumption that the structure of the 2_1^+ and 4_1^+ states of these nuclei is determined by an admixture of the seniority $\nu = 2 \pi(h_{9/2})^2$ and $\nu(f_{5/2})^2$ configurations. Even though this is a very crude and equivocal approximation, the results from the calculations indicated that the 4_1^+ states of $^{204,206}\text{Po}$ are of collective nature. Based on that, we conclude that for the 4_1^+ states the transition from single-particle to collective mode occurs above neutron number 124. It has to be noted, however, that even though this conclusion seems plausible, more experimental data and more thorough theoretical investigations are needed to fully understand the process. To complete this study it is necessary to experimentally determine all missing $B(E2)$ transition strengths between yrast states of polonium isotopes from ^{208}Po down to ^{204}Po . On the theoretical side, obtaining a description of these states in the framework of large-scale shell model calculations with realistic interaction is apparently also essential.

ACKNOWLEDGMENTS

M.S. acknowledges support by the Bulgarian Ministry of Education and Science under the National Research Program “Young scientists and post-doctoral students”, RD-22-862/08.04.2019. This work was supported by the partnership agreement between the University of Cologne and University of Sofia, by the Bulgarian National Science Fund under Grant No. DN08/23/2016, by the DFG under Grant No. GRK 2128, by the BMBF under Grants No. 05P18RDCIA, No. 5P18RDFN9, and No. 05P19RDFN1, and by the UK-STFC.

- [1] M. G. Mayer, *Phys. Rev.* **78**, 16 (1950).
- [2] A. de Shalit and I. Talmi, *Nuclear Shell Theory* (Academic, New York, 1963).
- [3] I. Talmi, *Nucl. Phys. A* **172**, 1 (1971).
- [4] I. Talmi, *Simple Models of Complex Nuclei: The Shell Model and Interacting Boson Model* (Harwood Academic, Chur, Switzerland, 1993).




- [5] J. J. Ressler, R. F. Casten, N. V. Zamfir, C. W. Beausang, R. B. Cakirli, H. Ai, H. Amro, M. A. Caprio, A. A. Hecht, A. Heinz, S. D. Langdown, E. A. McCutchan, D. A. Meyer, C. Plettner, P. H. Regan, M. J. S. Sciacchitano, and A. D. Yamamoto, *Phys. Rev. C* **69**, 034317 (2004), and references therein.
- [6] R. F. Casten, *Nuclear Structure from a Simple Perspective* (Oxford University Press, New York, 2000).


- [7] R. F. Casten, *Phys. Lett. B* **152**, 145 (1985).
- [8] H. Mach, A. Korgul, M. Górska, H. Grawe, I. Matea, M. Stănoiu, L. M. Fraile, Y. E. Penionzkevich, F. D. Santos, D. Verney, S. Lukyanov, B. Cederwall, A. Covello, Z. Dlouhý, B. Fogelberg, G. De France, A. Gargano, G. Georgiev, R. Grzywacz, A. F. Lisetskiy *et al.*, *Phys. Rev. C* **95**, 014313 (2017).
- [9] K. Heyde, J. Jolie, J. Moreau, J. Ryckebusch, M. Waroquier, P. Van Duppen, M. Huyse, and J. L. Wood, *Nucl. Phys. A* **466**, 189 (1987).
- [10] J. J. Ressler, C. W. Beausang, H. Ai, H. Amro, M. A. Caprio, R. F. Casten, A. A. Hecht, S. D. Langdown, E. A. McCutchan, D. A. Meyer, P. H. Regan, M. J. S. Szczytko, A. D. Yamamoto, and N. V. Zamfir, *Phys. Rev. C* **69**, 034331 (2004).
- [11] N. J. Stone, *At. Data Nucl. Data Tables* **90**, 75 (2005).
- [12] T. Grahn, J. Pakarinen, L. Jokiniemi, M. Albers, K. Auranen, C. Bauer, C. Bernards, A. Blazhev, P. A. Butler, S. Bönig, A. Damyanova, T. De Coster, H. De Witte, J. Elseviers, L. P. Gaffney, M. Huyse, A. Herzán, U. Jakobsson, R. Julin, N. Kesteloot *et al.*, *Eur. Phys. J. A* **52**, 340 (2016).
- [13] A. M. Baxter, A. P. Byrne, G. D. Dracoulis, R. A. Bark, F. Riess, A. E. Stuchbery, M. C. Kruse, and A. R. Poletti, *Nucl. Phys. A* **515**, 493 (1990).
- [14] U. Hagemann, W. Neubert, and W. Schulze, *Nucl. Phys.* **175**, 428 (1971).
- [15] A. Linnemann, Ph.D. thesis, Universität zu Köln, 2006.
- [16] J.-M. Régis, N. Saed-Samii, M. Rudigier, S. Ansari, M. Dannhoff, A. Esmaylzadeh, C. Fransen, R.-B. Gerst, J. Jolie, V. Karayonchev, C. Müller-Gatermann, and S. Stegemann, *Nucl. Instrum. Methods Phys. Res. A* **823**, 72 (2016).
- [17] J.-M. Régis, H. Mach, G. S. Simpson, J. Jolie, G. Pascovici, N. Saed-Samii, N. Warr, A. Bruce, J. Degenkolb, L. M. Fraile, C. Fransen, D. G. Ghita, S. Kisyov, U. Koester, A. Korgul, S. Lalkovski, N. Mărginean, P. Mutti, B. Olaizola, Z. Podolyak, P. H. Regan, O. J. Roberts, M. Rudigier, L. Stroe, W. Urban, and D. Wilmsen, *Nucl. Instrum. Methods Phys. Res. A* **726**, 191 (2013).
- [18] M. Stoyanova, G. Rainovski, J. Jolie, N. Pietralla, A. Blazhev, M. Djongolov, A. Esmaylzadeh, L. Gerhard, K. Gladnishki, V. Karayonchev, J. Keatings, R. Kern, D. Kocheva, Th. Kröll, K. Mashtakov, O. Möller, J.-M. Régis, M. Scheck, K. Schomacker, J. Sinclair, C. Urdar, V. Werner, and J. Wiederhold, *Eur. Phys. J. Web Conf.* **194**, 03002 (2018).
- [19] J.-M. Régis, M. Rudigier, J. Jolie, A. Blazhev, C. Fransen, G. Pascovici, and N. Warr, *Nucl. Instrum. Methods Phys. Res. A* **684**, 36 (2012).
- [20] V. Karayonchev, A. Blazhev, A. Esmaylzadeh, J. Jolie, M. Dannhoff, F. Diel, F. Dunkel, C. Fransen, L. M. Gerhard, R. B. Gerst, L. Knafla, L. Kornweibel, C. Müller-Gatermann, J. M. Regis, N. Warr, K. O. Zell, M. Stoyanova, and P. Van Isacker, *Phys. Rev. C* **99**, 024326 (2019).
- [21] J.-M. Régis, J. Jolie, N. Saed-Samii, N. Warr, M. Pfeiffer, A. Blanc, M. Jentschel, U. Köster, P. Mutti, T. Soldner, G. S. Simpson, F. Drouet, A. Vancraeynest, G. de France, E. Clément, O. Stezowski, C. A. Ur, W. Urban, P. H. Regan, Zs. Podolyák *et al.*, *Phys. Rev. C* **95**, 054319 (2017).
- [22] T. Kibédi, T. W. Burrows, M. B. Trzhaskovskaya, P. M. Davidson, and C. W. Nestor, *Nucl. Instrum. Methods Phys. Res. A* **589**, 202 (2008).
- [23] D. Kocheva, G. Rainovski, J. Jolie, N. Pietralla, A. Blazhev, A. Astier, Th. Braunroth, M. L. Cortés, A. Dewald, M. Djongolov, C. Fransen, K. Gladnishki, A. Hennig, V. Karayonchev, J. M. Keatings, J. Litzinger, C. Müller-Gatermann, P. Petkov, M. Scheck, P. Spagnoletti, Ph. Scholz, C. Stahl, R. Stegmann, M. Stoyanova, P. Thöle, N. Warr, V. Werner, W. Witt, D. Wölk, K. O. Zell, P. Van Isacker, and V. Yu. Ponomarev, *Eur. Phys. J. A* **53**, 175 (2017).
- [24] R. B. Cakirli, R. F. Casten, J. Jolie, and N. Warr, *Phys. Rev. C* **70**, 047302 (2004).
- [25] T. Grahn, S. Stolze, D. T. Joss, R. D. Page, B. Saygi, D. O'Donnell, M. Akmali, K. Andgren, L. Bianco, D. M. Cullen, A. Dewald, P. T. Greenlees, K. Heyde, H. Iwasaki, U. Jakobsson, P. Jones, D. S. Judson, R. Julin, S. Juutinen, S. Ketelhut *et al.*, *Phys. Rev. C* **94**, 044327 (2016).
- [26] B. Sayg, D. T. Joss, R. D. Page, T. Grahn, J. Simpson, D. O'Donnell, G. Alharshan, K. Auranen, T. Bäck, S. Boening, T. Braunroth, R. J. Carroll, B. Cederwall, D. M. Cullen, A. Dewald, M. Doncel, L. Donosa, M. C. Drummond, F. Ertugral, S. Ertürk *et al.*, *Phys. Rev. C* **96**, 021301 (2017).
- [27] A. Esmaylzadeh, L. M. Gerhard, V. Karayonchev, J.-M. Régis, J. Jolie, M. Bast, A. Blazhev, T. Braunroth, M. Dannhoff, F. Dunkel, C. Fransen, G. Häfner, L. Knafla, M. Ley, C. Müller-Gatermann, K. Schomacker, N. Warr, and K.-O. Zell, *Phys. Rev. C* **98**, 014313 (2018).
- [28] B. Cederwall, M. Doncel, O. Aktas, A. Ertoprak, R. Liotta, C. Qi, T. Grahn, D. M. Cullen, B. S. Nara Singh, D. Hodge, M. Giles, S. Stolze, H. Badran, T. Braunroth, T. Calverley, D. M. Cox, Y. D. Fang, P. T. Greenlees, J. Hilton, E. Ideguchi *et al.*, *Phys. Rev. Lett.* **121**, 022502 (2018).
- [29] C. J. Chiara and F. G. Kondev, *Nucl. Data Sheets* **111**, 141 (2010).
- [30] E. K. Warburton and B. A. Brown, *Phys. Rev. C* **43**, 602 (1991).
- [31] N. Bräuer, A. Goldmann, J. Hadijuana, M. Von Hartrott, K. Nishiyama, D. Quitmann, D. Riegel, W. Zeitz, and H. Schweickert, *Nucl. Phys. A* **206**, 452 (1973).
- [32] O. Häusser, T. K. Alexander, J. R. Beene, E. D. Earle, A. B. McDonald, F. C. Khanna, and I. S. Towner, *Nucl. Phys. A* **273**, 253 (1976).
- [33] S. Zhu and F. G. Kondev, *Nucl. Data Sheets* **109**, 699 (2008).


Publication III:

6 Tests of collectivity in ^{98}Zr by absolute transition rates

Tests of collectivity in ^{98}Zr by absolute transition rates

V. Karayonchev, J. Jolie, A. Blazhev, A. Dewald, A. Esmaylzadeh , C. Fransen, G. Häfner, L. Knafla, J. Litzinger, C. Müller-Gatermann ,* J.-M. Régis, K. Schomacker, A. Vogt , and N. Warr
Institut für Kernphysik, Universität zu Köln, 50937 Köln, Germany

A. Leviatan  and N. Gavrielov
Racah Institute of Physics, The Hebrew University, Jerusalem 91904, Israel

 (Received 21 May 2020; accepted 16 November 2020; published 14 December 2020)

Lifetimes of low-spin excited states in ^{98}Zr were measured using the recoil-distance Doppler-shift technique and the Doppler-shift attenuation method. The nucleus of interest was populated in a $^{96}\text{Zr}(^{18}\text{O}, ^{16}\text{O})^{98}\text{Zr}$ two-neutron transfer reaction at the Cologne FN Tandem accelerator. Lifetimes of six low-spin excited states, of which four are unknown, were measured. The deduced $B(E2)$ values were compared with Monte Carlo shell model and interacting boson model with configuration mixing calculations. Both approaches reproduce well most of the data but leave challenging questions regarding the structure of some low-lying states.

DOI: [10.1103/PhysRevC.102.064314](https://doi.org/10.1103/PhysRevC.102.064314)

I. INTRODUCTION

Quantum shape-phase transition is a phenomenon present in many physical systems including the atomic nucleus [1,2]. Depending on the proton and the neutron numbers, the ground state of the nucleus can have different shapes. Nuclei having neutron or proton number close to the magic numbers tend to exhibit a spherical ground state. As one moves away from a closed shell, towards midshell, the number of available states to mix under the residual interaction grows rapidly, and collectivity starts to develop. At this point, the proton-neutron correlations start to become dominant, making a deformed shape energetically more favorable, and the ground state becomes deformed. Although the development of collectivity is usually a gradual process, the Zr and Sr isotopes are unique on the nuclear chart as they experience a very rapid onset of collectivity when crossing neutron number $N = 60$. This is well observed through the systematics of the $B(E2; 2_1^+ \rightarrow 0_1^+)$ values (see Fig. 1). Starting from the shell closure at $N = 50$ until $N = 58$, both the Zr and the Sr isotopes have rather low transition probabilities and correspondingly high excitation energies, consistent with a spherical configuration. With the addition of only two neutrons beyond $N = 58$ the $B(E2; 2_1^+ \rightarrow 0_1^+)$ values for both isotopes jump abruptly to the collective values of about 100 W.u., consistent with a deformed ground-state configuration. The increase in the transition probabilities is accompanied by a sharp decrease in the excitation energies of the 2_1^+ to values typical for a rotational nucleus of the mass region. Phenomenologically, this could be interpreted as a coexistence of nuclear configurations with different shapes. For $N < 60$ the ground state is

spherical and a deformed configuration has higher energy. This deformed configuration lowers in energy as neutrons are added and eventually becomes the ground state, whereas the spherical configuration is pushed higher in energy. Indeed, low-lying excited 0^+ states are observed in the region, and their energy drops sharply as $N = 60$ is approached. The scenario of having an excited deformed configuration was recently confirmed by an electron-scattering experiment on the neighboring nucleus ^{96}Zr [3] and in ^{94}Zr in a neutron-scattering experiment [4]. Similarly, coexistence of deformed and spherical configurations was also observed in $^{96,98}\text{Sr}$ isotopes in a Coulomb excitation experiment performed at ISOLDE [5,6].

Already in the late 1970s, it has been pointed out by Federman and Pittel that the strong isoscalar attractive proton-neutron interaction between the spin-orbital partners, in particular, the $\pi(1g_{9/2})$ and the $\nu(1g_{7/2})$, could be responsible for the rapid emergence of deformation [15–17]. As neutrons are added beyond the $\nu(d_{5/2})$ orbital, the $\nu(1g_{7/2})$ will also start to fill. Due to the strong isoscalar interaction, the gap between the $\pi(1g_{9/2})$ and the $\pi(2p_{1/2})$ is reduced, which makes it energetically favorable for protons to be promoted from the $\pi(2p_{1/2})$ into the $\pi(1g_{9/2})$ orbital. The filling of the $\pi(1g_{9/2})$ orbital, successively, lowers the $\nu(1g_{7/2})$, further promoting neutrons into it. The breaking down of the pairing π - π and ν - ν correlations and the development of spatial π - ν correlation leads to deformation. This qualitative description was also supported by Hartree-Fock-Bogoliubov (HFB) and shell-model calculations, although in a very limited valence space from the current perspective, using a ^{94}Sr core [17]. The calculations also showed that the first excited 0^+ state in ^{98}Zr is strongly mixed and is, thus, possibly deformed. It is important to point out that the specific ordering of the orbitals around $A = 100$ makes this effect very strong allowing for the rapid onset of collectivity.

*Present address: Physics Division, Argonne National Laboratory, Argonne, Illinois 60439, USA.

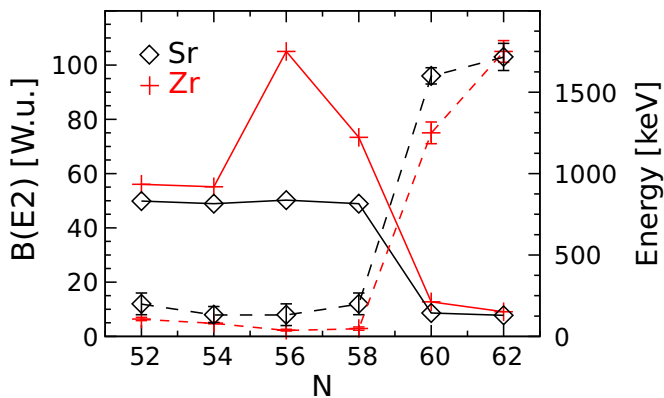


FIG. 1. The energies of the first excited 2^+ states for Zr and Sr isotopes with $N = 52$ – 62 (symbols connected by a solid line), together with the $B(E2; 2^+ \rightarrow 0^+)$ (symbols connected by a dashed line). Data are taken from the nuclear data sheets [7–13]. The $B(E2; 2^+ \rightarrow 0^+)$ value for ^{98}Zr is taken from Ref. [14].

The microscopic origin of the strong interaction between the spin-orbit partner orbitals can be understood in terms of the tensor-force component of the nucleon-nucleon interaction [18,19], which is a direct consequence of its meson exchange character. The importance of the tensor force in the shell evolution has been outlined in Ref. [20]. In the same publication, the authors have also stressed the importance of particle-hole excitations in the evolution of the shell structure especially their role in the transition probabilities. Indeed, the recently performed large-scale shell-model calculations, which do not take particle-hole excitations into account, carried out for Zr isotopes of $N = 50$ – 60 with a ^{78}Ni core, were able to account for the sudden drop in the excitation energy of the first excited 2^+ states at $N = 60$ but were unable to correctly describe the abrupt rise of the transition probabilities [21]. The recent advances of the Monte Carlo shell-model (MCSM) calculations [22], have allowed Togashi *et al.* [23] to perform calculations for the zirconium isotopes of $N = 50$ – 70 with a much larger basis, including also neutron excitation across the $N = 50$ shell closure. The calculation reproduces both the rise of the $B(E2)$ values and the drop in the energies of the first excited states along the isotopic chain. The MCSM calculations also predict a shape coexistence of more than two configurations with different deformations in the region around $N = 60$. Similarly, HFB calculations for ^{98}Zr based on the VAMPIR model [24], predict a coexistence of several strongly mixed shapes, albeit, with noticeable discrepancies with respect to the data on some electromagnetic properties. In another approach, the shape transition in the Zr isotopes was discussed in the framework of configuration mixing in the interacting boson model (IBM-CM) [25–27]. The calculation in Refs. [25,26] suggests the so-called intertwined quantum phase transitions, which involve crossing of two configurations where each of the two configurations undergoes its own quantum phase transition.

The ^{98}Zr nucleus lies on the interface between the spherical and the deformed region making it pivotal to understanding shape transition and the shape coexistence in the $A \approx 100$ region. Very recently, the lifetimes of the yrast 2^+ and 4^+

were determined by the recoil-distance Doppler-shift (RDDS) technique in a fission experiment at GANIL [14], but the lifetimes of the second excited 2^+ and 4^+ states remain unknown up to today. In this article we report on a measurement of the lifetimes of the 2^+_1 , 2^+_2 , 2^+_3 , 4^+_1 , 4^+_2 , and 4^+_3 states. Additionally, the lifetime of the 3^-_1 state has been measured.

II. EXPERIMENT

The nucleus of interest was populated in the $^{96}\text{Zr}(^{18}\text{O}, ^{16}\text{O})^{98}\text{Zr}$ two-neutron transfer reaction. An average beam current of 1 pA with an energy of 50 MeV was provided by the Cologne 10 MV FN-Tandem accelerator. A 1 mg/cm^2 ^{96}Zr self-supporting foil enriched to 72.47% was stretched inside the Cologne Plunger device [28]. To stop the nuclei ejected after the transfer reactions induced on the target, a 6.5-mg/cm^2 Ta stopper was stretched parallel to the target. The γ rays produced in the experiment were detected by 11 high-purity germanium detectors positioned in two rings around the target chamber. Five detectors were placed at backward angles of 142° relative to the beam axis and six at forward angles of 45° . Recoiling light fragments were detected by an array of six solar cells placed at backward angles inside the target chamber, covering angles between 120° and 165° . The data were recorded at seven target-to-stopper distances (22, 41, 71, 101, 131, 221, and $321 \mu\text{m}$) in triggerless mode. These distances were determined relative to a zero point which is obtained by using the capacitive method as described in Refs. [28,29]. For each distance and each detector ring particle- γ coincidences were sorted off-line.

The particle-gated spectrum for the shortest distance of $22 \mu\text{m}$ is shown in Fig. 2. Due to the low angular granularity of the solar cells and the straggling of the recoiling nuclei out of the target, no clear separation between ^{16}O and ^{18}O could be achieved in the particle spectrum. Hence, the major peaks in the γ -ray spectrum are due to Coulomb excitation in the target and the stopper foils. Transitions belonging to ^{97}Zr and ^{100}Mo are also observed, populated in the single-neutron and the α -transfer reactions, respectively. Despite the presence of many transitions, the ones belonging to ^{98}Zr are well defined and are indicated in Fig. 2. The transition intensities have been measured by integration and were normalized to the intensity of the $2^+_1 \rightarrow 0^+_1$ transition. Additionally, weak transitions from the 0^+_3 and the 0^+_4 states are observed. The intensities of the $0^+_3 \rightarrow 2^+_1$ and the $0^+_4 \rightarrow 2^+_2$ are very low and comparable with the level of the background fluctuation, i.e., 1% of the $2^+_1 \rightarrow 0^+_1$ transition intensity. The experimental information on the observed γ -ray transitions is summarized in Table I.

Using γ - γ coincidences, a level scheme has been built and is shown in Fig. 3. The spectrum gated on the $2^+_1 \rightarrow 0^+_1$ transition is displayed in Fig. 4. This spectrum is also used to check for other feeding contributions not clearly observed in the singles spectrum. Additionally, this spectrum allows for a cross-check of the intensities obtained using the singles γ -ray spectrum by comparing the ratio of the intensities obtained in the singles and the gated spectra. These ratios are consistent within the experimental uncertainties.

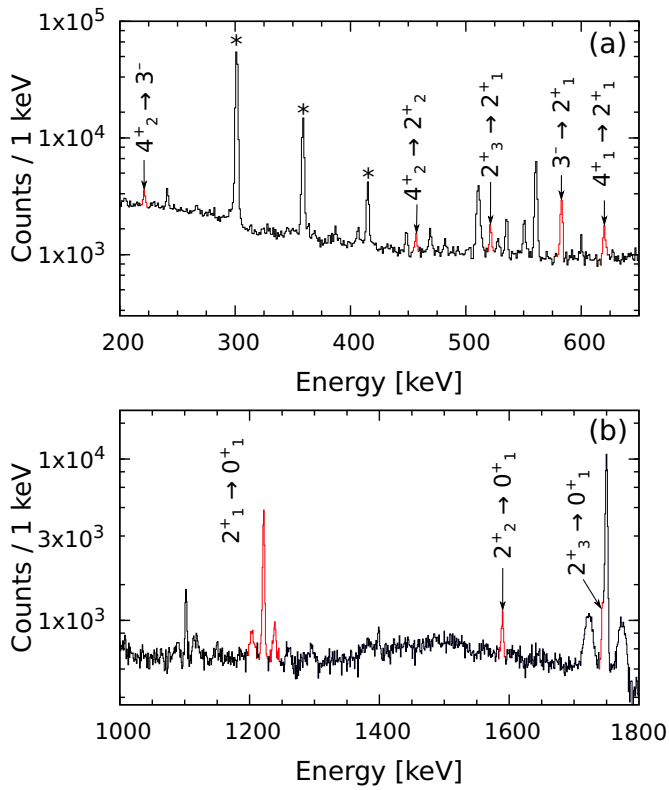


FIG. 2. Particle-gated γ -ray singles spectrum of both detector rings for plunger distance of $22\ \mu\text{m}$. (a) and (b) show different cutouts of the spectrum. The transitions belonging to ^{98}Zr are indicated and colored in red. The peaks belonging to the Coulomb excitation in the ^{181}Ta stopper are indicated with an asterisk.

III. LIFETIME DETERMINATION AND RESULTS

To extract the lifetimes of the 4_2^+ , 4_1^+ , 3_1^- , 2_2^+ , and 2_1^+ states, the RDDS technique has been used. The data has been analyzed using the Bateman equations (BEs) and the differential decay curve method (DDCM) [30]. Here we present only the essential ideas needed for the analysis. For a detailed

TABLE I. Relative transition intensities observed in the experiment normalized to the $2_1^+ \rightarrow 0_1^+$ transition. The energies are taken from Ref. [11].

Transition	Transition energy (keV)	Intensity
$2_1^+ \rightarrow 0_1^+$	1223	100.0(37)
$0_3^+ \rightarrow 2_1^+$	213	1.0(10)
$2_2^+ \rightarrow 0_1^+$	1591	10.4(14)
$2_3^+ \rightarrow 0_1^+$	1744	23.5(50)
$2_3^+ \rightarrow 2_1^+$	522	5.2(10)
$3_1^- \rightarrow 2_1^+$	583	17.7(12)
$4_1^+ \rightarrow 2_1^+$	621	9.0(12)
$0_4^+ \rightarrow 2_1^+$	269	1.0(10)
$4_2^+ \rightarrow 3_1^-$	242	10.1(12)
$4_2^+ \rightarrow 2_2^+$	456	3.1(9)
$4_2^+ \rightarrow 4_1^+$	204	3.1(16)
$4_2^+ \rightarrow 2_1^+$	825	2.9(9)

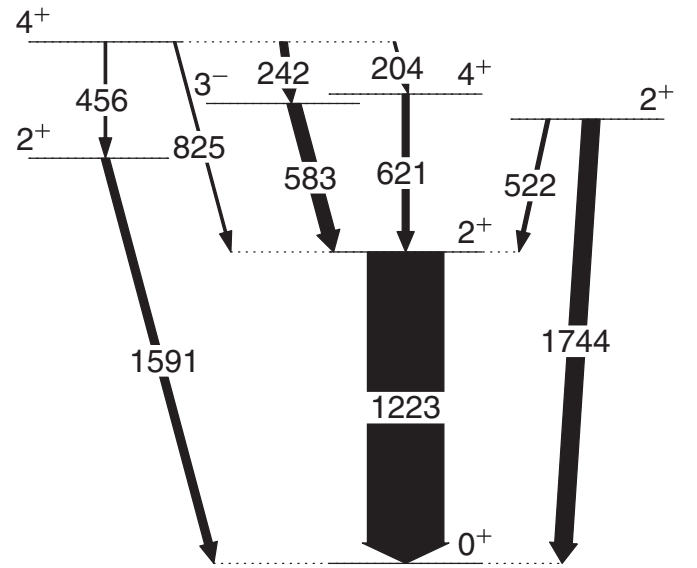


FIG. 3. Level scheme of ^{98}Zr populated in the $^{96}\text{Zr}(^{18}\text{O}, ^{16}\text{O})^{98}\text{Zr}$ two-neutron transfer reaction at beam energy of 50 MeV. The width of the lines are proportional to the transition intensities given in Table I.

review of both methods the reader is referred to Ref. [28]. For the sake of clarity, we use the same notation as in Ref. [28].

An excited state i of a nucleus ejected from the target foil can decay either in-flight or after stopping in the stopper foil. The γ rays emitted by a nucleus in-flight would appear Doppler shifted in the γ -ray spectrum. The corresponding peak is known as the *shifted* peak and its intensity, i.e., number of counts, is given by $I_i^s(t)$, where t is the time of flight of the nucleus between the target and the stopper. If the γ decay occurs after the nucleus has stopped in the stopper foil the peak in the γ -ray spectrum would not experience a Doppler shift and is known as the *unshifted* peak and its intensity is given by $I_i^u(t)$. The so-called decay curve is defined as

$$R_i(t) = I_i^u(t) / [I_i^s(t) + I_i^u(t)]. \quad (1)$$

In the case where state i is not fed from another state, i.e., is directly populated in a nuclear reaction, the decay curve is

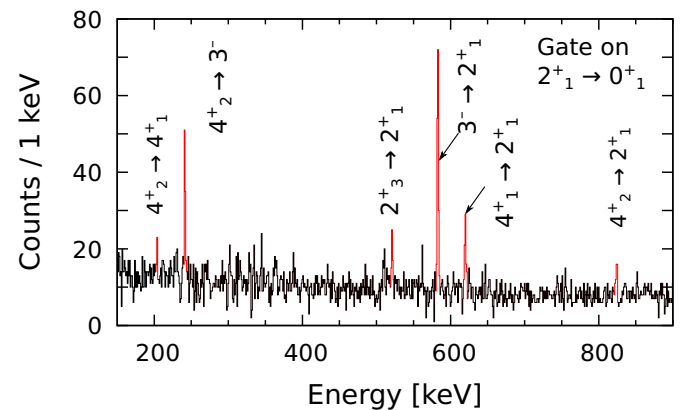


FIG. 4. Particle- γ gated γ -ray spectrum of both detector rings for a plunger distance of $22\ \mu\text{m}$. The transitions belonging to ^{98}Zr are indicated and colored in red.

given by the simple formula,

$$R_i(t) = e^{-t\lambda_i}, \quad (2)$$

where λ_i is the decay constant of state i and is related to the level lifetime τ_i with $\lambda_i = 1/\tau_i$. In a realistic case, the excited state has a complicated feeding pattern. The feeding contributions need to be taken into account to obtain the correct lifetime. One needs to solve the Bateman equations, which are a system of first-order differential equations that relate the populations $n_i(t)$ of the excited states i as a function of the time t , depending on the decay constants λ_i of the states i and the branching ratios. The Bateman equations are as follows:

$$\frac{d}{dt}n_i(t) = -\lambda_i n_i(t) + \sum_{k=i+1}^K \lambda_k n_k(t) b_{ki}. \quad (3)$$

Here k denotes the excited states feeding the state i , b_{ki} are the branching ratios between states k and i , and K is the total number of states. The solutions of these equations with respect to the decay curves $R_i(t)$ is given by

$$R_i(t) = P_i e^{-t\lambda_i} + \sum_{k=i+1}^K M_{ki} [(\lambda_i/\lambda_k) e^{-t\lambda_k} - e^{-t\lambda_i}]. \quad (4)$$

M_{ki} is defined recursively as

$$M_{ki}(\lambda_i/\lambda_k - 1) = b_{ki} P_k - b_{ki} \sum_{m=k+1}^K M_{mk} + \sum_{m=i+1}^{k-1} M_{km} b_{mi} (\lambda_m/\lambda_k), \quad (5)$$

where P_i is the population of the state i . Finding a solution to these equations becomes a tedious task, prone to errors when the feeding pattern is complicated, such as in the case of compound and fission reactions where the spin and the energy transfer of the reaction are high. However, due to the low-spin and low-energy transfer in the $2n$ -transfer reaction, relatively few states are populated. Moreover, these states are populated directly, not through a compound state. In such a case, the feeding pattern is simple, making the direct application of Eq. (4) to the experimental data relatively straightforward.

To conduct the RDDS analysis for each distance, two particle-gated spectra were generated, one for each ring. Drifts induced by radiation damage in the solar cells were compensated by a shift-tracking procedure.

The particle-gated spectra of the backward ring for each distance are displayed in Fig. 5. One can clearly see the evolution of the shifted components for the states of interest. In all the cases except the $4_2^+ \rightarrow 3_1^-$ transition, the shifted and the unshifted peaks are well separated, and their areas were determined by integration. The advantage of integration is that, no assumptions on the shape of the peaks are made and, hence, possible systematic errors are reduced. The systematic error that arises when choosing the fit region and the background parametrization has been taken into account when obtaining the uncertainties of the $R_i(t)$ values. The $4_2^+ \rightarrow 3_1^-$ transition has an energy of 242 keV and the shifted and unshifted components are not well separated. To obtain the areas of the two

components, a fit to the spectra have performed a using two Gaussians, keeping the peak positions and the widths of both components fixed for all the distances.

The average speed of the ejected ^{98}Zr nuclei was determined directly from the spectra, by measuring the energy difference between the shifted and the unshifted peaks for the strongest observed transitions, i.e., $2_1^+ \rightarrow 0_1^+$ and the $3_1^- \rightarrow 2_1^+$ transitions, using both the forward and the backward angles. All four results were consistent. The average velocity was adopted as 1.89(6)% c . Using this velocity we have determined the average time of flight of the ^{98}Zr nuclei between the target and the stopper for each distance and have used these values in the following analysis.

A. Bateman equations analysis

When performing the analysis using the Bateman equations [Eq. (4)] for a certain level, the level lifetime is used as the only fit parameter. The γ -ray transition intensities used in equations are the ones from Table 1. A top-to-bottom approach was adopted where the lifetimes of the highest states are determined first and are used as fixed parameters when determining the lifetimes of the lower-lying states.

The 4_2^+ state has no observed feeders, and one can simply use Eq. (2) to determine the lifetime of the state. A simple exponential decay fit yields a lifetime of $\tau_{4_2^+} = 24(5)$ ps. The fit and the data points are displayed in Fig. 6. Due to the much larger background present in the forward detector ring, especially at the low energies, an analysis for this ring was not possible.

The lifetime $\tau_{4_2^+}$ is then used as a fixed parameter when determining the lifetime of the 2_2^+ state. Here, also the long feeding coming from the 0_4^+ state is taken into account. Using the lifetime $\tau_{2_2^+}$ as the only fit parameter in Eq. (4) the data points for the decay curve of the 2_2^+ state were fitted, resulting in a lifetime of $\tau_{2_2^+} = 9(4)$ ps. The fit to the data points is displayed in Fig. 7.

The lifetime of the 4_1^+ , the 3_1^- , and the 2_1^+ states were obtained using the same procedure. The fits to the data and the obtained lifetimes are shown in Fig. 8.

The experimental uncertainties of the measured lifetimes were obtained by performing a Monte Carlo simulation, similar to Ref. [31]. All the input parameters used in the fit are independently varied within the corresponding experimental uncertainties before performing the fit. Since the individual fit values are distributed symmetrically around a mean value, the error is defined simply as the standard deviation of these values.

B. DDCM analysis

The data for the 2_1^+ , 3_1^- , and 4_1^+ states were also analyzed by the DDCM. This method was developed by Dewald *et al.* in 1989 [30] and is derived from the Bateman equations. The method is transparent and easier to apply when the feeding pattern is complicated. One of the advantages of DDCM is that it relies on the relative distances between the target and the stopper, which are very precisely determined via the active feedback system of the Plunger device [28]. In the framework

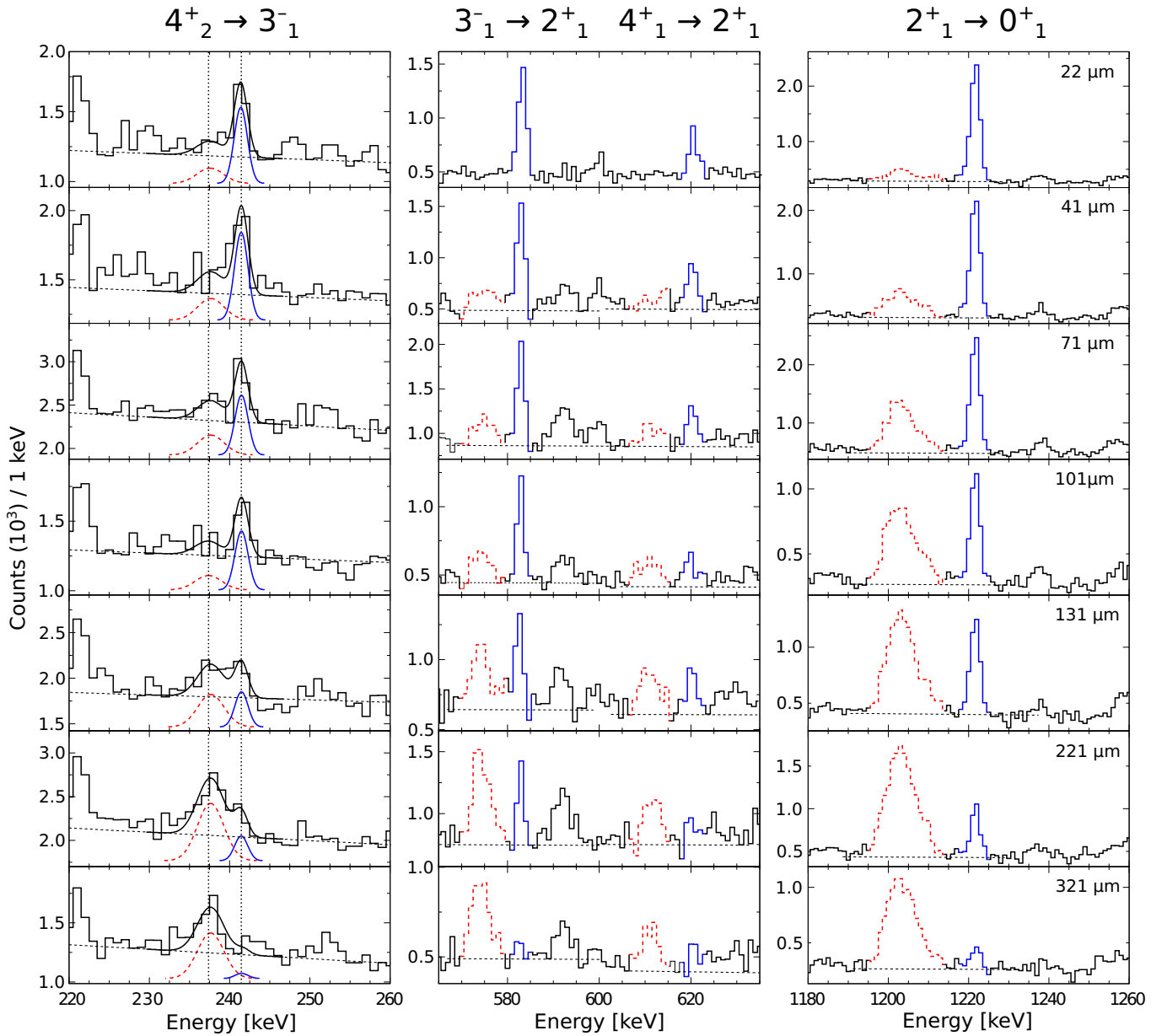


FIG. 5. Particle-gated spectra of the backward detector ring for all distances (indicated in the top-right corner) of the $4_2^+ \rightarrow 3_1^-$ (left), the $3_1^- \rightarrow 2_1^+$, the $4_1^+ \rightarrow 2_1^+$ (middle), and the $2_1^+ \rightarrow 0_1^+$ (right) transitions used to obtain the shifted (dashed red) and the unshifted (blue) intensities. The horizontal dashed lines represent the level of the background used for the determination of the peak areas were obtained.

of the DDCM the lifetime can be derived for each distance from

$$\tau_i(x) = \frac{R_i(x) - \sum_k [b_{ki} I_k(x) / I_i(x)] R_k(x)}{v \frac{d}{dx} S_i(x)} = \frac{U_i(x)}{v \frac{d}{dx} S_i(x)}, \quad (6)$$

where I_i and I_k are the total intensities of the transitions depopulating the states i and k and v is the speed of the ejected nuclei. The sum is carried over all the feeders k of the state of interest i . The numerator can be interpreted as a decay curve which has been corrected for the stopped feeding. The term in the denominator is the shifted component normalized to the

total intensity,

$$S_i(x) = \frac{I_i^s(x)}{I_i^s(x) + I_i^u(x)}. \quad (7)$$

The data were analyzed using the computer code NAPATAU which is described in Ref. [32]. The program performs a piecewise polynomial fit to the shifted intensities $S_i(x)$ to obtain the derivative $d[S_i(x)]/dx$. The derivative is multiplied by a parameter $\tau_i(x)$ and the product $\tau_i(x) d[S_i(x)]/dx$ is fitted simultaneously to the feeder-corrected decay curve values $U_i(x)$. The fit, in this case, has been performed with two second-order polynomials. The parameters $\tau_i(x)$ are the

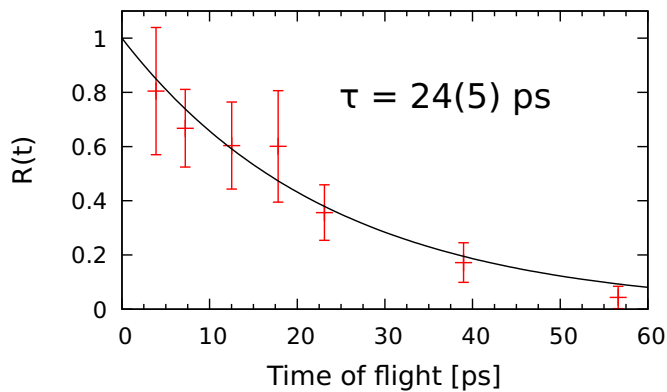


FIG. 6. Fitted decay curve together with the data points for the 4_2^+ state using the $4_2^+ \rightarrow 3_1^-$ transition observed at backwards angle. The obtained lifetime is given as well.

lifetime of the state i by definition. The final value of τ_i is obtained as a weighted average of the individual results. Fits to the data of the backward-detector ring used to extract the lifetimes of the 4_1^+ , the 3^- , and the 2_1^+ states are shown in Fig. 9. The same procedure is performed for the forward-detector ring as well. The results of the backward detector ring are given in Table II.

C. Doppler-shift attenuation analysis of the 2_3^+ state

When the lifetimes of the states are comparable to the average stopping time of the ejecting nuclei inside the stopper, the RDDS technique cannot be applied directly. To obtain the correct lifetime, the decays that happen during the stopping needs to be taken into account by employing the Doppler-shift attenuation (DSA) method. For a detailed review of the method, the reader is referred to Refs. [33,34]. To determine the lifetime of the 2_3^+ state, a DSA analysis has been performed utilizing the program APCAD [35]. In APCAD, the slowing down of the ^{98}Zr ions inside the target and the stopper and the drift between them is modeled using a Monte Carlo simulation in the framework of GEANT4 [36]. The electronic and the nuclear stopping powers used in the simulation are taken from SRIM2013 [37]. The doubly differential cross section of the $^{96}\text{Zr}(^{18}\text{O}, ^{16}\text{O})^{98}\text{Zr}$ reaction used in the simulation has been

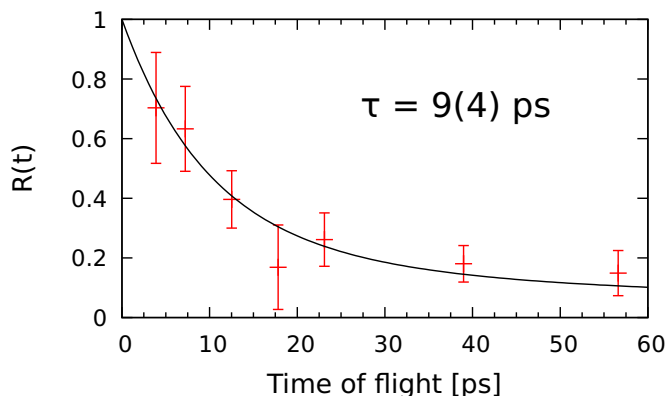


FIG. 7. Same as Fig. 6 but for the $2_2^+ \rightarrow 0_1^+$ transition.

calculated using the GRAZING code [38,39]. After the traces of the individual ions are simulated, APCAD calculates the Doppler shift observed in the individual detectors as a function of the time after the production of the ^{98}Zr nuclei inside the target. The calculations take into account the setup geometry, the kinematic restrictions imposed by the solar cells, and the detector resolutions. Finally, the simulated Doppler-broadened γ -ray line shapes are fitted to the experimental spectra using the level lifetime as the only fit parameter. The fit has been performed to the $2_3^+ \rightarrow 2_1^+$ transition peak. Only the forward detector ring spectra were used since the shifted component of the peak in the backward detector ring spectrum lies in the tail of the 511-keV peak. The fit to the spectra for the 22 and the 41- μm distances are shown in Fig. 10. The errors indicated in the figure include the statistical error of the fit and the systematic errors assuming 10% uncertainty in the stopping powers and 5- μm uncertainty in the distance between the target and the stopper. Additionally, up to 10% long-lived feeding has been assumed as a possible source of systematic error.

The results from the lifetime measurements are summarized in Table II. Adopted values are given and are compared to the recent results from Ref. [14]. Although the value for the 4_1^+ that we report here is consistent with the one from Ref. [14], the lifetime of the 2_1^+ we measure is considerably longer. It should be noted that the lifetimes of Ref. [14] have been determined also in a singles RDDS analysis, but the nucleus was populated in a fission reaction, which makes the feeding pattern severely complicated. Using the measured lifetimes, and the information on the conversion coefficients, the multipolarity mixing ratios and the branching ratios from Ref. [11], the reduced transition probabilities are calculated, and the results are presented in Table III. One can attempt to use the branching of the $2_2^+ \rightarrow 0_3^+$ transition measured in Ref. [40] and evaluated in Ref. [11] in order to estimate the reduced transition probability. However, this leads to an unrealistically large $B(E2)$ value and, furthermore, the indicated branching ratio was not confirmed by the more recent measurement in Ref. [41]. Accordingly, lifetime of the 2_2^+ and the branching of the $2_2^+ \rightarrow 0_3^+$ needs to be further corroborated in order to pin down an accurate $B(E2)$ value.

IV. DISCUSSION

A. Comparison to MCSM calculations

First, we compare the new measured results with the recent large-scale Monte Carlo shell-model calculation of Togashi *et al.* [23]. The calculation reproduced both the drastic rise in the $B(E2)$ values and the drop in the energies of the first excited state in the $N = 50-70$ zirconium isotopes. The results for ^{98}Zr are presented in Table III. We point out different assignments to experimental states of the calculated levels in ^{98}Zr . In the first comparison performed in Ref. [42] (MCSM-1), the first excited 4^+ and 6^+ were assigned to the calculated first excited 4^+ at 1.59 MeV and 6^+ at 1.64 MeV. However, in the more recent work by Ref. [14], these assignments were changed and instead the experimental 4^+ and 6^+ were assigned to the calculated second excited 4^+ at 2.197 MeV

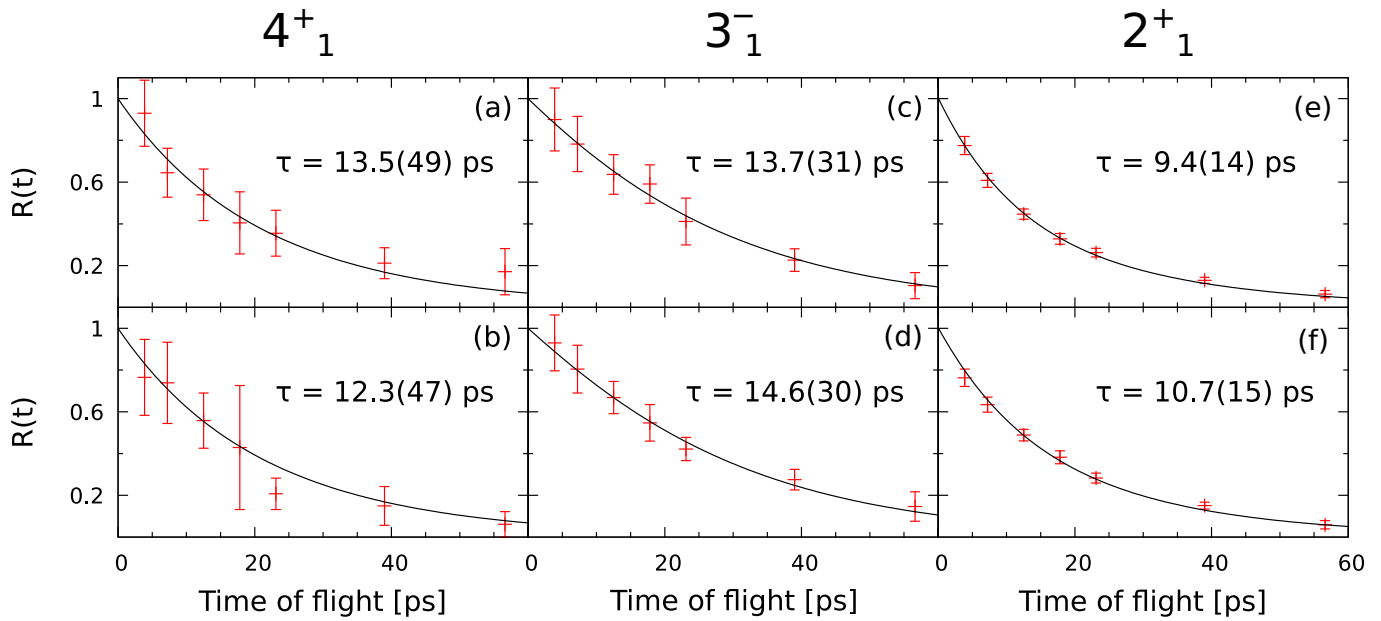


FIG. 8. Fitted decay curve together with the data points: (a) and (b) for the 4_1^+ state, (c) and (d) for the 3_1^- , and (e) and (f) for 2_1^+ . The upper panel is for the backward detector ring, and the lower panel is for the forward detector ring.

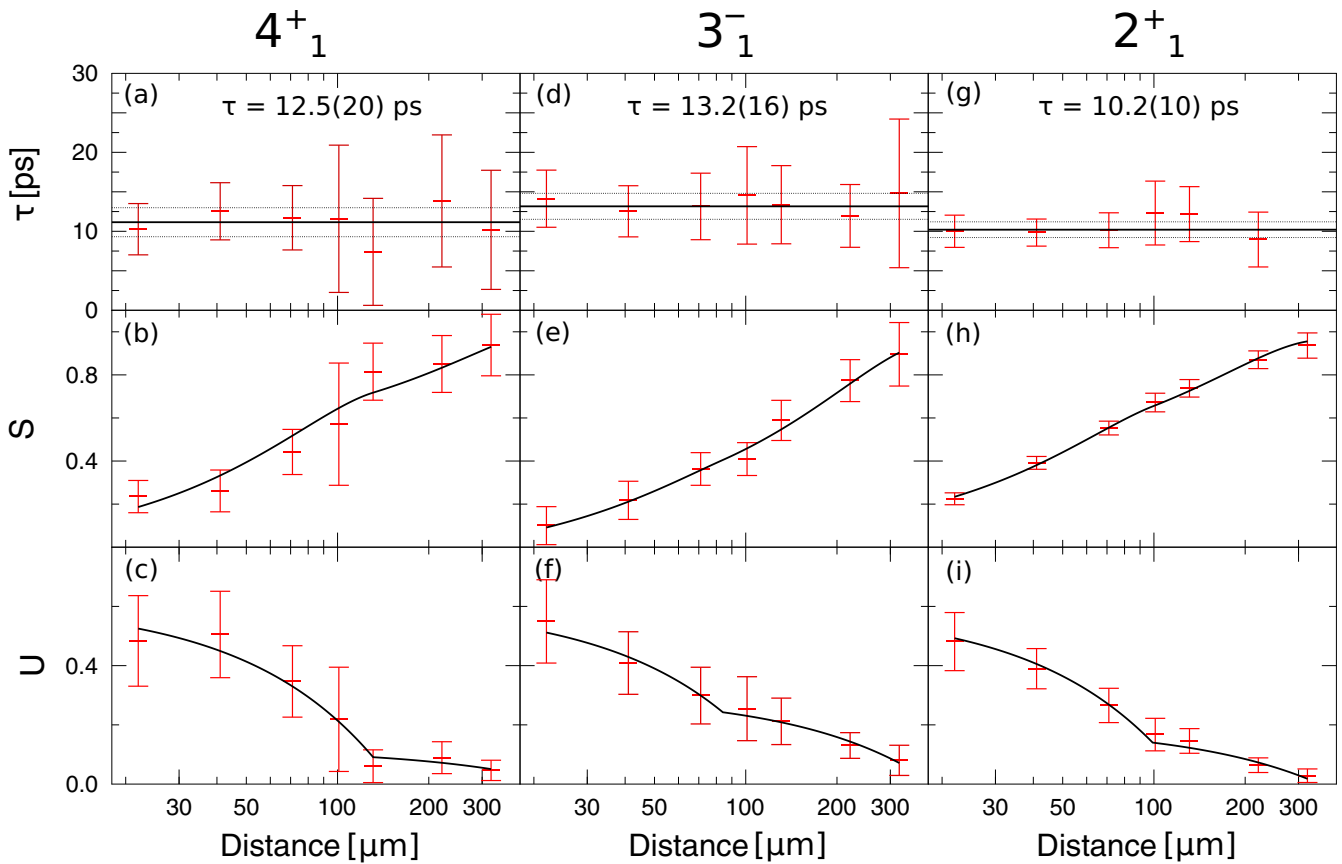


FIG. 9. DDCM analysis (see text) of the backward-detector ring for the 4_1^+ state (a)–(c), for the 3_1^- state (d)–(f), and for the 2_1^+ state (g)–(i). The individual lifetimes obtained in the analysis are displayed in the upper panel. The middle panel shows the evolution of the shifted component and the fit to it used to obtain the derivative $d[S_i(x)]/dx$. The lower panel shows the evolution of the unshifted component and the fit to it used to obtain the individual lifetimes.

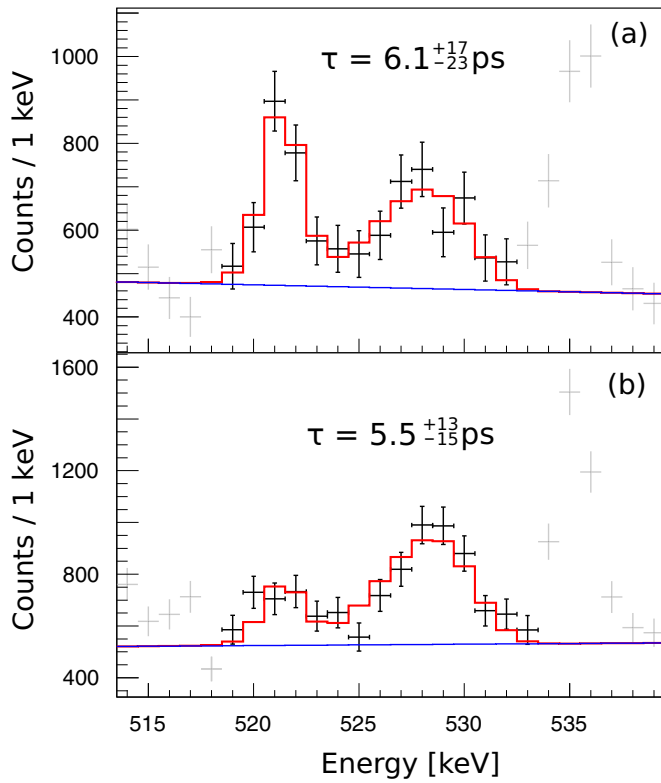


FIG. 10. DSA fits to the Doppler-broadened line shapes of the $2_3^+ \rightarrow 2_1^+$ transition for the (a) 22- μm and the (b) 41- μm distances of the forward detector ring used to obtain the lifetime of the 2_3^+ state.

and 6^+ at 2.668 MeV (MCSM-2). This change improves the agreement for the energies of the states, however, it yields a very low $B(E2; 4_1^+ \rightarrow 2_1^+)$ value of 0.6 W.u. This change does not have such a large effect for the $B(E2; 6_1^+ \rightarrow 4_1^+)$ transition strength as it changes the calculated value from 102

TABLE II. Lifetimes measured in the experiment using the BEs, the DDCM, and the DSA method together with the adopted values given in bold. The results from Ref. [14] are given for comparison.

State	Lifetime (ps)					Lit. ^a
	Backward ring		Forward ring		Adopted	
	BE	DDCM	BE	DDCM		
2_1^+	9.4(14)	10.2(10)	10.7(15)	10.4(10)	10(2)	3.8(8)
2_2^+	9(4)	–	–	–	9(4)	–
3_1^-	13.7(31)	13.2(16)	14.6(30)	13.2(16)	14(3)	–
4_1^+	13.5(49)	12.5(20)	12.3(47)	11.5(19)	13(5)	7.5(15)
4_2^+	24(5)	–	–	–	24(5)	–
	DSA					
			22 μm	41 μm		
2_3^+			$6.1^{+1.7}_{-2.3}$	$5.5^{+1.3}_{-1.5}$	6^{+2}_{-3}	–

^aFrom Ref. [14].

to 87 W.u., whereas the experimental value has been measured as 103.0(35.7) W.u. in Ref. [14].

Taking into account the new experimental $B(E2)$ values of the first and second 4^+ states, the situation is still unclear. Although the $B(E2; 4_1^+ \rightarrow 2_1^+)$ value is best reproduced using the old assignment, the $B(E2; 4_1^+ \rightarrow 2_2^+)$ value agrees better with the new assignment. As mentioned in Ref. [14], the reason might be related to an underestimation of the mixing of the 2^+ states indicating the need for further refinements of the shell-model Hamiltonian. Note that both 2^+ states have a small ground-state decay rate in this theory and this experiment.

B. Comparison to IBM-CM calculation

The framework of the interacting boson model with configuration mixing (IBM-CM) [43,44] was recently employed in a calculation [25–27] of several observables for the chain of zirconium isotopes with neutron numbers 52–70. The calculation considers a $^{90}\text{Zr}_{50}$ core with valence neutrons in the 50–82 major shell and two configurations. The normal A -configuration ($[N_b]$ -boson space) corresponds to no active protons above the $Z=40$ subshell gap, and the intruder B -configuration ($[N_b + 2]$ -boson space) corresponds to a two-proton excitation from below to above this gap, creating $2p$ - $2h$ states. The resulting eigenstates $|\Psi; L\rangle$ with angular momentum L are linear combinations of the wave-functions Ψ_A and Ψ_B in the two spaces $[N_b]$ and $[N_b + 2]$,

$$|\Psi; L\rangle = a |\Psi_A; [N_b], L\rangle + b |\Psi_B; [N_b + 2], L\rangle, \quad (8)$$

with $a^2 + b^2 = 1$ and $N_b = 4$ is the appropriate boson number for ^{98}Zr .

In Fig. 11, we compare the IBM-CM calculation of Refs. [25,26] (named IBM-CM-1) to the present new experimental results for ^{98}Zr . The spectrum is divided into sectors of normal states (in blue) and intruder states (in black). The 0_1^+ and 2_3^+ states are calculated in the IBM-CM-1 to be normal states, part of a senioritylike spectrum of neutron single-particle excitations, which is mostly outside the IBM model space. Therefore, the experimental 4_2^+ level is not considered in the calculation. The remaining states, shown in Fig. 11, have an intruder character and are calculated to be quasispherical or weakly deformed. Accordingly, the experimental 0_2^+ , 2_1^+ , (0_3^+ , 2_2^+ , 4_1^+), (0_4^+ , 2_4^+ , 3_1^+ , 4_3^+ , 6_1^+) states correspond to calculated states dominated by U(5) components with $n_d \approx 0$ –3, respectively, within the intruder part of the wave-function $|\Psi_B; [N_b + 2], L\rangle$. The resulting mixing between the two configurations is weak, e.g., $a^2=98.2\%$ for the ground-state (0_1^+) and $b^2=98.2\%$ for the intruder-state (0_2^+). These findings result in an agreement with the new experimental results of the current paper as seen in Table III and Fig. 11. The weak $E2$ rates $B(E2; 2_2^+ \rightarrow 0_2^+) = 1.8^{+1.4}_{-0.6}$ W.u. and strong $E2$ rates $B(E2; 2_2^+ \rightarrow 2_1^+) = 46^{+35}_{-14}$ W.u. conform with the IBM-CM-1 interpretation of quasiphonon structure for the intruder band. This interpretation agrees also with the previously measured $E2$ rates for $0_3^+ \rightarrow 2_1^+$, $0_4^+ \rightarrow 2_2^+$, $0_4^+ \rightarrow 2_1^+$ [11], and $6_1^+ \rightarrow 4_1^+$ [14], listed in Table III. The measured weak $E2$ rates $B(E2; 2_3^+ \rightarrow 0_1^+) = 0.14^{+0.12}_{-0.04}$, $B(E2; 2_3^+ \rightarrow$

TABLE III. Experimentally deduced transition probabilities for ^{98}Zr from the current experiment and from Refs. [11,14] in comparison with theoretical calculations. The conversion coefficient, the multipolarity mixing ratios, and the branching ratios are taken from Ref. [11] if not otherwise mentioned.

Transition	$B(E2)$ (W.u.)					IBM-CM-2 ^e
	This paper	Singh <i>et al.</i> ^a	MCSM-1 ^b	MCSM-2 ^c	IBM-CM-1 ^d	
$B(E2; 2_1^+ \rightarrow 0_1^+)$	$1.1^{+0.3}_{-0.2}$	2.9(6)	0.0	0.0	1.35	9.6
$B(E2; 2_1^+ \rightarrow 0_2^+)$	11^{+3}_{-2}	28.3(6.0)	70	70	43.39	32
$B(E2; 2_2^+ \rightarrow 0_1^+)$	$0.26^{+0.20}_{-0.08}$	–	0.0	0.0	0.34	2.5
$B(E2; 2_2^+ \rightarrow 0_2^+)$	$1.8^{+1.4}_{-0.6}$	–	2.0	2.0	0.06	47
$B(E2; 2_2^+ \rightarrow 0_3^+)$	f	–	49	49	6.54	3.2
$B(E2; 2_2^+ \rightarrow 2_1^+)$	$46^{+35}_{-14}g$	–	8.7	8.7	47.22	0.55
$B(E2; 2_3^+ \rightarrow 0_1^+)$	$0.14^{+0.12}_{-0.04}$	–	–	–	2.33	0.01
$B(E2; 2_3^+ \rightarrow 0_2^+)$	$1.7^{+1.5}_{-0.5}$	–	–	–	2.28	0.56
$B(E2; 2_3^+ \rightarrow 2_1^+)$	$7.6^{+6.5}_{-2.3}$	–	–	–	1.81	46
$B(E2; 4_1^+ \rightarrow 2_1^+)$	25^{+15}_{-7}	43.3(8.7)	103	0.6	68.0	59
$B(E2; 4_1^+ \rightarrow 2_2^+)$	38^{+26}_{-13}	67.5(13.5)	0.7	76	1.68	67
$B(E2; 4_2^+ \rightarrow 2_1^+)$	$0.6^{+0.17}_{-0.12}$	–	0.6	103	h	0.05
$B(E2; 4_2^+ \rightarrow 2_2^+)$	$4.6^{+1.7}_{-1.3}$	–	76	0.7	h	0.11
$B(E2; 6_1^+ \rightarrow 4_1^+)$	–	103.0(35.7)	102	87	76.9	143
	ENSDF ⁱ					
$B(E2; 0_3^+ \rightarrow 2_1^+)$	58(8)	–	–	–	37	53
$B(E2; 0_4^+ \rightarrow 2_2^+)$	42(3)	–	–	–	46	42
$B(E2; 0_4^+ \rightarrow 2_1^+)$	0.103(8)	–	–	–	0.045	0.33

^aFrom Ref. [14].

^bCalculation from Ref. [23]. Level assignments as in Ref. [42].

^cCalculation from Ref. [23]. Level assignments as in Ref. [14].

^dCalculation from Refs. [25,26].

^eCalculation from Ref. [27].

^fSee the text.

^gAssuming a pure $E2$ transition.

^hOutside IBM-CM model space. See the text.

ⁱFrom Ref. [11].

$0_2^+ = 1.7^{+1.5}_{-0.5}$, $B(E2; 2_1^+ \rightarrow 0_1^+) = 1.1^{+0.3}_{-0.2}$ and $B(E2; 2_2^+ \rightarrow 0_1^+) = 0.26^{+0.20}_{-0.08}$ W.u. conform with the IBM-CM-1 calculation [25,26] and the interpretation of the 0_1^+ and

the 2_3^+ as normal states with single-particle character weakly mixed with the intruder states. The measured $E2$ rates $B(E2; 2_3^+ \rightarrow 2_1^+) = 7.6^{+6.5}_{-2.3}$ W.u. deviates from

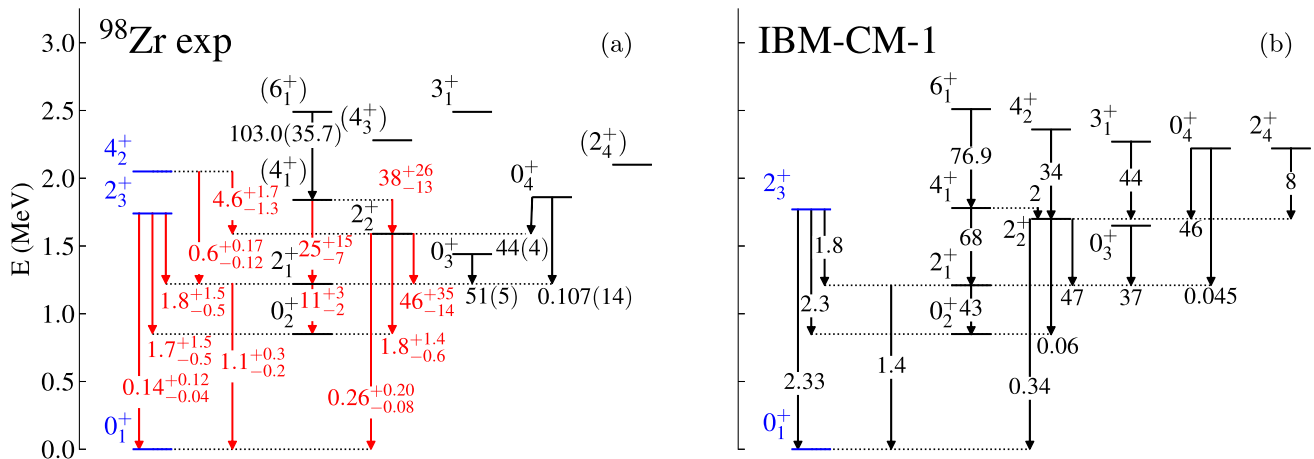


FIG. 11. (a) Experimental and (b) calculated [25,26] energy levels in MeV and $E2$ rates in W.u. for ^{98}Zr . Levels marked in blue (black) indicate states assigned to the A-normal (B-intruder) configuration. $E2$ transitions strengths marked in red are from the current paper.

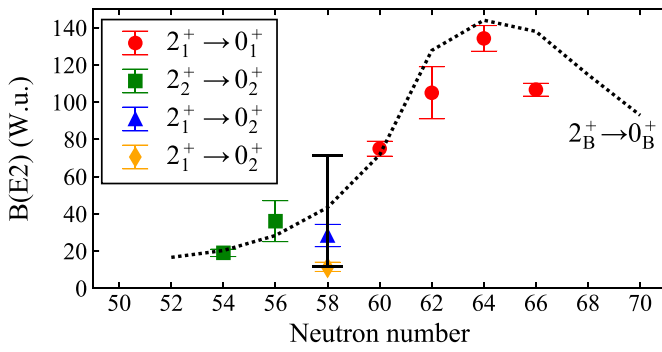


FIG. 12. $E2$ transition rates in W.u. for $2^+ \rightarrow 0^+$ transitions within the intruder- B configuration for the Zr isotopes. The symbols (\bullet , \blacksquare , \blacktriangle , and \blacklozenge) denote experimental rates. The dashed line depicts the IBM-CM-1 calculation of Ref. [25]. The data for ^{94}Zr , ^{96}Zr , ^{100}Zr , ^{102}Zr , and (^{104}Zr , ^{106}Zr) are taken from Refs. [3,4,13,42,46], respectively. For ^{98}Zr , the experimental values are from the current paper (\blacklozenge), from Ref. [14] (\blacktriangle), and the black upper and lower limits are from Refs. [42,45]. Note that the explicit experimental values in ^{98}Zr deviate from one another as well as from the calculated values of the IBM-CM-1 (43.39 W.u.) and of the MCSM (70 W.u.).

the calculated value of 1.8 W.u., however, a merely 1% decrease in the parameter $\epsilon_d^{(A)}$ in the Hamiltonian [25] results in a calculated value of 6.1 W.u. for this transition without affecting significantly the remaining transitions in Table III. As mentioned above, the experimental 4_2^+ state is excluded from the IBM-CM-1 model space, however, the transition rates involving it $B(E2; 4_2^+ \rightarrow 2_1^+) = 0.6_{-0.12}^{+0.17}$ and $B(E2; 4_2^+ \rightarrow 2_2^+) = 4.6_{-1.3}^{+1.7}$ W.u. support the assignment of the experimental 4_2^+ as a normal single-particle state, weakly mixed with the intruder band.

The IBM-CM-1 describes reasonably well most of the transitions listed in Table III. However, some of the newly measured transitions within the intruder band, reported in the present paper, exhibit marked differences from previous measurements and from both the IBM-CM-1 and the MCSM calculations. Specifically, the value of $B(E2; 2_1^+ \rightarrow 0_2^+) = 11_{-2}^{+3}$ W.u. is significantly lower than the recently measured value of 28.3(60) W.u. in Ref. [14], and conforms only with the lower (11.5 W.u.) and upper (71.3 W.u.) limits obtained in Refs. [42,45], respectively. Furthermore, although both the calculated IBM-CM-1 (43.39 W.u.) and MCSM (70 W.u.) values are in-between the experimental upper [45] and lower [42] limits, yet they deviate considerably from the explicit values of Ref. [14] and of the current paper. These deviations are somewhat surprising, in view of the trend in the calculated $E2$ rates from the first 2^+ state to the first 0^+ state within the intruder B configuration as portrayed by the dashed line in Fig. 12. Since deformation is increased as neutrons are added [17], an increase in this $B(E2)$ value at neutron number 58 is expected [23,25,26] when going from neutron number 56 to 60.

Additional discrepancies between calculated and measured values occur for transitions involving the 4_1^+ state. Specifically, both measured transition rates $B(E2; 4_1^+ \rightarrow 2_1^+) =$

25_{-7}^{+15} and $B(E2; 4_1^+ \rightarrow 2_2^+) = 38_{-13}^{+26}$ W.u. are strong, a situation that cannot be accommodated neither by the IBM-CM-1, nor by the MCSM calculations. In the IBM-CM-1 calculation, these values are 68 and 2 W.u., respectively, and reflect the fact that both the 4_1^+ and the 2_2^+ are members of the $n_d \approx 2$ triplet of configuration (B) and are weakly mixed with states in the normal A configuration. In such circumstances, these states cannot be connected by strong $E2$ transitions, which follow the selection rules $\Delta n_d = \pm 1$. As shown in Table III, both versions of the MCSM calculations, MCSM-1 and MCSM-2, encounter a similar problem and cannot accommodate simultaneously two strong transitions from the 4_1^+ state.

Recently, another independent IBM-CM calculation (named IBM-CM-2 in Table III) was carried out by García-Ramos and Heyde [27]. In the IBM-CM-2 the structure of 4_1^+ is similar to that of IBM-CM-1, however, the 2_1^+ and 2_2^+ states exhibit strong normal-intruder mixing with $a^2 = 55\%$ and $a^2 = 45\%$, respectively. Consequently, the IBM-CM-2 can describe adequately the empirical $B(E2; 4_1^+ \rightarrow 2_1^+)$ and $B(E2; 4_1^+ \rightarrow 2_2^+)$ rates. However, this structure leads to other noticeable discrepancies. In particular, the calculated $B(E2; 2_2^+ \rightarrow 0_2^+) = 47$, $B(E2; 2_3^+ \rightarrow 2_1^+) = 46$, and $B(E2; 2_2^+ \rightarrow 2_1^+) = 0.55$ W.u. are at variance with the experimental values of $1.8_{-0.6}^{+1.4}$, $7.6_{-2.3}^{+6.5}$, and 46_{-14}^{+35} W.u., respectively.

V. CONCLUSIONS AND OUTLOOK

The lifetimes of the 2_1^+ , 2_2^+ , 2_3^+ , 4_1^+ , 4_2^+ , and the 3_1^- states in ^{98}Zr have been measured using the Doppler-based techniques RDDS and DSA. The results have been compared to the recently performed calculations in the framework of the Monte Carlo shell model and the interacting boson model with configuration mixing. Although both approaches provide a good overall description of the structure of ^{98}Zr , there are some noticeable discrepancies. Some of the present measured transitions within the intruder band exhibit marked differences from the previous measurements in Ref. [14]. Most notably, the measured weak transition $B(E2; 2_1^+ \rightarrow 0_2^+)$ suggests the need to corroborate the lifetime of the 2_1^+ state using other lifetime measurement methods and to explore further the structure of the 2_1^+ and the 0_2^+ states. This suggests the need for further theoretical and experimental investigations. It would also be interesting to corroborate the $2_2^+ \rightarrow 0_3^+$ branching and the lifetime of the 2_2^+ state to obtain the $B(E2; 2_2^+ \rightarrow 0_3^+)$ value, which is calculated to be weak (6.54 W.u.) in the IBM-CM-1 and strong (49 W.u.) in the MCSM. This can provide clues towards understanding whether the 0_3^+ , 2_2^+ , and 4_1^+ states are part of a quasi-two-phonon triplet as in the IBM-CM-1 calculation [25,26] or part of a deformed configuration, possibly separated from the 0_2^+ and the 2_1^+ states as in the MCSM calculation [14,23].

ACKNOWLEDGMENTS

A.E. and V.K. acknowledge financial support from the BMBF under Grant No. 05P19PKFNA. J.-M.R. and L.K. acknowledge financial support from the Deutsche Forschungsgemeinschaft (DFG) under Grant No. JO391/16-2. We thank

J. E. García-Ramos for providing the $B(E2)$ values from the calculation in Ref. [27]. We also thank T. Otsuka for providing the $B(E2)$ values from the calculation in Ref. [23]. The work

of A.L. and N.G. was supported by the US-Israel Binational Science Foundation Grant No. 2016032 and, in part, by the Israel Science Foundation Grant No. 586/16.

-
- [1] P. Cejnar, J. Jolie, and R. F. Casten, *Rev. Mod. Phys.* **82**, 2155 (2010).
- [2] K. Heyde and J. L. Wood, *Rev. Mod. Phys.* **83**, 1467 (2011).
- [3] C. Kremer, S. Aslanidou, S. Bassauer, M. Hilcker, A. Krugmann, P. von Neumann-Cosel, T. Otsuka, N. Pietralla, V. Y. Ponomarev, N. Shimizu, M. Singer, G. Steinhilber, T. Togashi, Y. Tsunoda, V. Werner, and M. Zweidinger, *Phys. Rev. Lett.* **117**, 172503 (2016).
- [4] A. Chakraborty, E. E. Peters, B. P. Crider, C. Andreoiu, P. C. Bender, D. S. Cross *et al.*, *Phys. Rev. Lett.* **110**, 022504 (2013).
- [5] E. Clément *et al.*, *Phys. Rev. Lett.* **116**, 022701 (2016).
- [6] E. Clément *et al.*, *Phys. Rev. C* **94**, 054326 (2016).
- [7] E. Browne, *Nucl. Data Sheets* **82**, 379 (1997).
- [8] C. M. Baglin, *Nucl. Data Sheets* **113**, 2187 (2012).
- [9] D. Abriola and A. A. Sonzogni, *Nucl. Data Sheets* **107**, 2423 (2006).
- [10] D. Abriola and A. A. Sonzogni, *Nucl. Data Sheets* **109**, 2501 (2008).
- [11] J. Chen and B. Singh, *Nucl. Data Sheets* **164**, 1 (2020).
- [12] B. Singh, *Nucl. Data Sheets* **109**, 297 (2008).
- [13] D. De Frenne, *Nucl. Data Sheets* **110**, 1745 (2009).
- [14] P. Singh, W. Korten, T. W. Hagen, A. Gørgen, L. Greife, M.-D. Salsac *et al.*, *Phys. Rev. Lett.* **121**, 192501 (2018).
- [15] P. Federman and S. Pittel, *Phys. Lett. B* **69**, 385 (1977).
- [16] P. Federman and S. Pittel, *Phys. Lett. B* **77**, 29 (1978).
- [17] P. Federman and S. Pittel, *Phys. Rev. C* **20**, 820 (1979).
- [18] T. Otsuka, T. Suzuki, R. Fujimoto, H. Grawe, and Y. Akaishi, *Phys. Rev. Lett.* **95**, 232502 (2005).
- [19] T. Otsuka, T. Suzuki, M. Honma, Y. Utsuno, N. Tsunoda, K. Tsukiyama, and M. Hjorth-Jensen, *Phys. Rev. Lett.* **104**, 012501 (2010).
- [20] T. Otsuka and Y. Tsunoda, *J. Phys. G: Nucl. Part. Phys.* **43**, 024009 (2016).
- [21] K. Sieja, F. Nowacki, K. Langanke, and G. Martínez-Pinedo, *Phys. Rev. C* **79**, 064310 (2009).
- [22] N. Shimizu, T. Abe, Y. Tsunoda, Y. Utsuno, T. Yoshida, T. Mizusaki, M. Honma, and T. Otsuka, *Prog. Theor. Exp. Phys.* **2012**, 01A205 (2012).
- [23] T. Togashi, Y. Tsunoda, T. Otsuka, and N. Shimizu, *Phys. Rev. Lett.* **117**, 172502 (2016).
- [24] A. Petrovici, *Phys. Rev. C* **85**, 034337 (2012).
- [25] N. Gavrielov, A. Leviatan, and F. Iachello, *Phys. Rev. C* **99**, 064324 (2019).
- [26] N. Gavrielov, A. Leviatan, and F. Iachello, *Phys. Scr.* **95**, 024001 (2019).
- [27] J. E. García-Ramos and K. Heyde, *Phys. Rev. C* **100**, 044315 (2019).
- [28] A. Dewald, O. Möller, and P. Petkov, *Progr. Part. Nucl. Phys.* **67**, 786 (2012).
- [29] T.K. Alexander and A. Bell, *Nucl. Instrum. Methods* **81**, 22 (1970).
- [30] A. Dewald, S. Harissopulos, and P. von Brentano, *Z. Phys. A* **334**, 163 (1989).
- [31] J. Litzinger *et al.*, *Phys. Rev. C* **92**, 064322 (2015).
- [32] B. Saha, Program napatau, Inst. Nucl. Phys. Cologne.
- [33] D. B. Fossan and E. K. Warburton, *Nuclear Spectroscopy and Reactions, Part C* (Elsevier, Amsterdam, 1974), Vol. 40, p. 307.
- [34] P. J. Nolan and J. F. Sharpey-Schafer, *Rep. Prog. Phys.* **42**, 1 (1979).
- [35] C. Stahl, J. Leske, M. Lettmann, and N. Pietralla, *Comp. Phys. Commun.* **214**, 174 (2017).
- [36] S. Agostinelli *et al.*, *Nucl. Instrum. Methods Phys. Res., Sect. A* **506**, 250 (2003).
- [37] J. F. Ziegler, M. D. Ziegler, and J. P. Biersack, *Nucl. Instrum. Methods Phys. Res., Sect. A* **268**, 1818 (2010).
- [38] A. Winther, *Nucl. Phys. A* **572**, 191 (1994).
- [39] R. Yanez and W. Loveland, *Phys. Rev. C* **91**, 044608 (2015).
- [40] K. Becker, G. Jung, K.-H. Kobras, H. Wollnik, and B. Pfeiffer, *Z. Phys. A* **319**, 193 (1984).
- [41] W. Urban, M. Czerwinski, J. Kurpeta, T. Rzaca-Urban, J. Wisniewski, T. Materna *et al.*, *Phys. Rev. C* **96**, 044333 (2017).
- [42] S. Ansari, J. M. Regis, J. Jolie, N. Saed-Samii, N. Warr, W. Korten *et al.*, *Phys. Rev. C* **96**, 054323 (2017).
- [43] P. D. Duval and B. R. Barrett, *Nucl. Phys. A* **376**, 213 (1982).
- [44] P. D. Duval, D. Goutte, and M. Vergnes, *Phys. Lett. B* **124**, 297 (1983).
- [45] W. Witt, V. Werner, N. Pietralla, M. Albers, A. D. Ayangeakaa, B. Bucher *et al.*, *Phys. Rev. C* **98**, 041302(R) (2018).
- [46] F. Browne *et al.*, *Phys. Lett. B* **750**, 448 (2015).

7 Conclusion and outlook

In the scope of this doctoral thesis, lifetimes of excited states in nuclei above the doubly-magic ^{208}Pb nucleus have been measured employing the fast-timing, the RDDS, and the DSA methods. The newly deduced transition probabilities in ^{211}At and ^{209}Po have revealed that the nuclear-shell model cannot fully account for the transition probabilities due to missing components in the wave function of the nuclear states. The presence of particle-hole excitations in the wave function of the ground state of ^{210}Po has been proposed as a possible reason to explain the discrepancy. However, more research, both on the theoretical and the experimental sides is needed to further study this conundrum. The single-j calculations performed for ^{211}At , based on ^{210}Po , describe the newly deduced transition probabilities very well. This shows that seniority could be regarded as a good quantum number, both in ^{210}Po and ^{211}At . It would be interesting to continue this study along the other N=126 isotones. In fact, the ^{213}Fr nucleus, which was populated in the activation process of the ^{209}Po experiment, was already studied and a paper is already in preparation.

The measured lifetime of the first excited 4^+ states in ^{204}Po and ^{206}Po indicates that already at N=122 the 4_1^+ state of the Po isotopes starts to be collective. However, the measured lifetime of the 4_1^+ state in ^{204}Po has a rather large uncertainty and it would be beneficial to remeasure it more precisely. It would be also interesting to conduct a similar measurement in the Rn and Ra isotopes and see how the additional protons influence the onset of collectivity. As a matter of fact, fast-timing experiments aiming to measure the first excited 4^+ states in ^{206}Rn and ^{208}Rn were already conducted during the preparation of this thesis. The preliminary analysis of the data shows that both the 4_1^+ states are collective.

The newly measured lifetime of the important 2_1^+ state in ^{98}Zr is significantly longer than the previously measured one in Ref. [46]. This shows that the 2_1^+ and the 0_2^+ are not both members of a collective structure. The lifetimes of the 2_2^+ and 2_3^+ states were also measured in the study of ^{98}Zr . However, no transition stemming from these states have a large enough $B(E2)$ to be considered as a collective one. Although the feeding pattern in the two-neutron transfer reaction used to study ^{98}Zr is simple, a presence of some unobserved

feeding could not be excluded completely. It would be very interesting to corroborate this lifetime by other independent measurements. It would be also interesting to measure the branching of the $2_2^+ \rightarrow 0_3^+$ transition to determine the transition probability of this transition. This will give the answer if 2_2^+ and 0_3^+ are members of a collective structure. To answer this question and to corroborate the measured lifetimes an experiment at the Lohengrin spectrometer [49] was performed. ^{98}Y nuclei were populated in the neutron-induced fission and were implanted at the focal plane of the spectrometer. After the implantation, the ^{98}Y nucleus undergoes a β decay populating low-spin states in ^{98}Zr . The data is in process of analysis at the moment.

Appendix: Test of the APCAD procedure for a DSA analysis: The lifetime of the 3_1^- state in ^{88}Sr

To test the DSA analysis procedure of the program APCAD, the known lifetime of the 3_1^- state in ^{88}Sr was remeasured. The nucleus of interest was populated in the Coulomb excitation reaction $^{88}\text{Sr}(^{18}\text{O}, ^{18}\text{O})^{88}\text{Sr}^*$ at beam energy of 50 MeV. The target was a 1.4 mg/cm^2 natural Sr evaporated on an 8 mg/cm^2 Au backing. The Sr was sealed by a thin Au layer with a thickness of 0.1 mg/cm^2 to prevent oxidation of the target in the air. A particle and γ gated spectrum from the experiment is shown in Fig. 8. The gate in this spectrum has been placed only on the stopped component of the $2_1^+ \rightarrow 0_1^+$ transition. The spectrum serves as a qualitative indicator of the feeding pattern of the 3_1^- state. The intensities of the transitions were obtained from a spectrum in which the gate was placed both on the feeding and stopped components of the $2_1^+ \rightarrow 0_1^+$ transition. The intensities of the observed transitions are given in Table 1. Based on a γ - γ coincidence analysis a partial level scheme was build and is displayed in Fig. 9.

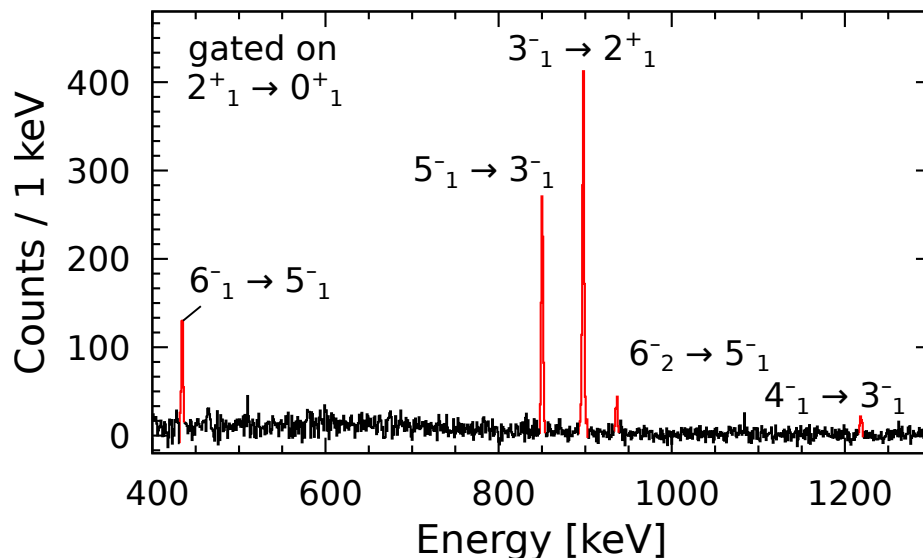


Figure 8: Particle- γ gated γ -ray spectrum of both detector rings. Transitions belonging to ^{88}Sr are indicated and colored in red. The γ -ray gate has been placed only on the stopped component of the $2_1^+ \rightarrow 0_1^+$ transition.

Table 1: γ -ray transitions observed in ^{88}Sr populated in the $^{88}\text{Sr}(^{18}\text{O},^{18}\text{O})^{88}\text{Sr}^*$ reaction. Transition intensities are normalized to the $3_1^- \rightarrow 2_1^+$ transition intensity.

Transition	Energy [keV]	Intensity
$3_1^- \rightarrow 2_1^+$	898	100(1)
$5_1^- \rightarrow 3_1^-$	851	27(1)
$4_1^- \rightarrow 3_1^-$	1219	3(1)
$6_1^- \rightarrow 5_1^-$	435	6(1)
$6_2^- \rightarrow 5_1^-$	937	10(1)

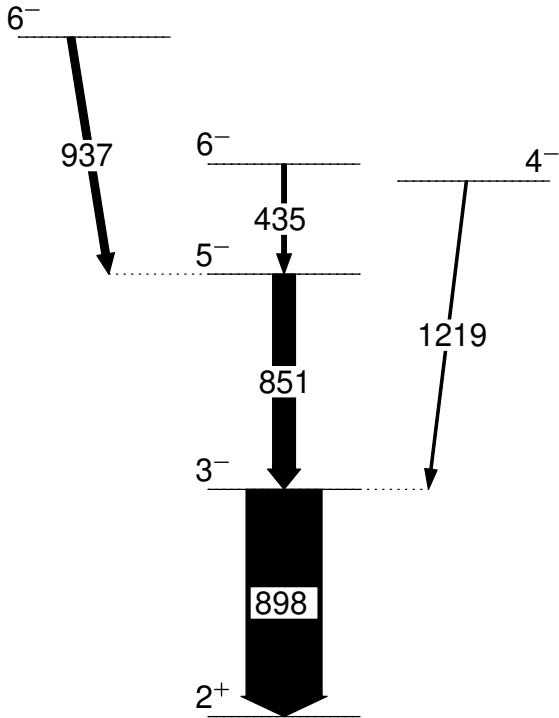


Figure 9: Partial level scheme of ^{88}Sr populated in the $^{88}\text{Sr}(^{18}\text{O},^{18}\text{O})^{88}\text{Sr}^*$ reaction. The width of the lines is proportional to the intensities of the transitions.

The DSA procedure to determine the lifetime was carried out as explained in the Subsection 1.1.2. The stopping powers were taken from SRIM [17]. The doubly-differential cross-section was adopted from Ref. [50] where the similar reaction $^{88}\text{Sr}(^{16}\text{O},^{16}\text{O})^{88}\text{Sr}^*$ was employed. Alternatively, the reaction cross sections were calculated using the GRAZING code [19, 20] or using the computer program CLX [51]. All three cross-sections give very similar results, with less than 1 % variation in the final lifetime. The stopping matrix is displayed in Fig. 10.

The fits to the Doppler-broadened line-shape of the $3_1^- \rightarrow 2_1^+$ transition for both detector rings are shown in Fig. 11. The feeding coming from all other states has been taken into account when determining the lifetime. The lifetimes of the feeding states were taken from the evaluated nuclear data [52]. The resulting lifetimes are 0.97(7) ps and 0.97(8) ps for the forward and backward detector rings, respectively. The errors given here are only the statistical errors of the fit. These results are in perfect agreement with the evaluated value of 1.00(7)ps [52]. The evaluated value is a weighted average of

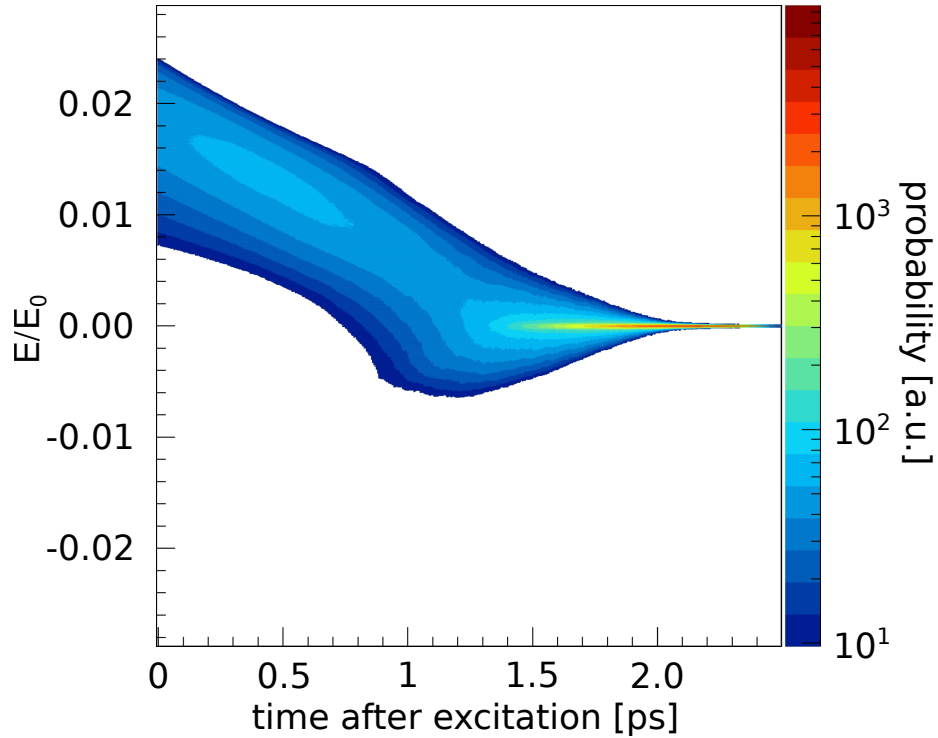


Figure 10: Stopping matrix for ^{88}Sr ion stopping in the target.

1.13(7) ps measured in (e,e') electron scattering experiment conducted in the scope of an unpublished doctoral thesis [53] and 0.97(4) ps obtained in a DSA measurement after Coulomb excitation [54].

The dependence from variations in the stopping powers and the target thickness of the lifetime was investigated. 10 % variation in the stopping power produced a difference of 0.01 ps in the final lifetime. This difference is much smaller than the statistical error of the fit. The thickness of the target has a much larger effect on the resulting lifetime. 10 % variation of the thickness of the Sr layer in the simulation results in 0.06 ps difference in the lifetime. However, 10 % from the Sr layer thickness is 0.14 mg/cm^2 . Such uncertainty of the thickness of a target produced by the skillful target makers of the University of Cologne is unrealistically large.

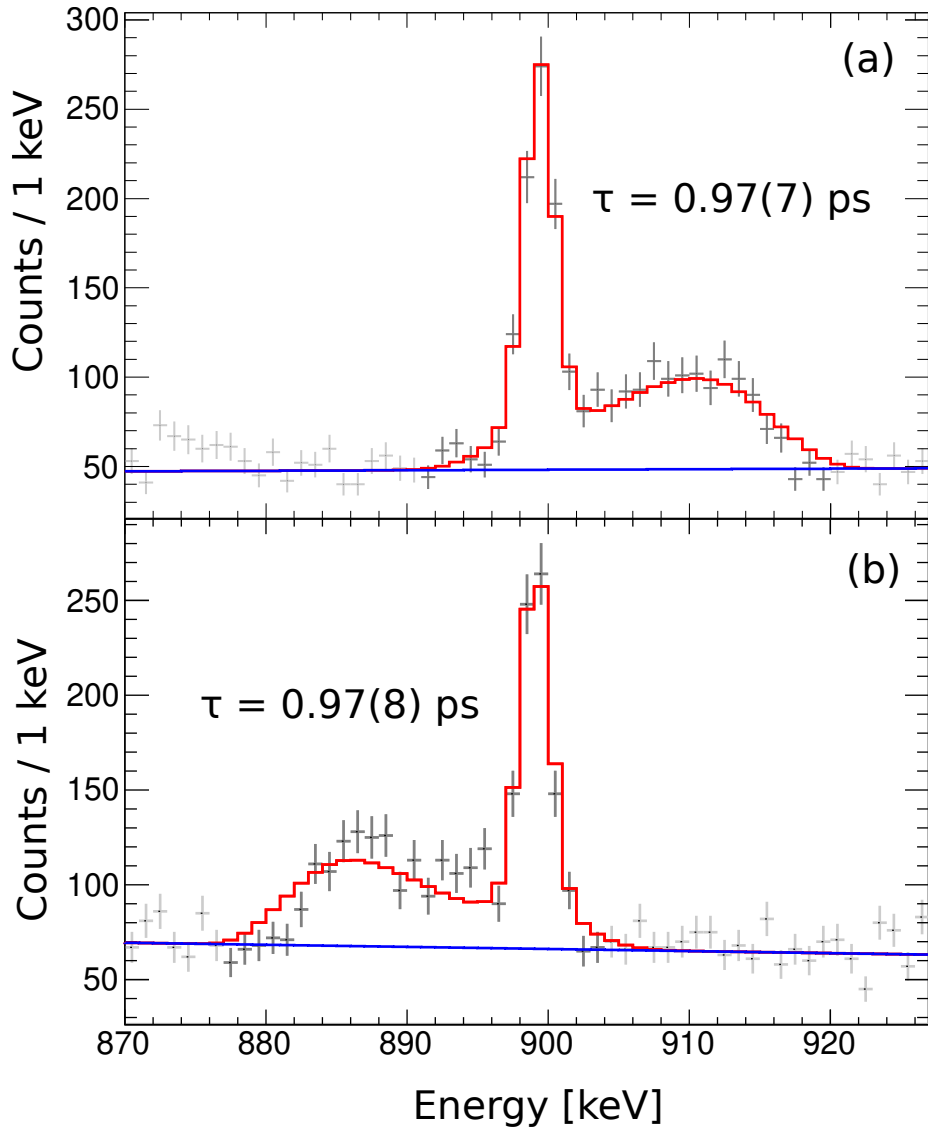


Figure 11: DSA fits to the Doppler-broadened lineshape of the $3_1^- \rightarrow 2_1^+$ transition. (a) is for the forward detector ring, (b) is for the backward detector ring. The spectra are generated by setting a particle gate and a γ -gate on both the shifted and the unshifted components of the $2_1^+ \rightarrow 0_1^+$ transition.

Bibliography

- [1] D.B. Fossan and E.K. Warburton. In *Nuclear Spectroscopy and Reactions, Part C*, volume 40, page 307. Elsevier, 1974.
- [2] P. J. Nolan and J. F. Sharpey-Schafer. *Rep. Prog. Phys.*, 42(1):1, 1979.
- [3] Z. Bay. *Phys. Rev.*, 77(3):419, feb 1950.
- [4] P. Dorenbos E. V. D. van Loef and C. W. E. van Eijk. *Appl. Phys. Lett.*, 79(10):1573, 2001.
- [5] J.-M. Régis, G S Simpson, A Blanc, G de France, M Jentschel, U Köster, P Mutti, V Pazyi, N Saed-Samii, T Soldner, C A Ur, W Urban, A M Bruce, F Drouet, L M Fraile, S Ilieva, J Jolie, W Korten, T Kröll, S Lalkovski, H Mach, N Mărginean, G Pascovici, Zs. Podolyak, P H Regan, O J Roberts, J F Smith, C Townsley, A Vancraeynest, and N Warr. *Nucl. Instrum. Methods Phys Res., Sect.*, 763:210, 2014.
- [6] J.-M. Régis et al. *Nucl. Instr. Meth. Phys. Res., Sect. A*, 726:191, 2013.
- [7] J.-M. Régis et al. *Nucl. Instr. Meth. Phys. Res. Sect. A*, 823:72, 2016.
- [8] J.-M. Régis, M Rudigier, J Jolie, A Blazhev, C Fransen, G Pascovici, and N Warr. *Nucl. Instrum. Methods Phys Res., Sect.*, 684:36, 2012.
- [9] J.-M. Régis, A. Esmaylzadeh, J. Jolie, V. Karayonchev, L. Knafla, U. Köster, Y.H. Kim, and E. Strub. *Nucl. Inst. Meth. Phys. Res. Sect. A*, 955:163258, 2020.
- [10] C. Mihai, G. Pascovici, G. Ciocan, C. Costache, V. Karayonchev, A. Lungu, N. Mărginean, R.E. Mihai, C. Neacșu, J.-M. Régis, A. Turturica, S. Ujeniuc, and A. Vasiliu. *Nucl. Instr. Meth. A*, 953:163263, 2020.
- [11] J.-M. Régis, G Pascovici, J Jolie, and M Rudigier. *Nucl. Instrum. Methods Phys Res., Sect.*, 622(1):83, 2010.
- [12] V. Karayonchev, A. Blazhev, A. Esmaylzadeh, J. Jolie, M. Dannhoff, F. Diel, F. Dunkel, C. Fransen, L. M. Gerhard, R.-B. Gerst, L. Knafla, L. Kornweibel, C. Müller-Gatermann, J.-M. Régis, N. Warr, K. O. Zell, M. Stoyanova, and P. Van Isacker. *Phys. Rev. C*, 99:024326, Feb 2019.
- [13] A. Dewald, O. Möller, and P. Petkov. *Progr. Part. Nucl. Phys.*, 67(3):786, 2012.

- [14] A Z Schwarzschild and E K Warburton. *Ann. Rev. Nucl. Sc.*, 18(1):265, 1968.
- [15] C. Stahl, J. Leske, M. Lettmann, and N. Pietralla. *Comp. Phys. Comm.*, 214:174, 2017.
- [16] S. Agostinelli et al. *Nucl. Inst. Meth. Phys. Res. Sect. A*, 506(3):250, 2003.
- [17] J. F. Ziegler, M.D. Ziegler, and J.P. Biersack. *Nucl. Inst. Meth. Phys. Res. Sect. A*, 268(11):1818, 2010.
- [18] J. Keinonen. *AIP Conf. Proc.*, (125):557, 1985.
- [19] A. Winther. *Nucl. Phys. A*, 572(1):191, 1994.
- [20] R. Yanez and W. Loveland. *Phys. Rev. C*, 91:044608, Apr 2015.
- [21] W. Marciano and H. Pagels. *Phys. Rep.*, 36(3):137, 1978.
- [22] T. Hamada and I.D. Johnston. *Nuc. Phys.*, 34(2):382, 1962.
- [23] R. Machleidt, K. Holinde, and Ch. Elster. *Phys. Rep.*, 149(1):1, 1987.
- [24] E. Epelbaum, H.-W. Hammer, and Ulf-G. Meißner. *Rev. Mod. Phys.*, 81:1773, Dec 2009.
- [25] R. Machleidt and D.R. Entem. *Phys. Rep.*, 503(1):1, 2011.
- [26] Maria Goeppert Mayer. *Phys. Rev.*, 78:16, Apr 1950.
- [27] O. Haxel, J. Hans D. Jensen, and Hans E. Suess. *Phys. Rev.*, 75:1766, Jun 1949.
- [28] G.H. Herling and T.T.S. Kuo. *Nuc. Phys. A*, 181(1):113, 1972.
- [29] S. Bonger, T.T.S. Kuo, and L. Coraggio. Low momentum nucleon–nucleon potentials with half-on-shell t-matrix equivalence. *Nuclear Physics A*, 684(1):432 – 436, 2001.
- [30] J.B. McGrory and T.T.S. Kuo. *Nucl. Phys. A*, 247(2):283, 1975.
- [31] T.R. McGoram, G.D. Dracoulis, A.P. Byrne, A.R. Poletti, and S. Bayer. *Nucl. Phys. A*, 637(4):469, 1998.
- [32] E. K. Warburton and B. A. Brown. *Phys. Rev. C*, 43:602, Feb 1991.
- [33] L. Coraggio, A. Covello, A. Gargano, N. Itaco, and T. T. S. Kuo. *Phys. Rev. C*, 58:3346, Dec 1998.
- [34] E. Caurier, M. Rejmund, and H. Grawe. *Phys. Rev. C*, 67:054310, May 2003.
- [35] D. Kocheva et al. *Eur. Phys. J. A*, 53(9):175, 2017.

- [36] D. Kocheva et al. *Phys. Rev. C*, 96:044305, Oct 2017.
- [37] R. F. Casten, D. S. Brenner, and P. E. Haustein. *Phys. Rev. Lett.*, 58:658, Feb 1987.
- [38] P. Federman and S. Pittel. *Physics Letters B*, 69(4):385, 1977.
- [39] T Grahn and other. *Eur. Phys. J. A*, 52(11):340, Nov 2016.
- [40] Jun Chen and Balraj Singh. *Nuclear Data Sheets*, 164:1, 2020.
- [41] Balraj Singh. *Nuclear Data Sheets*, 109(2):297, 2008.
- [42] Coral M. Baglin. *Nuclear Data Sheets*, 113(10):2187, 2012.
- [43] D. Abriola and A.A. Sonzogni. *Nuclear Data Sheets*, 107(9):2423, 2006.
- [44] D. Abriola and A.A. Sonzogni. *Nuclear Data Sheets*, 109(11):2501, 2008.
- [45] D. De Frenne. *Nuclear Data Sheets*, 110(8):1745, 2009.
- [46] Purnima Singh, W. Korten, T. W. Hagen, A. Gorgen, L. Grente, M.-D. Salsac, et al. *Phys. Rev. Lett.*, 121:192501, Nov 2018.
- [47] P. Federman and S. Pittel. *Physics Letters B*, 77(1):29, 1978.
- [48] P. Federman and S. Pittel. *Phys. Rev. C*, 20:820, Aug 1979.
- [49] P. Armbruster, M. Asghar, J.P. Bocquet, R. Decker, H. Ewald, J. Greif, E. Moll, B. Pfeiffer, H. Schrader, F. Schussler, G. Siegert, and H. Wollnik. *Nucl. Instr. Meth.*, 139:213, 1976.
- [50] F.D. Becchetti, P.R. Christensen, V.I. Manko, and R.J. Nickles. *Nucl. Phys. A*, 203(1):1, 1973.
- [51] H. Owner. Computer program clx, unpublished.
- [52] E.A. McCutchan and A.A. Sonzogni. *Nuclear Data Sheets*, 115:135, 2014.
- [53] L.T.Van der Bijl. Thesis, vrije univ.amsterdam (1982).
- [54] G. J. Kumbartzki, K.-H. Speidel, N. Benczer-Koller, D. A. Torres, Y. Y. Sharon, L. Zamick, S. J. Q. Robinson, P. Maier-Komor, T. Ahn, V. Anagnostatou, Ch. Bernards, M. Elvers, P. Goddard, A. Heinz, G. Ilie, D. Radeck, D. Savran, V. Werner, and E. Williams. *Phys. Rev. C*, 85:044322, Apr 2012.

List of publications and conference proceedings

1. V. Karayonchev et al., Phys. Rev. C 102, 064314 (2020).
2. M. Stoyanova, V. Karayonchev, G. Rainovski, et al., J. Phys. Conf. Ser. 1555, 012019 (2020).
3. D. Kocheva et al., J. Phys. Conf. Ser. 1555, 012020 (2020).
4. Ralph Kern et al., J. Phys. Conf. Ser. 1555, 012027 (2020).
5. J. Benito et al. (IDS Collaboration), Phys. Rev. C 102, 014328 (2020).
6. M. Rudigier et al., Nuc. Instr. Meth. A 969, 163967 (2020).
7. J.-M. Régis, A. Esmaylzadeh, J. Jolie, V. Karayonchev, L. Knafla, U. Köster, Y.H. Kim, and E. Strub, Nuc. Instr. Meth. A 955, 163258 (2020).
8. R. L. Canavan et al., Phys. Rev. C 101, 024313 (2020).
9. C. Mihai, G. Pascovici, G. Ciocan, C. Costache, V. Karayonchev, A. Lungu, N. Mărginean, R.E.Mihai, C. Neacșu, J.-M. Régis, A. Turturica, S. Ujeniuc, and A. Vasiliu, Nuc. Instr. Meth. A 953, 163263 (2020).
10. A. Esmaylzadeh, J.-M. Régis, Y. H. Kim, U. Köster, J. Jolie, V. Karayonchev, L. Knafla, K. Nomura, L. M. Robledo, and R. Rodríguez-Guzmán, Phys. Rev. C 100, 064309 (2019).
11. M. Stoyanova et al., Phys. Rev. C 100, 064304 (2019).
12. L. Kaya et al., Phys. Rev. C 100, 024323 (2019).
13. M. Rudigier et al., Act. Phys. Pol. B 50, 661 (2019).
14. V. Karayonchev et al., Phys. Rev. C 99, 024326 (2019).
15. M. Piersa et al., Phys. Rev. C 99, 024304 (2019).
16. C. M. Petrache et al., Phys. Rev. C 99, 024303 (2019).
17. M. Stoyanova et al., Eur. Phys. J W. Conf. 194 (2018).
18. R. Kern et al., Eur. Phys. J. W. Conf. 194, 03003 (2018).
19. A. Esmaylzadeh, L. M. Gerhard, V. Karayonchev, et al., Phys. Rev. C 98, 014313 (2018).
20. D. Kocheva et al., J. Phys. Conf. S. 1023, 012019 (2018).
21. R. Lică et al., Phys. Rev. C 97, 024305 (2018).
22. M. Queiser et al., Phys. Rev. C 96, 044313 (2017).
23. D. Kocheva et al., Phys. Rev. C 96, 044305 (2017).
24. D. Kocheva et al., Eur. Phys. J A 53, 175 (2017).
25. A. Vogt et al., Phys. Rev. C 96, 024321 (2017).
26. V. Karayonchev et al., Phys. Rev. C 95, 034316 (2017).
27. R. Lică et al., J.Phys. G: Nucl. Part. Phys. 44 (2017).
28. D. Kocheva et al., J. of Phys. Conf. Ser. 724 (2016).

29. J.-M. Régis, N. Saed-Samii, M. Rudigier, S. Ansari, M. Dannhoff, A. Esmaylzadeh, C. Fransen, R.-B. Gerst, J. Jolie, V. Karayonchev, C. Müller-Gatermann, and S. Stegemann, *Nuc. Instr. Meth. A* 823, 72 (2016).
30. D. Kocheva et al., *Phys. Rev. C* 93, 011303 (2016).
31. D. Kocheva et al., *Eur. Phys. J. W. Conf.* 107, 03004 (2016).

Contribution to the publications in this thesis

Publication I:

Lifetimes in ^{211}At and their implications on the nuclear structure above ^{208}Pb

- V. Karayonchev planned the experiment.
- V. Karayonchev installed the setup.
- V. Karayonchev participated actively in the experiment.
- V. Karayonchev analyzed the data.
- V. Karayonchev interpreted the results together with A. Blazhev and P. Van Isacker for the theoretical part.
- V. Karayonchev wrote the paper with the help of A. Blazhev, J. Jolie and P. Van Isacker

Publication II:

Lifetimes of the 4_1^+ states of ^{206}Po and ^{204}Po : A study of the transition from noncollective seniority-like mode to collectivity

- V. Karayonchev installed the setup.
- V. Karayonchev participated actively in the experiment.
- V. Karayonchev analyzed the data together with M. Stoyanova.
- V. Karayonchev helped G. Rainovski in writing the paper.

Publication III:

Tests of collectivity in ^{98}Zr by absolute transition rates

- V. Karayonchev planned the experiment.
- V. Karayonchev helped in installing the setup.
- V. Karayonchev participated actively in the experiment.
- V. Karayonchev analyzed the data.
- V. Karayonchev interpreted the results together with N. Garielov, J. Jolie and A. Leviatan.

- V. Karayonchev wrote the paper with the help of N. Garielov, J. Jolie and A. Leviatan.

Provisionally accepted publication:

Lifetimes and structures of low-lying negative-parity states of ^{209}Po

- V. Karayonchev planned the experiment.
- V. Karayonchev installed the setup.
- V. Karayonchev participated actively in the experiment.
- V. Karayonchev analyzed the data.
- V. Karayonchev helped G. Rainovski in writing the paper.

Pre-print publication:

Particle-hole excitations above ^{208}Pb

- V. Karayonchev planned the experiments.
- V. Karayonchev participated actively in the experiment.
- V. Karayonchev interpreted the results.
- V. Karayonchev wrote the paper.

Acknowledgment

I would like to thank all the people who contributed to this work. My special thank goes to:

- Prof. Dr. Jan Jolie for all his support during my stay at the University of Cologne. For always believing in me and giving me the opportunity to conduct many experiments at the FN-Tandem accelerator. For helping in my scientific and personal development.
- Prof. Dr. Alfred Dewald for his immense work in keeping the FN-Tandem facility running during the many years he has been here, making such a small laboratory with limited financing world-famous. I would also like to thank him for his willingness to be the second examiner of this work.
- Prof. Dr. Schadschneider for his time being the chairman of the examination.
- Prof. Dr. Rainovski for all the successful collaborations we have had during the last 8 years and hopefully, we will have in the future. Many of the ideas presented in this work stem from his research, for which I am grateful.
- Dr. Jean-Marc Régis for teaching me to go always deep with the analysis of the experimental data. For teaching me that there are no "standard" things in an analysis. For teaching me in extreme detail how to conduct fast-timing experiments. For teaching me the virtue of patience. For forming me as an experimental physics.
- Dr. Andrey Blazhev for the many useful discussions we had on many different nuclear structure aspects. I thank him for providing the excellent targets for many of the experiments conducted in this work.
- Dr. Claus Müller-Gattermann for his critical but fair comments on many of the aspects of my work at the University of Cologne. I am grateful to him for providing the tip to use light backing in RDDS experiments. I am also thankful to him for proofreading this work.
- Dr. Christoph Fransen for keeping the many systems at the Tandem accelerator always operational and in good shape. I am grateful for the discussion we had on the RDDS techniques and that he has always been there to make sure that the experiments are running optimally.
- Dr. Diana Kocheva for her instructions on how to use the APCAD program.

Acknowledgments

- Arwin Esmaylzadeh for being always eager to try new experiments and for the countless hours of helpful discussion we had. I am also thankful to him for proofreading this work.
- Guillaume Häfner for discussion we had on many nuclear structure topics. I am also thankful to him for proofreading this work.
- Dr. Karl-Oskar Zell for providing many of the excellent targets used in this work and for always being eager to provide high quality targets.
- Kerstin Schomacker for the tremendous amount of shifts she has done for many of the experiments performed during my stay at the University of Cologne
- Lukas Knafla for the discussions we had. For always being a good team player.
- Alina Goldkuhle for helping me with the thesis regulations.
- Tandem operators for providing the beam needed for the many experiments presented in this work and for keeping the FN-Tandem machine running, more than 50 years after it has been installed for the first time.
- Dr. Nigel Warr for all the discussion we had on a large variety of topics.
- My family for all the support.
- My girlfriend, Kristina Nikolova, for her deep and unconditional love.

Erklärung zur Dissertation

Hiermit versichere ich an Eides statt, dass ich die vorliegende Dissertation selbstständig und ohne die Benutzung anderer als der angegebenen Hilfsmittel und Literatur angefertigt habe. Alle Stellen, die wörtlich oder sinngemäß aus veröffentlichten und nicht veröffentlichten Werken dem Wortlaut oder dem Sinn nach entnommen wurden, sind als solche kenntlich gemacht. Ich versichere an Eides statt, dass diese Dissertation noch keiner anderen Fakultät oder Universität zur Prüfung vorgelegen hat; dass sie - abgesehen von unten angegebenen Teilpublikationen und eingebundenen Artikeln und Manuskripten - noch nicht veröffentlicht worden ist sowie, dass ich eine Veröffentlichung der Dissertation vor Abschluss der Promotion nicht ohne Genehmigung des Promotionsausschusses vornehmen werde. Die Bestimmungen dieser Ordnung sind mir bekannt. Darüber hinaus erkläre ich hiermit, dass ich die Ordnung zur Sicherung guter wissenschaftlicher Praxis und zum Umgang mit wissenschaftlichem Fehlverhalten der Universität zu Köln gelesen und sie bei der Durchführung der Dissertation zugrundeliegenden Arbeiten und der schriftlich verfassten Dissertation beachtet habe und verpflichte mich hiermit, die dort genannten Vorgaben bei allen wissenschaftlichen Tätigkeiten zu beachten und umzusetzen. Ich versichere, dass die eingereichte elektronische Fassung der eingereichten Druckfassung vollständig entspricht. Die Dissertation beinhaltet die Gewinnung von Primärdaten sowie die Analyse solcher Daten, die auf den Servern des Instituts für Kernphysik der Universität zu Köln gesichert und zugänglich sind.

Teilpublikationen:

- V. Karayonchev, A. Blazhev, A. Esmaylzadeh, J. Jolie, M. Dannhoff, F. Diel, F. Dunkel, C. Fransen, L. M. Gerhard, R.-B. Gerst, L. Knafla, L. Kornwebel, C. Müller-Gatermann, J.-M. Régis, N. Warr, K. O. Zell, M. Stoyanova, and P. Van Isacker
“Lifetimes in ^{211}At and their implications on the nuclear structure above ^{208}Pb .”
Phys. Rev. C 99, 024326
- M. Stoyanova, G. Rainovski, J. Jolie, N. Pietralla, A. Blazhev, M. Beckers, A. Dewald, M. Djongolov, A. Esmaylzadeh, C. Fransen, L. M. Gerhard, K. A. Gladnishki, S. Herb, P. R. John, V. Karayonchev, J. M. Keatings, R. Kern, L. Knafla, D. Kocheva, L. Kornwebel, Th. Kröll, M. Ley, K. M. Mashtakov, C. Müller-Gatermann, J.-M. Régis, M. Scheck, K. Schomacker, J. Sinclair, P. Spagnoletti, C. Sürder, N. Warr, V. Werner, and J. Wiederhold
“Lifetimes of the 4_1^+ states of ^{206}Po and ^{204}Po : A study of the transition from non-collective seniority-like mode to collectivity” Phys. Rev. C 100, 064304

- V. Karayonchev, J. Jolie, A. Blazhev, A. Dewald, A. Esmaylzadeh, C. Fransen, G. Häfner, L. Knafla, J. Litzinger, C. Müller-Gatermann, J.-M. Régis, K. Schomacker, A. Vogt, N. Warr, A. Leviatan, and N. Gavrielov
“Tests of collectivity in ^{98}Zr by absolute transition rates”
Phys. Rev. C 102, 064314

Köln, den 21. April 2021

Vasil Karayonchev